Reduction Studies on Tungsten Hexachloride

Reduktions Studien von Wolfram(VI)-Chlorid

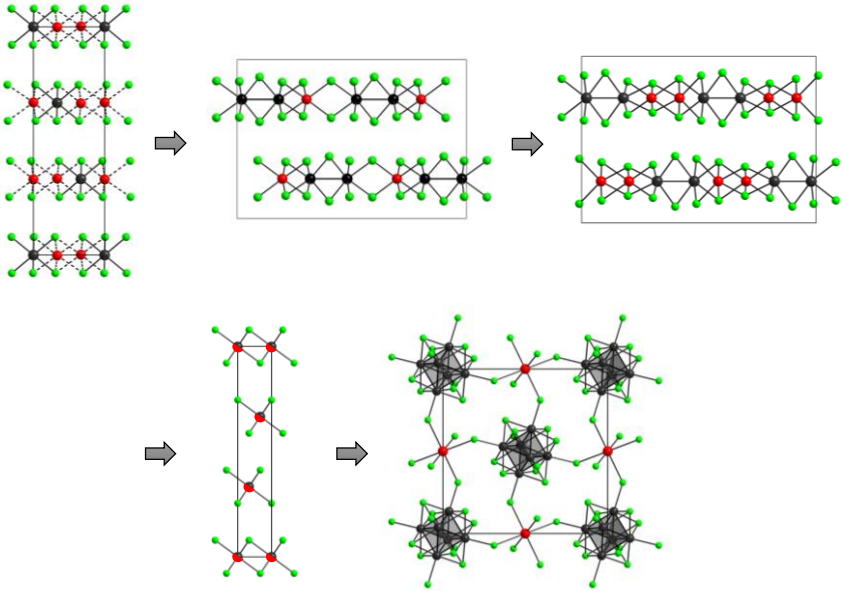

Dissertation

vorgelegt von

M. Sc. Agnieszka Moś-Hummel

Tübingen

2016

Reduction Studies on Tungsten Hexachloride

Reduktions Studien von Wolfram(VI)-Chlorid

Dissertation
der Mathematisch-Naturwissenschaftlichen Fakultät
der Eberhard Karls Universität Tübingen
zur Erlangung des Grades eines
Doktors der Naturwissenschaften
(Dr. rer. nat.)

vorgelegt von
M. Sc. Agnieszka Moś-Hummel
aus Oświęcim/Polen

Tübingen
2016

Gedruckt mit Genehmigung der Mathematisch-Naturwissenschaftlichen Fakultät der Eberhard Karls Universität Tübingen.

Tag der mündlichen Qualifikation: 28. Juli 2016
Dekan: Prof. Dr. Wolfgang Rosenstiel
1. Berichterstatter: Prof. Dr. H.-Jürgen Meyer
2. Berichterstatter: Prof. Dr. Eberhard Schweda

Die vorliegende Arbeit wurde von Oktober 2012 bis Juli 2016 am Institut für Anorganische Chemie der Eberhard-Karls-Universität Tübingen unter der Leitung von Prof. Dr. H.-Jürgen Meyer angefertigt.

Meinem Doktorvater

Herrn Prof. Dr. H.-Jürgen Meyer

danke ich herzlich für die Überlassung des interessanten Themas, die ständige Gesprächsbereitschaft, für die guten Arbeitsbedingungen und die weit reichenden Freiheiten bei der Arbeit.

Mein Dank gilt weiterhin

meinem zweiten Doktorvater, Prof. Dr. Eberhard Schweda für die stete Diskussionsbereitschaft und fachliche Unterstützung während meiner Promotion.

Dr. Markus Ströbele für seine Hilfe bei allen fachlichen Fragen und für Inspiration und Unterstützt bei der Lösung von Kristallstrukturen.

Dr. Jochen Glaser für die Durchführung der magnetischen Messungen und anregende Diskussionen auf diesem Gebiet.

Dr. Sylvio Indris (Karlsruher Institut für Technologie) für die durchgeführte und auswertete Mössbauerspektroskopie Messungen.

Prof. Dr. R. F. Fink. und Cristina Castro für die durchgeführten Quantenchemische Berechnungen.

Elke Nadler für die Hilfe bei die Durchführung von EDX Messungen.

Dr. Ronny Löffler für die Aufnahme von Bilder mit dem Rasterelektronenmikroskop.

Dr. Farzia Hossain für die Unterstützung bei der Anfertigung der NMR Messung.

Dem gesamten Arbeitskreis für das angenehme Arbeitsklima und ein guter Teamgeist.

Ich danke meinen Freunden für die Unterstützung in allen Phasen meiner Promotion.

Szczególnie dziękuję Danusi i Szymonowi D. za uśmiech, dobre słowo i okazane serce.

Ich danke ebenso Alex. K., Martin T., Johannes F., Maja O. und Oliver S. für Eure Unterstützung, Lächeln und unsere Zeit zusammen. Danke für die Jahre die wir gemeinsam verbracht haben.

Ich danke meine Schwiegereltern, die mich während des gesamten Doktorstudiums in jeder erdenklichen Weise unterstützt haben.

Besonderer Dank gilt meinen lieben Mann Thorsten. Ich danke Dir, dass Du immer bei mir warst, wenn ich Dich gebraucht habe. Danke dass du mich immer zum lächeln in schwere Momenten gebracht hast. Du hast mir immer Motivation gegeben und mich in jeden meinem Schritt unterstutzt. Danke für deine Liebe und dass du immer in mir geglaubt hast. Ich liebe Dich und widme dir diese Arbeit.

Dziękuję Babci Aleksandrze za pogodę ducha, którą mi przekazywała podczas wspólnych spotkań.

Dziękuję moim Siostrom, Gosi i Martusi, że zawsze mogłam na Was liczyć. Byłyście ze mną, gdy potrzebowałam Waszego wsparcia oraz Waszego dobrego humoru, który pozwalał zapomnieć o wszystkich troskach.

Kochani Rodzice, dziękuję Wam za bezgraniczną miłość, troskę i wsparcie. Jestem Wam bardzo wdzięczna za trud, jaki włożyliście w moje wychowanie oraz za wiarę we mnie. Dzieki Wam mogłam to wszystko osiagnąć. Kocham Was i to Wam dedykuję tę pracę.

Meinem Mann

Rodzicom

Introduction 1
Used Technics, Software and Chemicals 3

1. Used Technics 3
1.1. Powder Diffraction 3
1.2. Single Crystal Diffraction 3
1.3. Thermal Analysis 3
1.4. Magnetic Measurement 4
1.5. Energy Dispersive X-ray Spectroscopy 4
1.6. Mößbauer Spectroscopy 4
1.7. Nuclear Magnetic Resonance Spectroscopy 5
1.8. Preparations 5

2. Used Programs 6
2.1. Graphics 6
2.2. Powder Diffraction Analysis 6
2.3. Single Crystal Analysis 6
2.4. Quantum Chemical Calculations 6

3. Used Chemicals 7
Experimental Part 9

4. Reduction of Tungsten Hexachloride 9
4.1. Mn-W-Cl System 9
Thermal Analysis of Mn-W-Cl System 9
Synthesis of Products in Mn-W-Cl System 11
Characterization of Mn_xWCl_6 12
Characterization of MnW_2Cl_{10} 13
Characterization of $(Mn,W)_{1-x}Cl_2$ 15
Characterization of MnW_6Cl_{14} 16
Magnetic Measurement 16
Synthesis and Characterization of $Mn_{0.51}[W_2O_2Cl_6]$ 18
4.2. Fe-W-Cl System 21
Thermal Analysis of Fe-W-Cl System 21
Synthesis 22

Characterization of Fe_xWCl_6 24
Characterization of FeW_2Cl_{10} 27
Characterization of $Fe_2W_2Cl_{10}$ 29
Characterization of $(Fe,W)_{1-x}Cl_2$ 29
Characterization of FeW_6Cl_{14} 31
Magnetic Measurement 32
Mössbauer Spektroskopie 34
Quantum Chemical Calculations 36
4.3. Co-W-Cl System 41
Thermal Analysis of Co-W-Cl System 41
Synthesis 43
Characterization of Co_xWCl_6 44
Characterization of CoW_2Cl_{10} 45
Characterization of "$Co_2W_2Cl_{10}$" 46
Characterization of $(Co,W)_{1-x}Cl_2$ 46
Characterization of CoW_6Cl_{14} 46
Magnetic Measurement 47
4.4. Ni-W-Cl System 49
Thermal Analysis of Ni-W-Cl System 49
Synthesis of the Products in Ni-W-Cl System 50
Characterization of $(Ni,W)_{1-x}Cl_2$ 51
Characterization of NiW_6Cl_{14} 52
4.5. Cu-W-Cl System 53
Thermal Analysis of Cu-W-Cl System 53
Synthesis of Products in Cu-W-Cl System 54
Characterization of Cu_xWCl_6 56
Characterization of α-$Cu_2W_2Cl_{10}$ and β-$Cu_2W_2Cl_{10}$ 63
Characterization of $Cu_2W_6Cl_{14}$ 66
4.6. Reduction of WCl_6 with Copper and Hexachlorobenzene 67
Synthesis 67
Characterization of $Cu[W_6CCl_{18}]$ 68
Characterization of $Cu(C_2H_6OS)_6[W_6CCl_{18}]$ 71

Characterization of $Cu(C_2H_6OS)_4[W_6CCl_{18}]_2$ 73
Summary 75
Zusammenfassung 79
List of Publications 83
Acknowledgment 84
References 85

Introduction

Metal-rich halide cluster compounds are known for various group 4 – 7 metal halides (X = Cl, Br, I). This work is focussed on tungsten chloride compounds. The first distinct geometry is based upon a central tungsten atom surrounded by six chlorido ligands to form an octahedral WCl_6 unit, which is known to form two modifications, α-WCl_6[1,2] and β-WCl_6[2,3] (Figure 1. up, right). This motive is also present in WCl_5 compound.[4] The structure of WCl_5 contains two edge-bridged WCl_6 octahedra forming a Cl_4W-Cl_2-WCl_4 dimer (Figure 1. up, middle). The crystal structure of WCl_4 (Figure 1. up, right) is represented by chains of edge-sharing WCl_6 octahedra with alternating short and long distances between tungsten atoms.[5,6]

A distinct structural pattern is observed in the structure of W_6Cl_{12} where tungsten atoms form an octahedral metal cluster (Figure 1. bottom, left).[7] Each cluster face is capped by a chloride ligand, with eight of them are forming a cube (W_6Cl_8). Six additional chlorido ligands are situated in apical positions of the octahedral cluster, with four of them having a bridging functionality with four other clusters $(W_6Cl_8^{i})Cl_2^{a}Cl_{4/2}^{a\text{-}a}$ (a - outer, i - inner, a-a - outer-outer bridging).

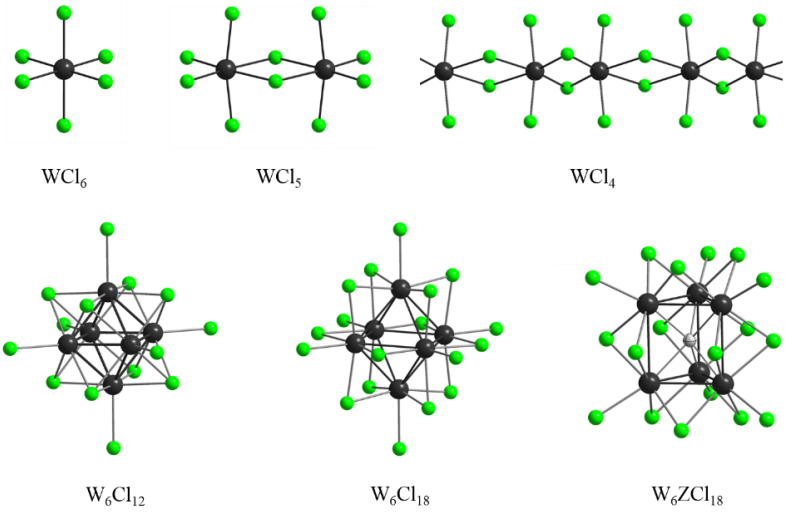

Figure 1. Examples of tungsten chloride main structures. In W_6ZCl_{18} cluster Z symbolize carbon or nitrogen ion.

The third geometry presented in W_6Cl_{18} is shown in the Figure 1 (bottom, middle). Structure similarity of W_6Cl_{18} and W_6Cl_{12} is based on an octahedron built up from tungsten atoms.[8] To get a better comparison of these two cluster archetypes (W_6X_8) and (W_6X_{12}) it favorable to write $(W_6Cl_8^i)Cl_2^aCl_{4/2}^{a-a}$ for W_6Cl_{12} and $(W_6Cl_{12}^i)Cl_6^a$ for W_6Cl_{18}. In W_6Cl_{18} each tungsten cluster edge is capped by a chloride ligand, forming a (W_6Cl_{12}) cluster. Additional six chloride anions are terminal atoms from each tungsten atom.

Another interesting example from tungsten compounds is carbon centered trigonal prismatic tungsten cluster W_6CCl_{18} (Figure 1. bottom, right).[9,10] This cluster is known as a neutral species, but can also occur as an anion $[W_6ZCl_{18}]^{n-}$ (n = 1, 2 ,3) containing carbon or nitrogen (Z) in the center of a trigonal prism build up from tungsten atoms.[11,12] Twelve chloride ligands have μ_2-bridging functionality and six chlorides act as terminal Cl^a ligands, all together forming the $[(W_6CCl_{12}^i)Cl_6^a]$ cluster.

Preparations of metal-rich halide cluster compounds are usually performed by high-temperature solid state techniques. Reactions depart from a metal halide which is reduced by the same metal or by an effective reduction agent, such as alkali metals and placed in fused quartz ampoules for several days at temperatures in excess of 700 °C.

The problem of many transition elements such as tungsten is, that they behave inert in solid state reactions. Several strategies were explored to overcome this problem and to be able to perform kinetically controlled reactions, such as the employment of a salt melt[13] or reduction within a Lewis acidic ionic liquid[14]. Until now, there has been no effective way to investigate whole metal-rich halides systems and to understand their transformation reaction dynamics.

The present work is focusing on thermal investigations by using of differential scanning calorimetry (DSC) performed on *M*-W-Cl (*M* = Mn, Fe, Co, Ni, Cu) systems. On this way it was possible to synthesize series of new compounds in metal-rich halide systems. The combined method of DSC and X-ray diffraction is used to investigate the reduction of tungsten in WCl_6 from oxidation state +6 to +2. The reaction with reducing metal involves a cascade of intermediate compounds until a thermodynamically stable product is formed. The mixture of WCl_6 and metal *M* (*M* = Mn, Fe, Co, Ni, Cu) is placed in a DSC container to undergo thermal analysis. Thermal effects shown in the DSC diagram are analysed and individual reaction, are performed meeting the requirements concerning temperature and estimated sample composition based on observed DSC signal. Finally new structure determination from X-ray diffraction data are performed.

Used Technics, Software and Chemicals

1. Used Technics

1.1. Powder Diffraction

Powder X-ray diffraction data (XRD) of crystalline powders of products were collected at room temperature with a *Stoe StadiP diffractometer* using Ge-monochromatized Cu-$K_{\alpha 1}$ radiation (λ = 1.540598 Å). Standard measurements were taken in the 2θ range between 5 ° and 100 ° in step, of 0.02 °.

1.2. Single Crystal Diffraction

Single-crystals of obtained products were selected and mounted on the tip of a glass fiber for an intensity measurement using a single-crystal X-ray diffractometer (*Stoe, IPDS 2T*, Darmstadt, Germany), equipped with (graphite) monochromated Mo-K_α radiation (λ = 0.71073 Å) at room temperature. Raw data intensities were corrected for Lorentz factors and polarization effects by the IPDS software. Absorption effects were corrected by *X-Red/X-Shape* program of the *STOE software*.

A single crystal of MnW_2Cl_{10} was selected and mounted on the tip of a glass fiber for an intensity measurement with a single-crystal X-ray diffractometer (*Bruker APEXII DUO sealed-tube CCD*) with Mo-K_α radiation. Raw data were reduced and scaled with the *program SAINT*. Corrections for absorption effects were applied by using *SADABS*.[15]

1.3. Thermal Analysis

Mixtures of β-WCl_6 and metal powder were enclosed (screwed) into a gold plated (5 µm) steel container (with inserted nuts) (100 µL, *BFT 94*, *Bächler Feintech AG, Switzerland*) in a dry argon atmosphere (glovebox) (Figure 2). The gas-tight container was standard heated with a rate of 2 K/min in a differential scanning calorimeter (*DSC 204 F1 Phoenix, Netzsch*) from room temperature to suitable temperature °C (depending on the system).

Figure 2. Closed DSC container (left) and three separate parts: empty container, golden seal and a metal cap (right).

1.4. Magnetic Measurement

Powdered samples of obtained samples were loaded into gelatin capsules in an argon atmosphere (glovebox) and their magnetic susceptibilities were recorded with a *SQUID magnetometer* (superconducting quantum interference device; *Quantum Design, MPMS*) in a magnetic field between 50 Oe and 10000 Oe in the temperature range 5 K ≤ T ≤ 300 K with progressive steps (the higher the temperature the bigger the steps between collected data points). The recorded susceptibilities were fitted following an extended Curie-Weiss law ($\chi = C / (T - \theta) + \chi_0$).

1.5. Energy Dispersive X-ray Spectroscopy

Energy dispersive X-ray spectroscopy (EDX) data were collected with a *transmission electron microscope HITACHI SU8030* at 25.0 kV. A qualitative analysis of crystalline powders revealed the presence of *M*, W, and Cl (*M* = Mn, Fe, Co, Ni) and the absence of oxide and other elements. The picture of $(Fe,W)_{1-x}Cl_2$ compound was made with an *HITACHI SU8030* and this of $(Ni,W)_{1-x}Cl_2$ was made with an *Scanning Electron Microscope (SEM) JEOL JSM-6500F*.

1.6. Mößbauer Spectroscopy

^{57}Fe Mössbauer spectroscopic measurements were performed in transmission mode at room temperature using a constant acceleration spectrometer with a *^{57}Co(Rh) source*. Isomer shifts are given relative to that of *α-Fe at room temperature*. Measurements were done for products from the Fe-W-Cl system. $FeCl_2$ was used as a reference, appearing with the $CdCl_2$ and CdI_2 structure (high pressure modification) in approximate 1:2 ratio (estimated form the XRD pattern).

1.7. Nuclear Magnetic Resonance Spectroscopy

A ^{13}C-NMR spectrum of $Cu(C_2H_6OS)_6[W_6CCl_{18}]$ was recorded using a *Bruker AvanceII+400 NMR spectrometer* equipped with a 5 mm *QNP (quad nucleus)* probe head operating at 100.13 MHz (^{13}C). Chemical shift is given in δ value in ppm relative to external $SiMe_4$ (^{1}H, ^{13}C, ^{29}Si). $^{13}C\{^1H\}$ UDEFT NMR (DMSO): δ = 280.7 $[W_6CCl_{18}]$.

1.8. Preparations

Preparations were done in a glovebox under argon atmosphere with amounts of oxygen and water below 1 ppm.

Mixtures of β-WCl_6 and metal powder, with total masses around 150 mg were prepared in an argon atmosphere (glovebox), placed into homemade quartz ampules (inner diameter: 0.7 cm, length: 2.5–3 cm) (Figure 3, left)), and sealed therein under vacuum while cooling the mixtures with liquid nitrogen. Loaded ampules were placed into *Simon-Müller* (Figure 3, right) furnace at a temperature, which was individually revised in order to obtain well-crystallized, high yield products or single crystals.

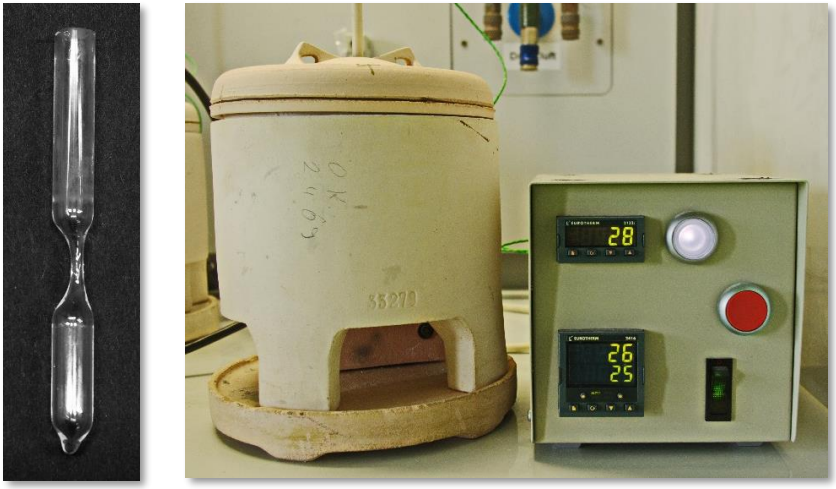

Figure 3. Picture of homemade ampule (left) and Simon Müller furnace (right).

2. Used Programs

2.1. Graphics

Pictures of presented crystal structures were created with the program *Diamond 3.2k*.
Collective pictures of powder diffractions were created with the use of *WinXPow Graphic 3.0.2.2* program.
Plots presenting thermal diagrams (DSC), magnetic measurements and change of unit cell volume were done with *OriginPro 8.5.0 SR1*. DSC plots were additionally corrected for a baseline with a Peak Analyzer function.

2.2. Powder Diffraction Analysis

Powder patterns were refined by global refinement using the *WinPlotr (FullProf Suite)*[16] program package (for isotypic compounds) and new crystal structures were indexed, solved by direct methods with the use of *EXPO 2009*[17], and then refined with the *WinPlotr (FullProf Suite)*.

2.3. Single Crystal Analysis

Crystal structure solutions were performed with *direct method (SHELXS)*, followed by full-matrix least square structure refinements *(SHELXL-97 and SHELXL-2014)*[18].

2.4. Quantum Chemical Calculations

The bonding characteristics of $[W_2Cl_{10}]^{2-}$ and $[W_2Cl_{10}]^{4-}$ were investigated by spin unrestricted DFT calculations performed with the program *TURBOMOLE6.6*.[19,20] The crystal structure data of FeW_2Cl_{10} and $Fe_2W_2Cl_{10}$ were used as a starting point for the geometry optimization of both fragments and no symmetry constrains were imposed. The DFT calculations were carried out using the *B3-LYP*[21] functional, the *RI*[22, 23, 24] and *MARIJ*[25] options as well as the *def2-TZVP*[26] basis set, the *Stuttgart small core pseudopotential*[27] and the *COSMO module*[28,29,30] which was employed to stabilize the anions. The geometry optimized fragments were also analysed via *numerical vibrational analysis*,[31] in order to verify the nature of the stationary points found by means of the geometry optimization.

3. Used Chemicals

α-WCl_6 (Sigma Aldrich, 99.9%) was purified by sublimation (fused silica tube at 180 °C) prior to use, yielding the high temperature modification, β-WCl_6.

Obtained β-WCl_6 was reduced during studies with the following chemicals:

- Mn (Alfa Aesar, 325 mesh, 99.95 %)
- Fe (Ventron, 325 mesh, 99.5 %)
- Co (Riedel-de Haen, 99.5 %)
- Ni (Riedel-de Haen, 99.8 %)
- Cu (Merck, 99.9 %)
- C_6Cl_6 (Sigma Aldrich, 99 %)

For copper products obtained from solution dimethylsulfoxid (DMSO, Roth, > 99.5 %) was used.

Experimental Part

4. Reduction of Tungsten Hexachloride

4.1. Mn-W-Cl System

Thermal Analysis of Mn-W-Cl System

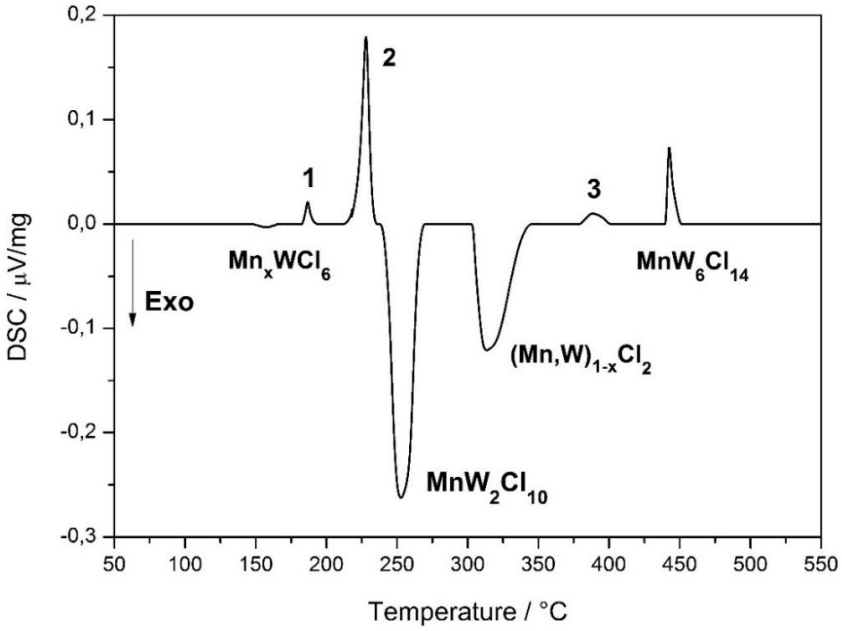

Figure 4. Thermal (DSC) effects and assigned compounds obtained when heating a mixture of β-WCl_6 and manganese powder at a rate of 2 °K / min. Numbered effects correspond to the sublimation of WCl_6 (1), formation of a melt of WCl_6 (2), and sublimation of WCl_4 (3).

The thermal scanning experiment described herein is designed to study the Mn-W-Cl system by reacting WCl_6 with an increasing amount of Mn powder. In course of this reaction we expect the formation of new Mn-W-Cl compounds under release of $MnCl_2$ as a side phase. The total amount of Mn powder is calculated to allow (at least) the reduction of tungsten from W^{6+} (in WCl_6) to W^{2+}. The progressive reaction is driven by temperature increase. The heating rate, optimized at 2 °K per minute, is crucial for the separation of thermal effects monitored in the DSC, and thus, for the resolution of the measurement which has to be adjusted to the reaction

speed of the given system. A 1:2 molar mixture (ca. 40 mg) of β-WCl_6 and manganese powder was heated from room temperature to 550 °C. Monitored thermal effects were assigned by powder X-ray diffraction patterns from separately prepared samples.

The reaction between WCl_6 and manganese powder involves a series of signals in the DSC measurement (Figure 4.). An increasing amount of metal is mobilized with increasing temperature (and time) to form more and more reduced tungsten species in the *M*-W-Cl system (*M* =Mn,[32] Fe,[33,34,35] Co,[33,36] Ni, Cu[37]). Subsequent powder XRD studies are used to assign and identify reaction products corresponding to the observed thermal effects. XRD powder patterns of new compounds are displayed in Figure 5.

The first exothermic DSC effect in the Mn-W-Cl system is near 150 °C and represents the structural transformation of trigonal β-WCl_6 into rhombohedral α-WCl_6 with a simultaneous intercalation of manganese into the structure of WCl_6. The product can be described as Mn_xWCl_6 with a small, variable amount of manganese ions in the structure. The following two endothermic effects can be addressed to the sublimation and melting of WCl_6, respectively, as has been confirmed in separate heating experiments of WCl_6 in a silica tube (eye inspection) and by DSC.

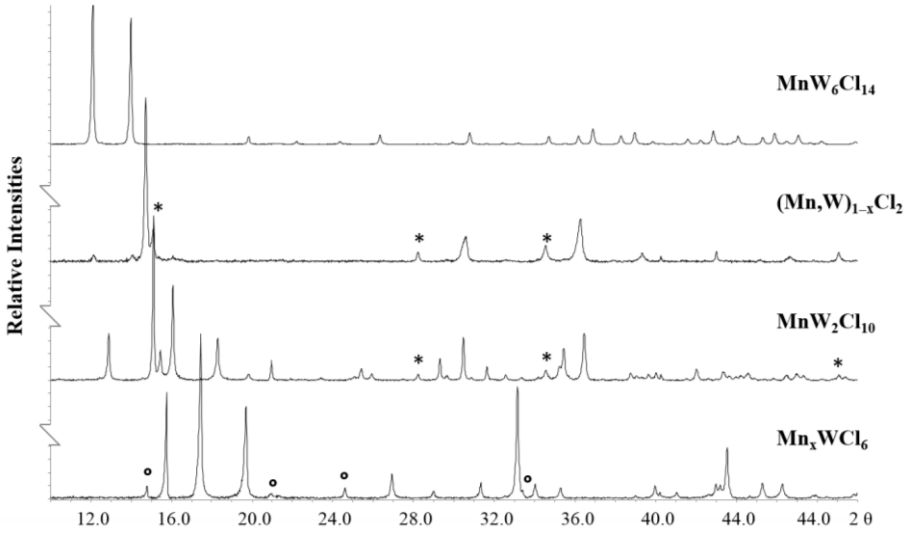

Figure 5. Selection of X-ray powder diffraction patterns of compounds obtained in the Mn-W-Cl system with their respective preparation temperature and assigned formula given. Side phases are marked for $WOCl_4$ (o) and $MnCl_2$ (*).

The second exothermic effect is obtained near 250 °C and can be addressed to the formation of MnW_2Cl_{10}. Single-crystals of MnW_2Cl_{10} were obtained, appearing as green-black plates.
The following exothermic effect above 300 °C can be explained with the formation of a compound, which is addressed as $(Mn,W)_{1-x}Cl_2$, whose crystal structure can be related to a defect $MnCl_2$ ($CdCl_2$-type) structure. The next endothermic effect near 400 °C is addressed to the sublimation of WCl_4 under given conditions. Finally the formation of MnW_6Cl_{14} is obtained near 450 °C. This compound can be indexed in accord to the well-known $PbMo_6Cl_{14}$ structure.[38]

Synthesis of Products in Mn-W-Cl System

Preparations of compounds were carried out following conditions adapted from DSC measurement. Mixtures of β-WCl_6 and manganese powder, with total masses around 150 mg were prepared in an argon atmosphere (glovebox), placed into homemade quartz ampules (inner diameter: 0.7 cm, length: 2.5–3 cm), and sealed therein under vacuum while cooling the mixtures with liquid nitrogen. All compounds behave sensitive to moist air.
Later on, reaction conditions were individually revised in order to obtain well-crystallized high yield products or single crystals. Individually optimized reaction conditions are given as follows:

Mn_xWCl_6 was obtained as a black powder after heating β-WCl_6 with variable amounts of manganese powder with y = 0.1–15 fold molar proportions at 125 °C for 7 d (total mass: ca. 450 mg). Only a small fraction (x) of Mn was incorporated into the structure, while most of the employed elemental Mn (y) remained as a residue (z), explained in Equation (1). Mn_xWCl_6 has a phase width (x) as evidenced from the refinement of the unit cell parameters using powder XRD.

$$WCl_6 + y\ Mn \rightarrow Mn_xWCl_6 + z\ Mn \quad (1)$$

MnW_2Cl_{10} was obtained as green-black crystal plates after heating a mixture of β-WCl_6 with manganese powder in a 1:1 molar ratio at 265 °C for 500 h following Equation (2):

$$2\ WCl_6 + 2\ Mn \rightarrow MnW_2Cl_{10} + MnCl_2 \quad (2)$$

$(Mn,W)_{1-x}Cl_2$ was obtained as a dark-brown powder after heating a mixture of β-WCl_6 with manganese powder in 1:2 molar ratio at 330 °C for 3 d, following Equation (3):

$$2\ WCl_6 + 4\ Mn \rightarrow 2\ (Mn,W)_{1-x}Cl_2 + 2\ MnCl_2 \quad (3)$$

MnW_6Cl_{14} was obtained as a brown powder after heating β-WCl_6 with manganese powder in a 1:2 molar ratio at 500 °C for 2d, following Equation (4):

$$6\ WCl_6 + 12\ Mn \rightarrow MnW_6Cl_{14} + 11\ MnCl_2 \quad (4)$$

Characterization of Mn_xWCl_6

Two modifications have been reported for WCl_6. The rhombohedral low temperature modification (α-WCl_6) transforms irreversibly into the trigonal modification (β- WCl_6) when being heated above 150 °C.[2,3] Our experiments departed from trigonal β-WCl_6, which was obtained after sublimation of (commercial) α- WCl_6. When β-WCl_6 is heated with manganese powder the phase-transition is reversed, thereby leading to an intercalated structure of α-WCl_6, which we assign as Mn_xWCl_6.

Similar M_xWCl_6 compounds (M = Fe and Co) have been described.[35,36] All these experiments have shown that a small but variable amount of metal ions (M) can be incorporated into the WCl_6 structure, especially under prolonged heating with excess of metal powder at constant temperature. A single-crystal study has been performed for Fe_xWCl_6 with x in the order of 0.1.[36] The structure can be described as a cubic close packing of chloride with tungsten ions occupying (1/3) octahedral sites in every other layer (α-WCl_6-type). Iron ions occupy octahedral voids in tungsten ion layers in a disordered fashion (Fe_xWCl_6). The same type of incorporation into α-WCl_6 can be expected for Mn_xWCl_6. A progressive intercalation of manganese ions into the structure of WCl_6 leads to an increase of the unit cell volume of Mn_xWCl_6 as shown in Figure 6. Lattice constants and corresponding unit cell volumes are calculated from indexed powder XRD patterns, showing an increase of the unit cell of Mn_xWCl_6 with increasing x in all directions.

With respect to a hexagonal setting the a axis changes within range from 6.1416(3) to 6.213(1) Å and the c-axis from 16.829(1) to 17.149(4) Å, leading to an increase of the unit cell volume by 23.5 $Å^3$ (549.74(5) – 573.3(2) $Å^3$). These results show that the unit cell volume of Mn_xWCl_6 is much larger than the volume reported for α-WCl_6 (V = 543.3(1) $Å^3$).[34]

The observation of this compound can be interpreted as the beginning of a usual reduction of WCl_6, in which the reducing agent is incorporated to form Mn_xWCl_6, similar to $LiWCl_6$[39].

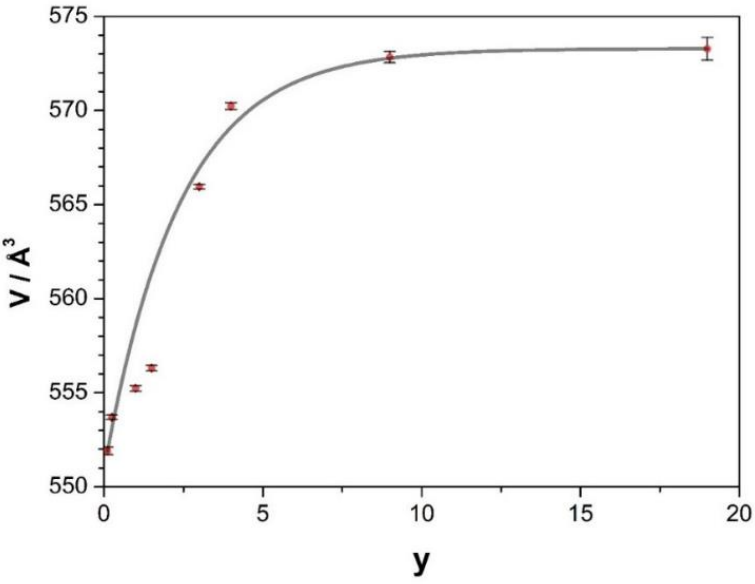

Figure 6. Unit cell volume increase of Mn_xWCl_6 as a function of the amount (y) of manganese powder used in reactions. The metal was employed in excess (y).

Characterization of MnW_2Cl_{10}

Crystalline powders of MnW_2Cl_{10} were handled in an argon atmosphere because they tend to decompose in moist air. The crystal structure of MnW_2Cl_{10} was refined with a monoclinic crystal system ($C2/c$) based on single-crystal XRD data, with some results given in Table 1. An isotypic crystal structure is reported for MW_2Cl_{10} (M = Fe, Co).[33,35,36] A characteristic fragment in the structure of MnW_2Cl_{10} is the motive of an edge-sharing bi-octahedron, known from the neutral $[W_2Cl_{10}]$ species in the WCl_5 structure.[4] In MnW_2Cl_{10} adjacent tungsten atoms are moved from their octahedral centers to approach each other resulting in a short W–W distance of 2.6994(3) Å, which can be well related with a $[W_2Cl_{10}]^{2-}$ ion. The corresponding

W–W distance in the structure of WCl_4 are equal $d_{W–W}$ = 2.688(2) Å[5] and $d_{W–W}$ = 2.713(3) Å[6].

The structure of MnW_2Cl_{10} can be described as a layered arrangement derived from a hexagonal close packing (hcp) of chloride ions, stacked along the *c* axis direction, as shown in the projection in Figure 7 (top). Octahedral voids in every second interlayer are occupied with manganese ions by 1/5 and tungsten ions by 2/5. Additional 2/5 octahedral voids in every second interlayer remain to be empty.

Table 1. Crystallographic data and structure refinement of MnW_2Cl_{10}.

Formula weight	780.85
Temperature	293(2) K
Wavelength	71.073 pm
Crystal system	monoclinic
Space group	*C 2/c* (No. 15)
Unit cell dimensions	*a* = 6.1663(2) Å
	b = 16.9028(5) Å
	c = 11.8285(4) Å
Volume	1214.50(7) Å^3
Z	4
Density (calculated)	4.270 g/cm^3
Absorption coefficient	22.134 mm^{-3}
F(000)	1379
Crystal size	0.15 x 0.15 x 0.3 mm^3
Reflections collected	10442
Independent reflections	1841 (R_{int} = 0.0259)
Goodness-of-fit on F^2	1.123
Final R indices [I>2sigma(I)]	R_1 = 0.0191, wR_2 = 0.0436
R indices (all data)	R_1 = 0.0216, wR_2 = 0.0444
Largest diff. peak and hole	2.072 and -2.100 e·Å^{-3}

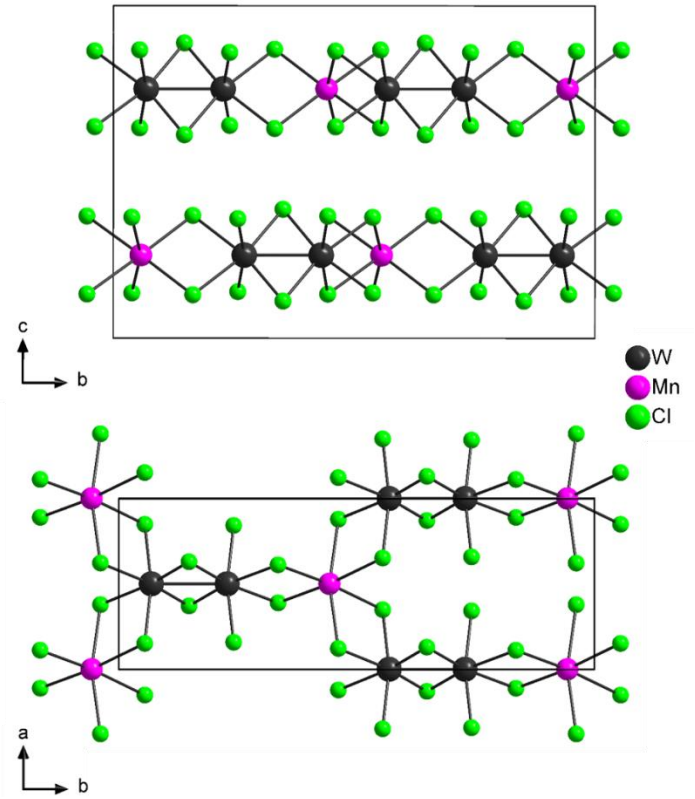

Figure 7. Crystal structure of MnW_2Cl_{10}. The top projection represents one single Cl–(Mn,W)–Cl sandwich layer and the bottom projection displays two of these layers stacked in the unit cell along the *c*-axis.

Characterization of $(Mn,W)_{1-x}Cl_2$

The exothermic effect appearing around 320 °C in the DSC measurement is assigned to the formation of a compound denoted as $(Mn,W)_{1-x}Cl_2$. In comparison to corresponding compounds with *M* = Fe, Co, Ni the compound with *M* = Mn behaves less stable against moist air and water. The excess of manganese powder used in the reaction could not be completely removed from the sample and therefore magnetic data were not collected. Moreover, an alternative way of synthesis is not available for this compound. According to our X-ray powder diffraction studies the crystal structure of $(Mn,W)_{1-x}Cl_2$ appears related to the $MnCl_2$ ($CdCl_2$-type) structure (*R*-3*m*).

Due to some additional reflections in the XRD pattern (with $I < 1/10\ I\text{max}$) the presence of a super-structure cannot be ruled out. A phase-width has to be considered due to significant variations of lattice parameters obtained from sample to sample. Hexagonal indexing of the powder XRD pattern of a representative sample yielded $a = b = 3.4222(3)$, $c = 18.0405(3)$ Å. The obtained unit cell volume of $(Mn,W)_{1-x}Cl_2$ with V = 183.12(5) Å^3 is much smaller, than the corresponding volume of $MnCl_2$ (V = 209.79 Å^3)[40].

The composition of a sample of $(Mn,W)_{1-x}Cl_2$ was analyzed as $(Mn_{0.47}W_{0.36})Cl_2$ by EDX analysis. When manganese was in divalent and tungsten in trivalent oxidation state the corresponding charge balanced phase could be described as $(Mn_{1-y}W_{2/3y})Cl_2$. A variation of y would explain small changes of the unit cell volume obtained for this phase.

Characterization of MnW_6Cl_{14}

The last effect monitored in DSC corresponds to the formation of a dark gray crystalline powder, identified as the new compound MnW_6Cl_{14}. The XRD pattern of the compound was indexed isotypically to the structure of $PbMo_6Cl_{14}$,[38] consistent with a cubic crystal system with $a = 12.650(1)$ Å. The arrangement of Mn^{2+} and $[(W_6Cl_8^i)Cl_6^a]^{2-}$ cluster ions in the structure follows the motif of the arrangement of Na^+ and Cl^- ions in the structure of NaCl. MnW_6Cl_{14} is moderately stable in air and dissolves in water to yield a brown solution.

Magnetic Measurement

Magnetic susceptibility measurements were performed for MnW_2Cl_{10} and MnW_6Cl_{14}. Both compounds show paramagnetic behavior, as presented in Figure 8 and Figure 9. The fit with an extended Curie-Weiss law yields 5.72 μ_B for MnW_2Cl_{10} and 5.96 μ_B for MnW_6Cl_{14} per formula unit, consistent with five unpaired electrons (5.92 μ_B according to spin-only).

The inset in Figure 8 and Figure 9 ($1/\chi$ vs. T) shows almost perfect linearity according to the paramagnetic behavior of both compounds. Thus, for MnW_2Cl_{10} and MnW_6Cl_{14} we can consider (d^5) Mn^{2+} ions and essentially diamagnetic cluster cores for $[Cl_5W–WCl_5]^{2-}$ and $[W_6Cl_{14}]^{2-}$.

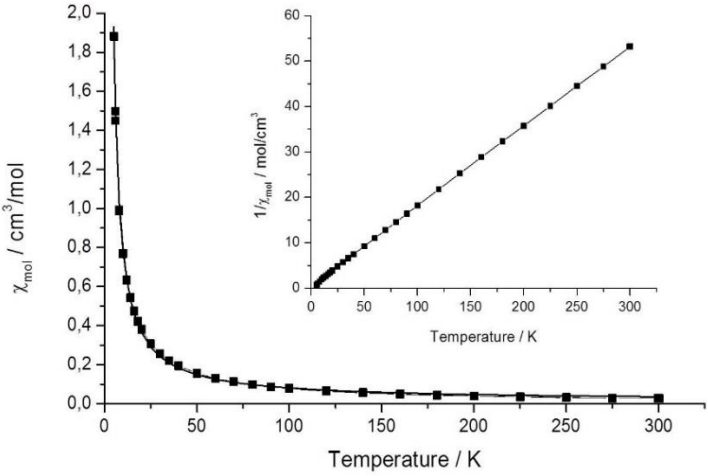

Figure 8. The magnetic susceptibility of MnW_2Cl_{10} in a magnetic field of 50 Oe vs. temperature.

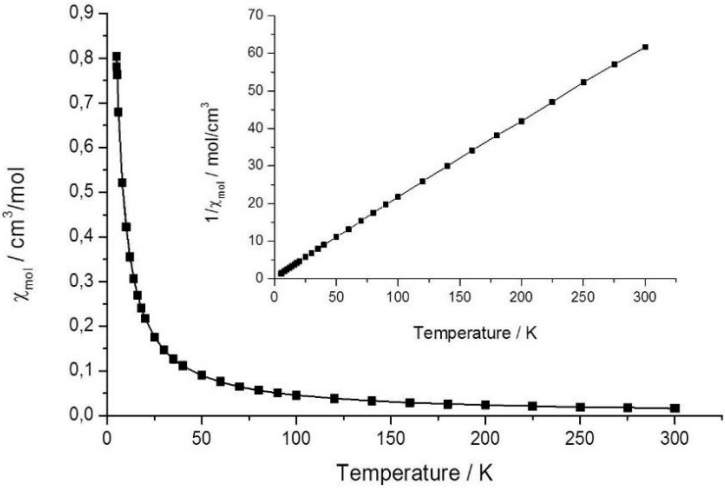

Figure 9. Magnetic susceptibility of MnW_6Cl_{14} in a magnetic field of 100 Oe vs. temperature.

Synthesis and Characterization of $Mn_{0.51}[W_2O_2Cl_6]$

$Mn_{0.51}[W_2O_2Cl_6]$ was obtained as a byproduct during the reaction of WCl_6 with manganese powder. Dark violet lustrous needles of $Mn_{0.51}[W_2O_2Cl_6]$ were placed into glass fiber for an intensity measurement using a single-crystal X-ray diffractometer at room temperature. Details of structure refinements are presented in Table 2 and 3.

Table 2. Single crystal structure and refinement data of $Mn_{0.51}[W_2O_2Cl_6]$.

Formula weight	667.34
Temperature, Wavelength	293(2) K, 71.073 pm
Crystal system	monoclinic
Space group	*C2/m*
Unit cell dimensions	*a* = 12.961(2) Å
	b = 3.7703(2) Å
	c = 10.114(8) Å
	β = 114.75(7) °
Volume	448.9(7) $Å^3$
Z	2
Density (calculated)	4.937 g/cm^3
Absorption coefficient	28.673 mm^{-1}
F(000)	582
Crystal size	0.2 x 0.02 x 0.02 mm^3
Theta range for data collection	2.217 to 24.956°
Reflections collected	1738
Independent reflections	452 ($R_{(int)}$ = 0.0392)
Goodness-of-fit on F^2	1.051
Final R indices [I > 2σ(I)]	R1 = 0.0386, wR2 = 0.0927
R indices (all data)	R1 = 0.0407, wR2 = 0.0947
Largest diff. peak and hole	1.817 and -1.575 e·$Å^{-3}$

$Mn_{0.51}[W_2O_2Cl_6]$ crystallizes monoclinic in the space group *C2/m*. One of the basic building blocks in the structure are $[W_2O_{4/2}Cl_6]$ units, which are build up from two edge-sharing WO_2Cl_4 octahedra, connected via two chloride atoms. Peaks of octahedras are connected through oxygen atoms creating endless chains. Between strands Mn^{2+} ions are located and connect them to layers. Manganese cations are trigonal prismatic coordinated by the terminal Cl atoms of the negative $[W_2O_{4/2}Cl_6]$ (Figure 10). Mn–Cl distances are separated in two groups of two short bonds $d_{Mn\text{-}Cl}$ = 2.293(8) and 2.36(1) Å, and four long ones $d_{Mn\text{-}Cl}$ = 2×2.796(6) and 2×2.893(8) Å, what shows the distortion of the trigonal prism. The position of manganese atom in the structure is not fully occupied and equals 0.51(1). Other cases with a similar structure to $Pb_{0.55}[W_2O_2Cl_6]$ and $Hg_{0.55}[W_2O_2Cl_6]$ were reported by J. Beck et. al.[41] where, like in $Mn_{0.51}[W_2O_2Cl_6]$, also divalent cations are present. In all cases cation positions are only partially occupied, what leads to the formal oxidation state +4.49 for the W atoms in $Mn_{0.51}[W_2O_2Cl_6]$, and +4.45 in lead and mercury compounds.

Table 3. Atomic coordinates (x 10^4) and equivalent isotropic displacement parameters (pm^2 x 10^{-1}) for $Mn_{0.51}W_2O_2Cl_6$. U(eq) is defined as one third of the trace of the orthogonalized U^{ij} tensor.

	x	y	z	U(eq)	S.O.F.
W(1)	0.761(1)	0	0.6490(1)	36(1)	1
Mn(1)	0.2590(6)	0	0.148(8)	56(2)	0.505
Cl(1)	0.2795(3)	0	0.7935(4)	42(1)	1
Cl(2)	0.1247(3)	0	0.4479(4)	40(1)	1
Cl(3)	0.658(3)	0	0.8818(4)	46(1)	1
O(1)	0.799(5)	- ½	0.6582(8)	19(2)	1

Interatomic distances between tungsten atoms in the manganese compound are equal $d_{W–W}$ = 2.827(3) Å. In the case of lead and mercury compounds distances between tungsten atoms are congruent and equal $d_{W–W}$ = 2.8370(4) Å and $d_{W–W}$ = 2.8442(8) Å respectively. The motive of edge-shearing bi-octahedron $[W_2O_{4/2}Cl_6]$ corresponds to a motive of $[W_2Cl_{10}]$ known from WCl_4 having a separation of tungsten atoms $d_{W–W}$ = 2.688(2) Å[5] and 2.713(3) Å[6]. Thus, W−W interatomic distances around 2.7 Å in WCl_4 may be addressed with an oxidation state of

+4 for tungsten atoms. The corresponding distance in $Mn_{0.51}[W_2O_2Cl_6]$ appears longer and should be addressed to a higher oxidation state of tungsten.

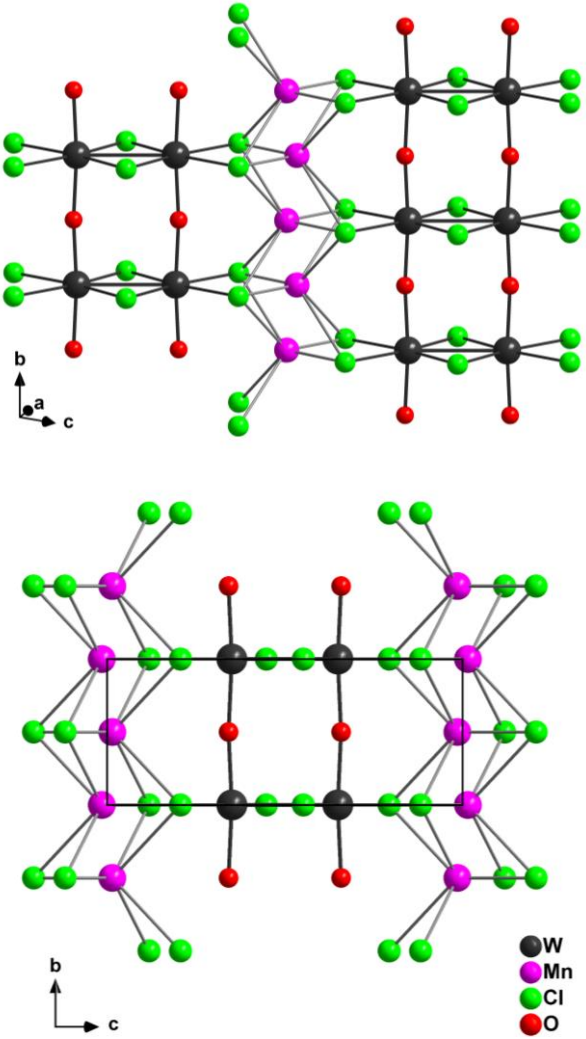

Figure 10. Crystal structure of $Mn_{0.51}[W_2O_2Cl_6]$. In both pictures two neighboring strands are shown, together with the coordination of the cations and chains build out of $[W_2O_{4/2}Cl_6]$ units.

4.2. Fe-W-Cl System

Thermal Analysis of Fe-W-Cl System

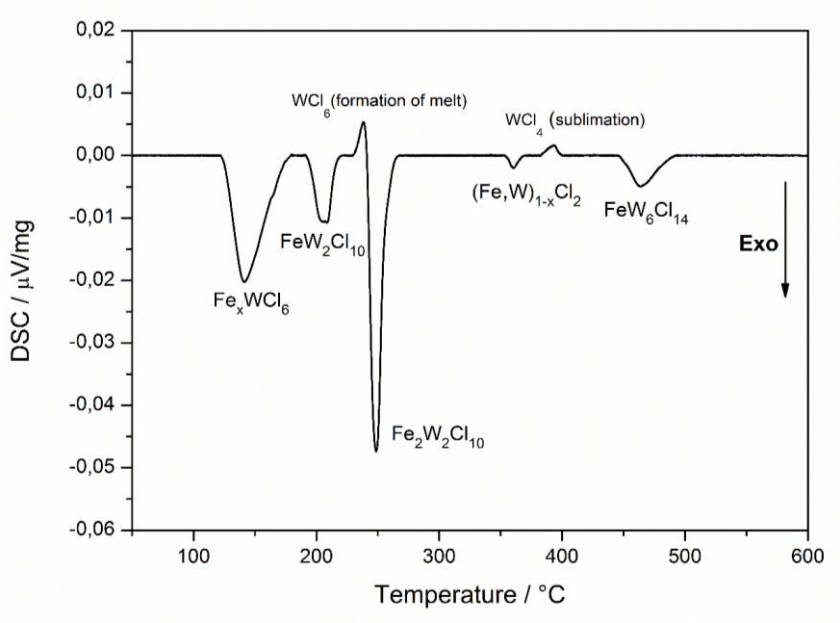

Figure 11. Thermal effects during the reduction of WCl_6 with Fe powder at increasing temperature.

The next studied reduction element is iron. The reduction of WCl_6 with iron powder was performed according to the nominal reaction:

$$6\ WCl_6 + 12\ Fe \rightarrow FeW_6Cl_{14} + 11\ FeCl_2 \qquad (5)$$

The starting mixture was fused into a DSC container and heated up to 600 °C in a heating rate 2 °/ min with the resulting differential thermogram displayed in the Figure 11.

Trigonal β-WCl_6 was used as a starting material for the reaction with elemental iron powder. The first exothermic effect represents the (irreversible) formation of rhombohedral α-WCl_6. Separate reactions of β-WCl_6 with iron powder for an expended time span revealed a significant lattice expansion of rhombohedral WCl_6, so that a variable intercalation of iron into the structure of α-WCl_6 can be assumed to yield Fe_xWCl_6. The following two exothermic effects displayed in the DSC experiment are explained with the formation of FeW_2Cl_{10} and $Fe_2W_2Cl_{10}$

(Figure 11). It is obvious that the relatively open layer structure of FeW_2Cl_{10} adopts another Fe ion into its structure. The next exothermic effect corresponds with the formation a CdI_2-type related structure of $(Fe,W)_{1-x}Cl_2$, according to X-ray diffraction data. This structure can be envisioned by occupying the remaining octahedral void in the structure of $Fe_2W_2Cl_{10}$ (Figure 12) to yield $Fe_3W_2Cl_{10}$, but the precise cation ratio in this compound and the full characterisation of the crystal structure was not possible to obtain. Finally FeW_6Cl_{14} is formed, which has shown to crystallize with the $PbMo_6Cl_{14}$-type structure.[38]

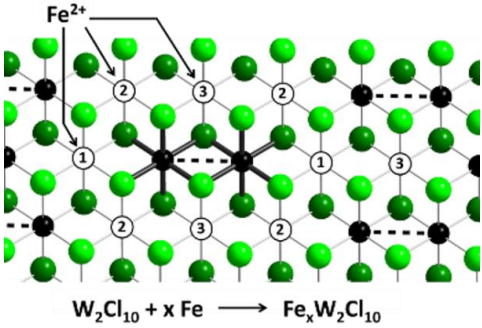

Figure 12. Section of one closed packed double layer made up by chloride ions (light green: in front, dark green: back) with (2/5) octahedral sites occupied with tungsten ions (black) forming $[W_2Cl_{10}]^{2n-}$ bioctahedra. More octahedral sites are occupied with iron ions, indicated with numbers for FeW_2Cl_{10} (1), $Fe_2W_2Cl_{10}$ (1+2). For $(Fe,W)_{1-x}Cl_2$ we assume a variable cation distribution pattern over all kinds of octahedral sites (1, 2, 3).

Synthesis

Reaction conditions based on DSC thermal effects were individually revised in order to obtain well-crystallized high yield products or single crystals. X-ray powder patterns of obtained compounds are shown in the Figure 13. Individually optimized reaction conditions are given as follows:

Fe_xWCl_6 was obtained as a black powder after heating β-WCl_6 with variable excess of iron powder with y = 0.1–19 fold molar proportions at 125 °C for 10 days (total mass: ca. 450 mg). Only a small fraction (x) of Fe was incorporated into the structure, while most of the employed elemental Fe (y) remained as a residue (z), explained in Equation (6). Fe_xWCl_6 has a phase width (x) as evidenced from the refinement of the unit cell parameters using powder XRD.

$WCl_6 + y\ Fe \rightarrow Fe_xWCl_6 + z\ Fe$ (6)

FeW_2Cl_{10} was obtained as green-black crystal plates after heating a mixture of β-WCl_6 with manganese powder in a 1:1 molar ratio at 270 °C for 100 h following Equation (7):

$2\ WCl_6 + 2\ Fe \rightarrow FeW_2Cl_{10} + 2\ FeCl_2$ (7)

$Fe_2W_2Cl_{10}$ was obtained as green-black crystal plates after heating a mixture of β-WCl_6 with iron powder at 300 °C for 100 h following Equation (8):

$6\ WCl_6 + 9\ Fe \rightarrow Fe_2W_2Cl_{10} + 2\ FeCl_2$ (8)

$(Fe,W)_{1-x}Cl_2$ was obtained as a dark-brown powder after heating a mixture of β-WCl_6 with iron powder at 350 °C for 48 h, following Equation (9):

$6\ WCl_6 + 9\ Fe \rightarrow 6\ (Fe,W)_{1-x}Cl_2 + 3\ FeCl_2$ (9)

FeW_6Cl_{14} was obtained as a brown powder after heating β-WCl_6 with iron powder in a 1:2 molar ratio at 475 °C for 24 h, following Equation (10):

$6\ WCl_6 + 12\ Fe \rightarrow FeW_6Cl_{14} + 11\ FeCl_2$ (10)

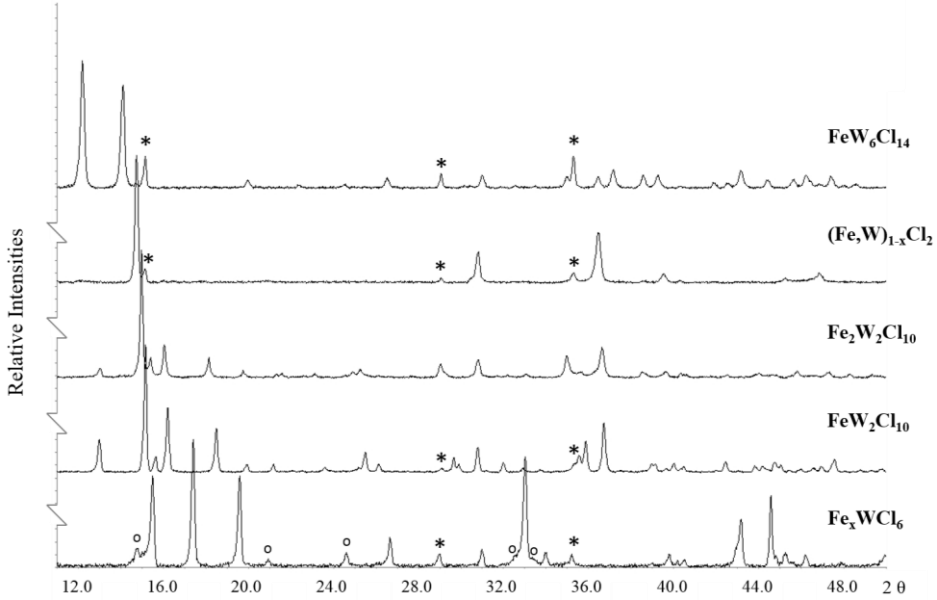

Figure 13. XRD patterns of compounds obtained during the reduction of WCl_6 with Fe. Two side phases are marked for $FeCl_2$ (∗) and $WOCl_4$ (o).

Characterization of Fe_xWCl_6

Two modifications have been reported for WCl_6. Rhombohedral (α-WCl_6) was prepared by Ketelaar and van Oosterhout by hydrogen reduction tungsten trioxide, followed by chlorination with gaseous Cl_2 at 600–700 °C.[1] A phase-change was first assigned at 228 °C[42] and later at ≤ 150 °C[3]. The crystal structure of trigonal β-WCl_6 was refined isotypic with the structure of UCl_6 and considered as high-temperature modification of WCl_6. However, this modification has shown to remain stable at room temperature, also in our reactions, e.g. when a commercial sample of α-WCl_6 was transformed into β-WCl_6 by sublimation. Both WCl_6 modifications are based on a hexagonal closest packing of chloride ions with different arrangements of tungsten ions, occupying (1/3) octahedral interstices in every second interlayer.

When β-WCl_6 is heated in the presence of iron powder it undergoes a phase transition to yield the α-WCl_6-type structure product, here described as Fe_xWCl_6. This transition is not obtained in the absence of metal powder. In order to investigate the role of iron powder, separate experiments were carried out in fused silica ampules. Fe_xWCl_6 revealed an increasing unit cell volume with increasing excess of metal powder. Reactions here reported were performed at 125 °C for ten days with an increasing amount of metal powder. These experiments revealed an expansion of the *c*-axis, related with an increase of the unit cell volume for Fe_xWCl_6 in the order of $\Delta V = 14$ Å^3, which is graphically displayed in Figure 14. The saturation of the metal uptake seems to emerge with a large excess of metal powder.

This leads to the assumption that a variable intercalation of iron powder into the structure of WCl_6 is possible, and thereby represents the first reduction step of the WCl_6 - Fe mixture. The upper concentration of iron metal ions in WCl_6 is estimated to be very small. According to an X-ray structure determination on a sublimation-grown single crystal of Fe_xWCl_6, the iron ions are occupying octahedral sites in layers that are occupied with (1/3) tungsten ions (Figure 15). The refined iron content in the crystal structure of Fe_xWCl_6 (space group R-3, a = 6.113(3) Å, c = 17.06(1) Å) was refined in the order of x = 0.1. The obtained unit cell volume (V = 552.0(5) Å^3) is clearly larger than values reported for α-WCl_6 (V = 543.3(1) Å^3 [36,43] or V = 534.9(1) Å^3 [2]. It can be addressed to the upper range of the iron uptake in Fe_xWCl_6 with respect to the data given in Table 4. An analytical refinement of the metal incorporation into the structure of WCl_6 remains difficult to date, due to the excess of iron powder used in reactions of Fe_xWCl_6.

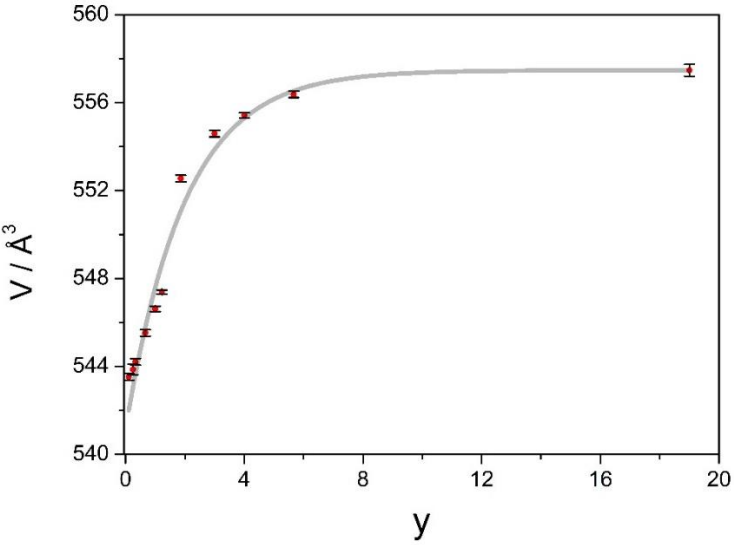

Figure 14. Unit cell volume of $W(Fe_x)Cl_6$ phases as a function of excess (y) iron powder.

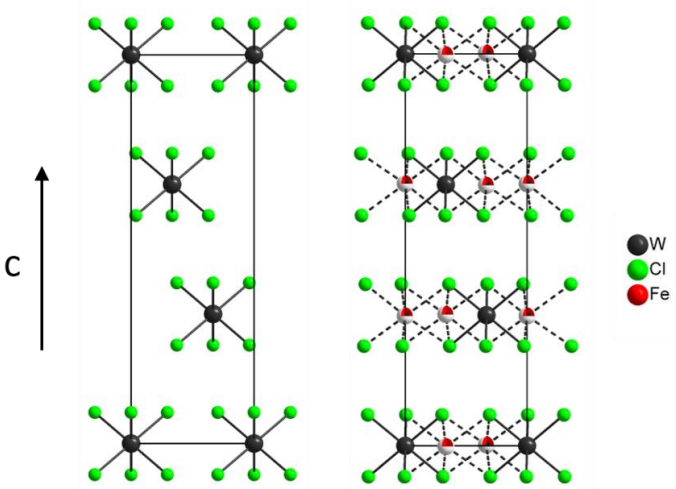

Figure 15. Crystal structures of α-WCl_6 (left) and Fe_xWCl_6 (right). Structures are based on closest packed layers of chloride ions stacked along the *c*-axe direction, and metal ions occupying octahedral sites in every second interlayer. Partially occupied sites of iron ions are shown in Fe_xWCl_6.

Table 4. Selected single crystal structure refinement data of $Fe_{0.08}WCl_6$ and FeW_2Cl_{10}.

	$Fe_{0.08}WCl_6$	FeW_2Cl_{10}
Formula weight	401.02	778.05
Temperature / ° K	293(2)	293(2)
Crystal system	trigonal	monoclinic
Space group	*R-3m*	*C2/c*
Unit cell dimensions	*a* = 611.3(3) Å *c* = 1706(1) Å	*a* = 6.113(3) Å *c* = 17.06(1) Å β = 109.035(4) °
Volume / Å^3	552.0(5)	1200.7(1)
Z	3	4
Density (calculated) / g/cm^3	3.619	4.304
Absorption coefficient / mm^{-1}	17.906	22.477
F(000)	534	1376
Crystal size / mm^3	0.24 x 0.20 x 0.12	0.03 x 0.03 x 0.01
Independent reflections	236 ($R_{(int)}$ = 0.0718)	1056 (R(int) = 0.0307)
Goodness-of-fit on F^2	1.176	1.121
Final R indices [I > 2σ(I)]	R1 = 0.0213, wR2 = 0.0458	R1 = 0.0366, wR2 = 0.0814
R indices (all data)	R1 = 0.0213, wR2 = 0.0458	R1 = 0.0391, wR2 = 0.0832
Largest diff. peak and hole / e·Å^{-3}	1.111 and -0.930	3.304 and -1.003

Characterization of FeW_2Cl_{10}

FeW_2Cl_{10} is observed as a second exothermic signal in DSC and crystalizes monocline as black powders or crystals in the space group *C2/c*. The crystal structure has been reported on basis of powder XRD data refinement[33] and additionally single-crystal data presented in Table 4, both of them with a very high similarity in lattice parameters.

The structures of FeW_2Cl_{10} is isotypic to MW_2Cl_{10} (*M* = Mn, Co) and is represented by a hexagonal close packing of chloride atoms with alternating layers along the *c*-axis direction. Iron and tungsten atoms occupy 3/5 of octahedral interstices in every second interlayer of the structure. An alternative formula can be given as a $Fe_{1/5}W_{2/5}Cl_2$. The structural arrangement of a Cl-($Fe_{1/5}W_{2/5}$)-Cl sandwich in the structure is shown on the Figure 16 (left, on top), and one of the layers turned of 90 ° in a *b*-axe direction, is presented below.

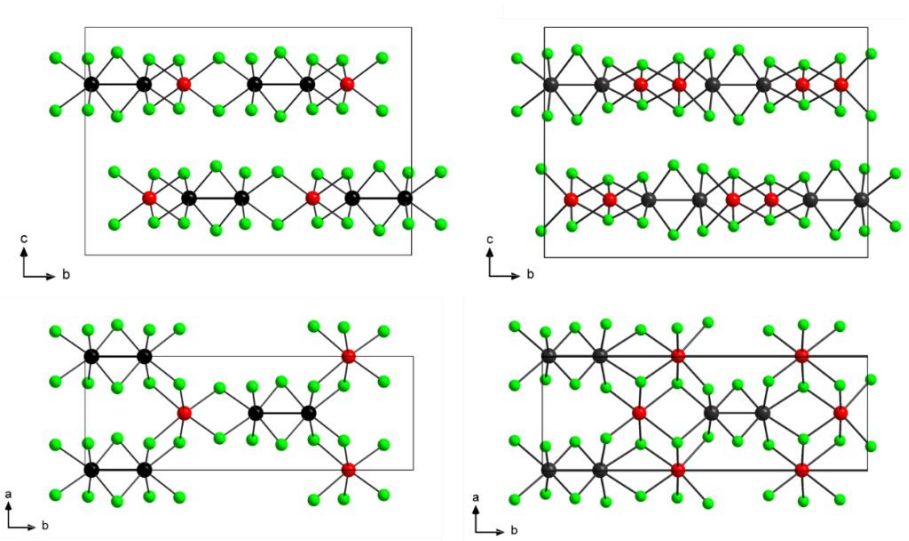

Figure 16. Crystal structures of FeW_2Cl_{10} (left) and $Fe_2W_2Cl_{10}$ (right). The top projections represent two layers, and the bottom projections display one layer, rotated by 90° around the (horizontal) b-axis. Chloride ions are shown in green, tungsten ions black, and iron ions red.

FeW_2Cl_{10} is made up from bioctahedral $[W_2Cl_{10}]$ units, where iron atoms are placed in octahedral voids in between them in every layer, and connected with six chloride atoms from $[W_2Cl_{10}]$ unit. The bioctahedra unit $[W_2Cl_{10}]$ in FeW_2Cl_{10} is well-known from the structure of WCl_5[4] and is build up from two $[WCl_6]$ edge shearing octahedra.

However, tungsten atoms in the $[W_2Cl_{10}]$ dimer of WCl_5 are placed away from each other, which leads to the long distance between tungsten atoms d_{w-w} = 3.814(2) Å, and thereby exclude bonding between them.

The bioctahedra motive in the crystal structures of FeW_2Cl_{10} behaves in the opposite way, so that tungsten atoms in $[W_2Cl_{10}]$ are shifted towards each other, thereby allowing the presence of a W–W bond. The W–W distances in FeW_2Cl_{10} are close to the interatomic distance in WCl_4 (d_{w-w} = 2.688(2) Å[5] and d_{w-w} = 2.713(3) Å[6]). Another example of an edge-sharing bioctahedral $[W_2Cl_{10}]^{2-}$ arrangement similar to the one in FeW_2Cl_{10} was reported for $(NR_4)_2W_2Cl_{10}$ having a bond length between tungsten atoms equal d_{w-w} = 2.792(1) Å[44].

The compound behaves stable in air but not against water. FeW_2Cl_{10} can be washed with dry ethanol under argon atmosphere, and forms deep green single-crystals of $W_2Cl_4(OEt)_4(EtOH)_2$[45] and after some time deep red single-crystals of $W_2Cl_4(OEt)_6$[46], shown in Figure 17. Bioctahedral $[W_2Cl_4L_6]$ units in both structures contain four terminal chloride ligands. W–W distances were reported in accord to a formal double bond for the W^{4+} species with d_{W-W} = 2.483 Å, and a formal single bond for the W^{5+} species with d_{W-W} = 2.715 Å. The bond lengths and bonding conditions in these compounds appear different to the (μ_2-)chloride bridged bioctahedra in compounds, in which quantum chemical calculation have been performed for $[W_2Cl_{10}]^{n-}$ (n = -2, -4), described later.

Figure 17. Green crystals of $W_2Cl_4(OEt)_4$ $(EtOH)_2$, and red crystals of $W_2Cl_4(OEt)_6$ from reactions of FeW_2Cl_{10} with ethanol.

Characterization of $Fe_2W_2Cl_{10}$

Powders of $Fe_2W_2Cl_{10}$ behave stable in air but not against water. The crystal structure of $Fe_2W_2Cl_{10}$, as refined from X-ray powder data (Figure 16, right), is closely related to the structure of FeW_2Cl_{10} (Figure 16, left). Both structures are composed of a distorted hexagonal closest packed arrangement of chloride ions alternating along the *c*-axis direction (Figure 16, top).

Metal atoms occupy octahedral interstices in every second interlayer at z = 1/4 and 3/4. One-fifth of octahedral positions are occupied by pairs of tungsten atoms which are moved toward each other to yield short interatomic distances which can be interpreted as bonding W−W interactions. Interatomic distances ($d_{W–W}$ = 2.637(1) Å) calculated for $Fe_2W_2Cl_{10}$ are clearly shorter than the corresponding ($d_{W–W}$ = 2.707(5) Å) distances reported for FeW_2Cl_{10}. The motif of an edge-sharing $[W_2Cl_{10}]$ double octahedron contained in these structures corresponds to a section of the WCl_4 structure, having a separation of tungsten atoms $d_{W–W}$ = 2.688(2) Å[5] and 2.713(3) Å[6], as reported from two different sources. Thus, W−W distances around 2.7 Å obtained for FeW_2Cl_{10} and WCl_4 may be typically addressed with an oxidation state of +4 for tungsten. The corresponding distance in $Fe_2W_2Cl_{10}$ appears shorter and should be addressed to a lower oxidation state (formally +3) of tungsten.

Two iron ions per formula unit $Fe_2W_2Cl_{10}$ occupy another one-fifth of octahedral sites. Metal−halide distances range at $d_{W–Cl}$ = 2.388(2)−2.560(2) Å ($\bar{d}_{W–Cl}$ = 2.471(2) Å) and $d_{Fe–Cl}$ = 2.284(3)−2.536(3) Å. The average Fe−Cl distance $\bar{d}_{Fe–Cl}$ = 2.440(3) Å in the structure of $Fe_2W_2Cl_{10}$ is in-between the corresponding average distances obtained in $FeCl_2$ ($\bar{d}_{Fe–Cl}$ = 2.500(5) Å)[47] and $FeCl_3$ ($\bar{d}_{Fe–Cl}$ = 2.377(5) Å)[48].

Characterization of $(Fe,W)_{1–x}Cl_2$

The phase which we describe here as $(Fe,W)_{1–x}Cl_2$ appears as a dark-green, almost black powder. The X-ray powder pattern can be indexed isotypically to the crystal structure of $FeCl_2$. Until now, it is not known if this phase exhibits a cation deficiency. Calculated lattice parameters obtained from samples, prepared with different amounts of iron powder, (at 350 °C, 5 h) indicate the existence of a phase width. Lattice parameters calculated for $(Fe,W)_{1–x}Cl_2$ revealed a shorter a-axis and a longer c-axis compared to $FeCl_2$ (V = 197.15(1) Å)[47] and a smaller unit cell volume of $(Fe,W)Cl_2$ (V = 180.23(4) Å)[36].

The strongest (003) X-ray reflection of the $FeCl_2$ side phase, indicated as (∗) in Figure 13, appears as a small peak right next to the corresponding strongest reflection of $(Fe,W)Cl_2$. A comparison of average Fe−Cl and W−Cl distances (2.440(3) and 2.471(2) Å) suggest quite similar radii for Fe and W ions in $Fe_2W_2Cl_{10}$. It is clear that more studies will be necessary to identify the composition and phase range of this structure.

The compound originally described as $(Fe,W)Cl_2$ was assigned with a defect $FeCl_2$ ($CdCl_2$-type) structure. If iron was in divalent and tungsten in trivalent oxidation state, the corresponding charge balanced phase would be best described as $Fe_{1-x}W_{2/3x}Cl_2$. Carefully recorded powder XRD patterns support the assumption of a defect $CdCl_2$-type structure. XRD studies of $(Fe,W)_{1-x}Cl_2$ samples prepared under different conditions (with respect to reaction time and excess of iron powder) have revealed small but significantly deviating lattice parameters indicating a phase-width. The observation of some extra reflections in the powder XRD pattern suggests the presence of a super structure.

EDX measurements revealed the composition $(Fe_{0.37}W_{0.38})Cl_2$ which is close to $Fe_2W_2Cl_{10}$. FeW_6Cl_{14} was used as a standard. Additional picture of $(Fe,W)_{1-x}Cl_2$ was made with an HITACHI SU8030 (Figure 18). Hence, a cation deficiency is clearly indicated with respect to a $CdCl_2$-type structure.

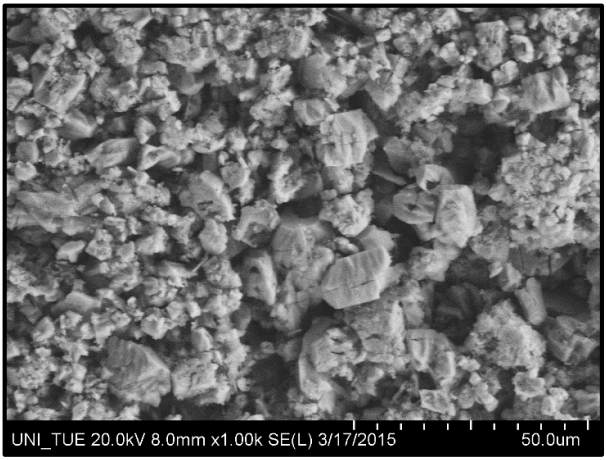

Figure 18. Picture of $(Fe,W)_{1-x}Cl_2$ crystallites made with an Electron Scanning Microscope HITACHI SU8030.

Characterization of FeW_6Cl_{14}

The last exothermic effect at around 450 °C, in the DSC diagram, represents the last reduction step of tungsten hexachloride with iron powder. FeW_6Cl_{14} crystallizes cubically in the space group *Pn-3*, isotypic to the MW_6Cl_{14} (*M* = Mn, Co, Ni) compounds (Figure 19). The structure contains $[(W_6Cl_8i)Cl_6a]^{2-}$ clusters and Fe^{2+} cations placed in octahedral voids. The arrangement of divalent iron atoms and $[W_6Cl_{14}]^{2-}$ ions follows the atom arrangement in the NaCl-type structure. The iron ion in this structures is coordinated in a distorted octahedron (d_{Fe-Cl} = 2.47(2) Å; Cl–Fe–Cl angle: 83.3(4)–96.7(4) °) formed by outer chlorido ligands of the $[(W_6Cl_8i)Cl_6a]^{2-}$ cluster.

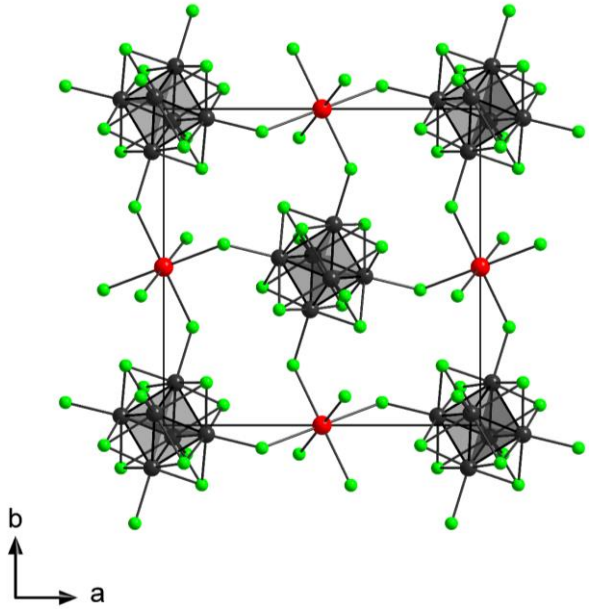

Figure 19. Crystal structure of FeW_6Cl_{14}.

Magnetic Measurement

Crystalline samples of compounds were loaded into gelatine capsules under argon atmosphere (glovebox) and their magnetic susceptibilities were recorded with a SQUID magnetometer (superconducting quantum interference device, Quantum Design, MPMS) with a magnetic field of 100 Oe, in the temperature range 5 K ≤ T ≤ 300 K with progressive steps (the higher the temperature the bigger steps between collected data points). The susceptibility of FeW_6Cl_{14} was fitted following an extended Curie-Weiss law ($\chi = C / (T - \theta) + \chi_0$).

The magnetic properties of $FeCl_2$ deserve special precaution because $FeCl_2$ is obtained as a side-phase in essentially all reactions. Moreover, the crystal structure of $FeCl_2$ ($CdCl_2$-type) is closely related to the layered structures described herein. The magnetic structure of $FeCl_2$ is composed of hexagonal closest packed layers of ferromagnetically aligned Fe^{2+} spins with a strong anisotropy confining the spins parallel to the hexagonal axis. Alternating layers in this structure are coupled weakly antiferromagnetically to each other so that the overall magnetic structure is antiferromagnetic below $T_N = 23.55$ K.[49]

Magnetic susceptibility measurements performed for FeW_2Cl_{10}, $(Fe,W)_{1-x}Cl_2$, and FeW_6Cl_{14} are shown in Figure 20. Measurements on WCl_4 and $FeCl_2$ are used as references. The measurement on WCl_4 shows temperature independent paramagnetic (T, P) behavior consistent with the consideration of W^{4+} ions and electrons being semi-localized in formally double bonded W–W dumbbells. In comparison, the formula FeW_2Cl_{10} can be decomposed into $FeCl_2$ and two times WCl_4, yielding four unpaired electrons from one (high spin d^6) Fe^{2+} ion per formula unit, responsible for paramagnetic behavior. An antiferromagnetic ordering obtained in the plots of FeW_2Cl_{10} and $(Fe,W)_{1-x}Cl_2$ at 24 K can be addressed to the presence of the $FeCl_2$ side-phase.

Paramagnetic behavior is found for FeW_6Cl_{14}. The fit with an extended Curie-Weiss law corresponds to the expected value of 5.3 μ_B, consistent with one Fe^{2+} and a diamagnetic $[W_6Cl_{14}]^{2-}$ cluster.

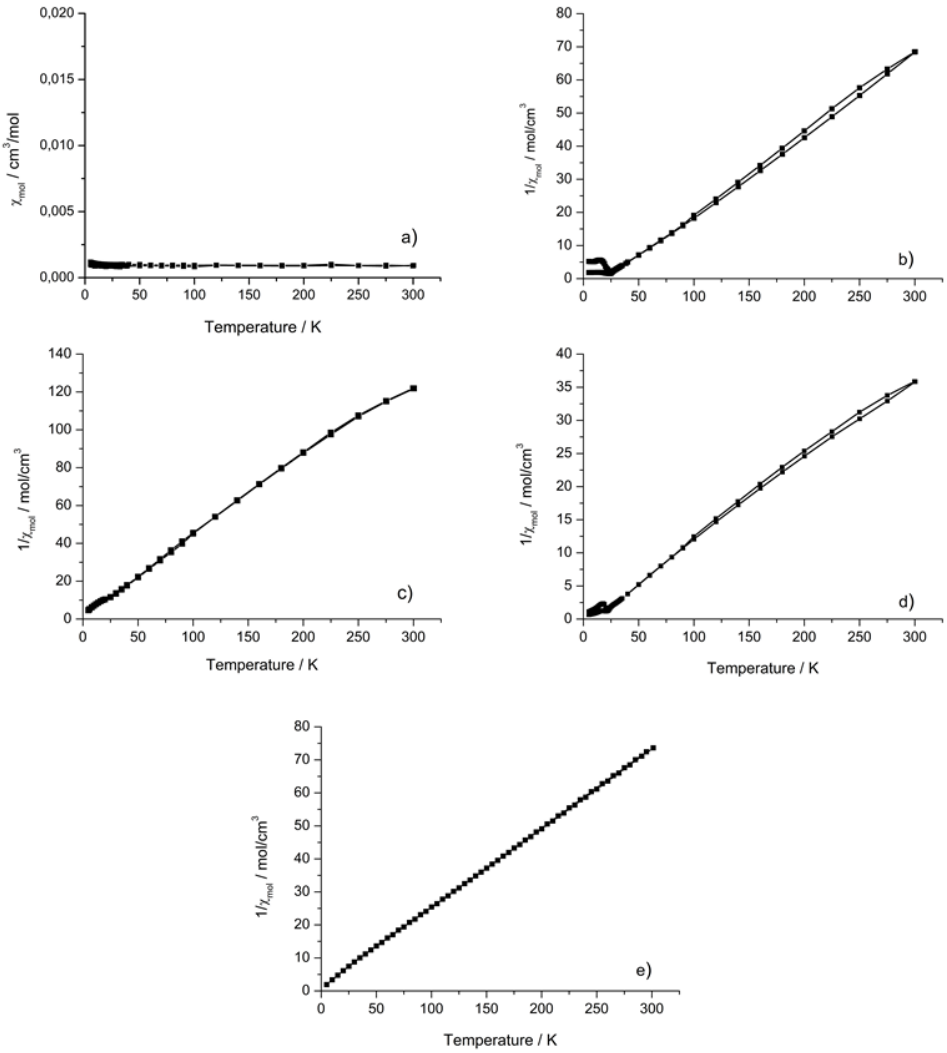

Figure 20. Temperature dependency of the magnetic susceptibilities of a) WCl_4, b) $FeCl_2$, c) $(Fe,W)_{1-x}Cl_2$, d) FeW_2Cl_{10} and e) FeW_6Cl_{14} measured in field cooled (FC) and zero field cooled (ZFC) mode.

Mössbauer Spektroskopie

^{57}Fe Mössbauer spectroscopic measurements were performed in transmission mode at room temperature using a constant acceleration spectrometer with a ^{57}Co(Rh) source. Isomer shifts are given relative to that of α-Fe at room temperature. Measurements were done for Fe_xWCl_6, FeW_2Cl_{10}, $Fe_2W_2Cl_{10}$, and $(Fe,W)_{1-x}Cl_2$. $FeCl_2$ was used as a reference, appearing with the $CdCl_2$ and CdI_2 structure (high pressure modification) in approximate 1:2 ratio (estimated form the XRD pattern).

The ^{57}Fe Mössbauer spectra of the different samples and the corresponding fitting parameters are displayed in Figure 21 for Fe_xWCl_6, FeW_2Cl_{10}, $Fe_2W_2Cl_{10}$, $(Fe,W)_{1-x}Cl_2$. A mixture of $CdCl_2$-type[47] and CdI_2-type[50] $FeCl_2$ is used as a reference.

The recorded spectra consist of multiple contributions in each case. The presence of metallic Fe shown by the black line with its characteristic (sextet) splitting and position is evident for samples Fe_xWCl_6, FeW_2Cl_{10} and $Fe_2W_2Cl_{10}$ as a result of the syntheses in which iron powder was employed. Since the value of the density of elemental Fe is high in metallic iron in comparison to the chloride phases, this sextet appears to be very pronounced (see area fraction in Table 5), but the mass fraction of metallic Fe is correspondingly smaller. The other contributions in the spectra are represented exclusively by doublets with isomer shifts in the range from 1.0 to 1.2 mm/s which is characteristic of Fe^{2+} in high-spin state.[51] Therefore, the presence of Fe^{3+} can be excluded for all samples. The presence of multiple Fe^{2+} doublets reveals different Fe environments, either in the same crystal structure or in different phases.

The disordered situation of Fe^{2+} ions in the structure of Fe_xWCl_6, as refined from a previous single-crystal study corresponds with a broad doublet. FeW_2Cl_{10} contains one, and $Fe_2W_2Cl_{10}$ contains two major doublets, which appear in line with the number of crystallographically distinct Fe^{2+} ions in the respective structure, as also represented by the occupation of positions 1 and 2 in Figure 12.

The Mössbauer spectrum of $(Fe,W)_{1-x}Cl_2$ shows essentially one (yellow) doublet and a much smaller (red) one. The smaller (red) one can be addressed as a $FeCl_2$ side phase, indicated by comparison with the (red) $FeCl_2$ reference ($CdCl_2$-type). The presence of just one doublet suggests the presence of only one Fe^{2+} species in the structure of $(Fe,W)_{1-x}Cl_2$. Not unexpectedly the Mössbauer pattern, and thus the environment of this iron ion appears similar to that of iron ions in FeW_2Cl_{10} and $Fe_2W_2Cl_{10}$.

As can be seen in the Mössbauer spectrum of $(Fe,W)_{1-x}Cl_2$ a considerable amount of Fe powder is contained, due to the excess of iron powder used in the reaction. This issue appears to be a problem for the magnetic measurement of this compound.

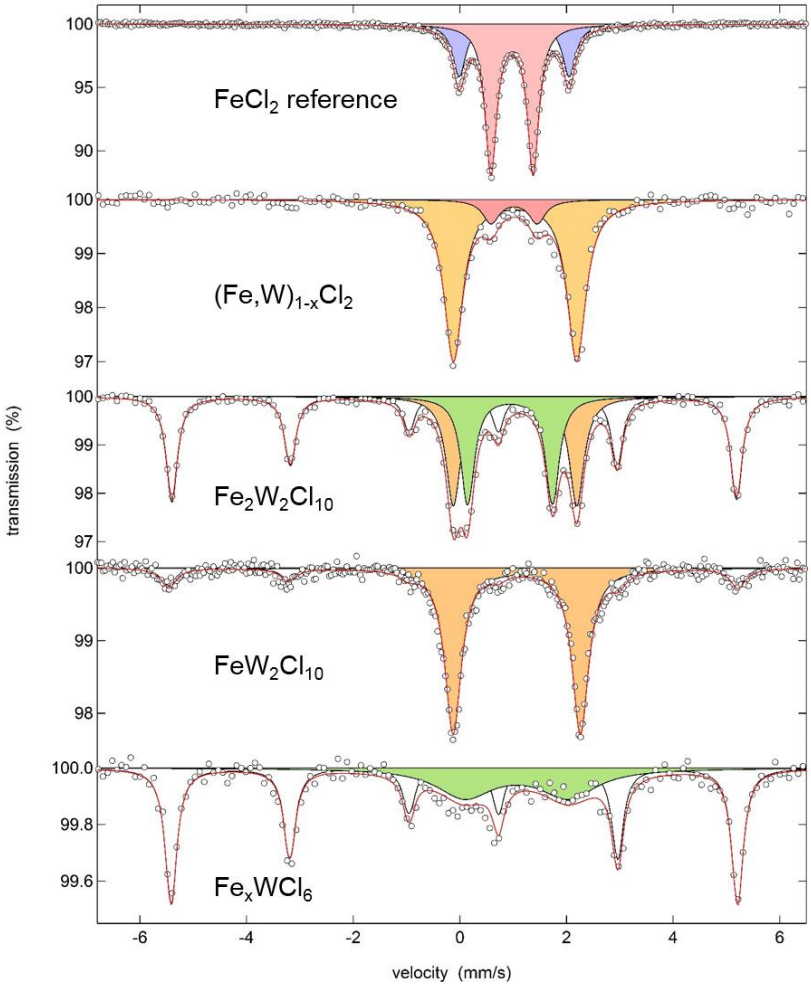

Figure 21. ^{57}Fe Mössbauer spectra including fit (red line). The $FeCl_2$ reference is represented by a mixture of the $CdCl_2$ (red fit) and a CdI_2 structured phase (blue fit). Fe^{2+} species present in ternary Fe-W-Cl compounds is fitted (yellow and green). The presence of the iron impurity is represented by the characteristic sextet splitting, detectable in the spectra of $Fe_2W_2Cl_{10}$, FeW_2Cl_{10} and in Fe_xWCl_6.

Table 5. Isomer shifts IS, quadrupole splitting QS, hyperfine fields B_{hf}, and line widths used to fit the Mössbauer spectra.

sample		IS (mm/s)	QS (mm/s)	B_{hf} (T)	line width (mm/s)	area fraction
$FeCl_2$	Fe^{2+}	1.085 ± 0.001	0.790 ± 0.001	-	0.263 ± 0.001	68.5 %
	Fe^{2+}	1.125 ± 0.001	2.062 ± 0.003	-	0.299 ± 0.004	31.5 %
$(Fe,W)_{1-x}Cl_2$	Fe^{2+}	1.141 ± 0.002	2.310 ± 0.005	-	0.427 ± 0.008	88.8 %
	Fe^{2+}	1.124 ± 0.016	0.865 ± 0.031	-	0.373 ± 0.048	11.2 %
$Fe_2W_2Cl_{10}$	Fe^{2+}	1.141 ± 0.005	2.315 ± 0.006	-	0.330 ± 0.009	30.8 %
	Fe^{2+}	1.048 ± 0.003	1.589 ± 0.007	-	0.307 ± 0.010	26.4 %
	Fe^{0}	-0.005 ± 0.002	0.009 ± 0.004	32.8 ± 0.1	0.255 ± 0.007	42.8 %
FeW_2Cl_{10}	Fe^{2+}	1.174 ± 0.002	2.388 ± 0.004	-	0.374 ± 0.006	81.8 %
	Fe^{0}	-0.016 ± 0.013	0.001 ± 0.027	33.1 ± 0.1	0.349 ± 0.040	18.2 %
Fe_xWCl_6	Fe^{2+}	1.172 ± 0.036	1.950 ± 0.062	-	1.274 ± 0.101	35.7 %
	Fe^{0}	-0.004 ± 0.003	0.011 ± 0.006	32.9 ± 0.1	0.263 ± 0.008	64.2 %

Quantum Chemical Calculations

The crystal structures of FeW_2Cl_{10} and $Fe_2W_2Cl_{10}$ compromise edge-sharing $[W_2Cl_{10}]^{n-}$ bioctahedra, which can be derived from the structure of tungsten pentachloride. The crystal structure of WCl_5 contains two independent, but only slightly distinct W_2Cl_{10} molecules having W–W distances of 3.816(2) and 3.813(1) Å.[4]

The short W-W bond distance is of particular interest for these substances. Investigations of this approach were done with use of quantum chemical calculations using $[W_2Cl_{10}]^{n-}$ clusters as model system. Hereby we assume that the electronic structure and in particular the bond distances are only marginally influenced by surrounding of the clusters. This assumption is motivated by the much longer bond distances for Fe-W (3.59-3.72 Å), Fe-Fe (3.71 Å) and Fe-Cl (2.28-2.64 Å) as compared to the W–W (2.64/2.70 Å) and W–Cl (2.29-2.49 Å). Bonding and antibonding interactions between the three t_{2g} d-orbitals in the bioctahedral $[W_2Cl_{10}]^{n-}$ ion are

expected to lead to a MO scheme following the order of $\sigma < \pi < \delta < \delta^* < \pi^* < \sigma^*$ levels with increasing energy (Figure 22). The occupation of these levels from d^1-d^1 to d^6-d^6 configurations involve various electronic situations of which the d^6-d^6 configuration would represent the absence of metal–metal bonding.[52,53]

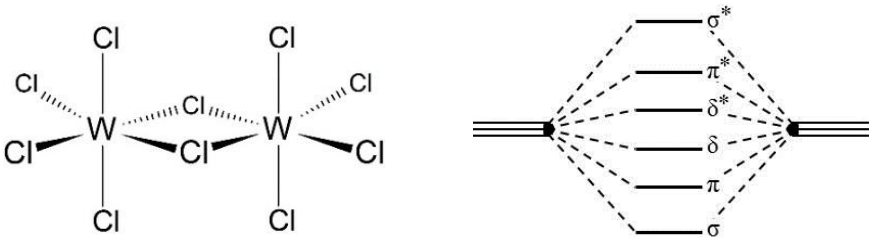

Figure 22. Structure of a bioctahedral $[W_2Cl_{10}]^{n-}$ fragment (left) and energy splitting of t_{2g} type levels for the occupation of bonding and antibonding W–W states (right).

A deviation from the above mentioned energy level order has to be considered in the present case. Calculations find that the δ level is destabilized through interactions with (μ_2)-bridging halides (orbitals) of the same symmetry (Figure 22).[54,55,56,57,58,59] Thereby the δ level is moved slightly above the δ* level. The electronic configuration of the ground state has been assigned to $\sigma^2\pi^2\delta^{*2}$ by an analysis of the apparent metal-metal distance.[60] However, calculations and the near degeneracy of the δ and δ* orbitals support antiferromagnetic ordering within bioctahedral tungsten clusters for d^3-d^3 situations with a ground state composed of about 50% each of $\sigma^2\pi^2\delta^{*2}$ and $\sigma^2\pi^2\delta^2$ configurations. This is equivalent to the occupation pattern $\sigma^2\pi^2\delta^{*1}\delta^1$ for $Fe_2W_2Cl_{10}$. According to McGardy et al[57] the inversion of the δ and δ^* levels is lifted only if the metal–metal distance becomes shorter than 2.3 Å. A W–W triple bond and a sequence of energy levels corresponding to the molecular orbitals shown in Figure 23 is expected.

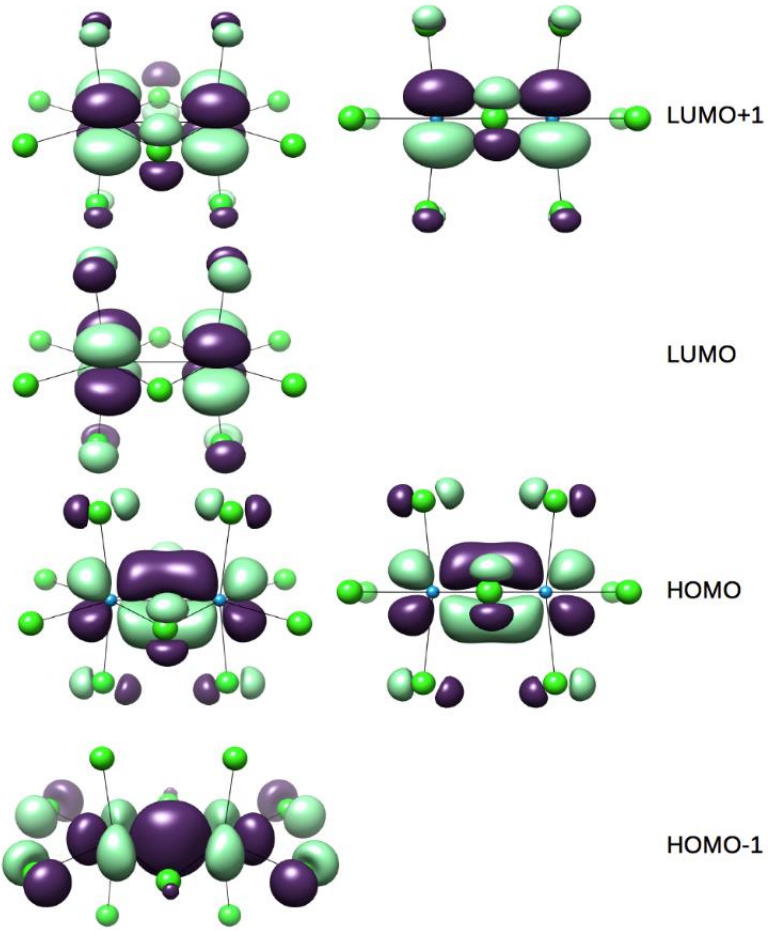

Figure 23. Molecular orbitals of the $[W_2Cl_{10}]^{2-}$ anion representing the σ (HOMO-1) and π (HOMO) molecular orbitals, as well as the energy inversion of the δ (LUMO) and δ* (LUMO+1) levels as a result of the particular linear combination of the d-type orbitals with the p-orbitals of bridging chloride ions. Orbitals at right are rotated to highlight the π-type bonding (below) and the antibonding situation between δ-type molecular orbitals and the p-orbitals of bridging chloride ions. All molecular orbitals have been rendered[61] with an iso value of 0.045.

FeW_2Cl_{10} contains the $[W_2Cl_{10}]^{2-}$ ion which can be related to the diamagnetic WCl_4 with a d^2-d^2 interaction formally consistent with a ($\sigma^2\pi^2$) double bond. W–W distances at d_{W-W} = 2.707(5) Å for FeW_2Cl_{10} are in line with our calculated value (d_{W-W} = 2.719 Å) as well as crystal structure values reported for WCl_4 (d_{W-W} = 2.688(2) Å[5] or 2.713(3) Å)[6], and $(NR_4)_2(W_2Cl_{10})$ (d_{W-W} = 2.792(1) Å)[44]. The results of our calculations on bioctahedral $[W_2Cl_{10}]^{2-}$ ions are represented by the molecular orbitals shown in Figure 23. The HOMO-1 represents the σ-type bond, and the HOMO represents a π-type bond for the W–W dumbbell of W^{4+} ions in $[W_2Cl_{10}]^{2-}$. For this cluster, but also for the d^3 analog on $[W_2Cl_{10}]^{4-}$ and in line with former quantum chemical results an inversion of δ/δ* type levels is found.

The situation of $[W_2Cl_{10}]^{4-}$ in $Fe_2W_2Cl_{10}$ with a d^3-d^3 interaction appears more complicated due to occupation of δ and δ* levels. The W–W distance of d_{W-W} = 2.637(1) Å in $Fe_2W_2Cl_{10}$ is well reproduced with our calculations which provide d_{W-W} = 2.644 Å. It is expected that the W(d^3) –W(d^3) bond distance with an effective orbital occupation of $\sigma^2\pi^2\delta^{*1}\delta^1$ is similar to the distance between the W(d^2) –W(d^2) centers with the configuration $\sigma^2\pi^2$ as both cases correspond to a formal double bond. We note that an occupation of the bonding δ and antibonding δ* orbitals with a preference for the occupation of the latter orbital in $[W_2Cl_{10}]^{4-}$ is expected to lead to a weaker bonding than in $[W_2Cl_{10}]^{2-}$. Thus, this effect should be small as δ bonding and antibonding is relatively weak.

We considered two possible explanations for the increased bond strength of the W(d^3) –W(d^3) cluster as compared with the W(d^2)-W(d^2) one: occupation of the δ orbitals increases the number of electrons at the tungsten atoms and thus lowers the electronegativity of this center. Thus, the tungsten d-orbitals become more diffuse which leads to a stronger σ- and π-bonding. This argument is supported by the Mayer bond order[62] of these complexes which was found to be 1.39 for $[W_2Cl_{10}]^{2-}$ and 1.62 for $[W_2Cl_{10}]^{4-}$. An alternative explanation for the observed bond distance difference is that the effective (positive) charge at the tungsten atoms decreases with the reduction of $[W_2Cl_{10}]^{2-}$ to $[W_2Cl_{10}]^{4-}$. Indeed natural population analysis (NPA)[63] indicates a slightly smaller charge of the W atoms in $[W_2Cl_{10}]^{4-}$ (0.510 e) than in $[W_2Cl_{10}]^{2-}$ (0.541 e). Thus, a smaller Coulomb repulsion between the tungsten centers is another possible explanation for the observed bond distance differences. The small absolute change of the NPA charges and the rather significant difference between the Mayer bond orders indicate that the latter may be more important for the observed bond distance changes.

4.3. Co-W-Cl System

Thermal Analysis of Co-W-Cl System

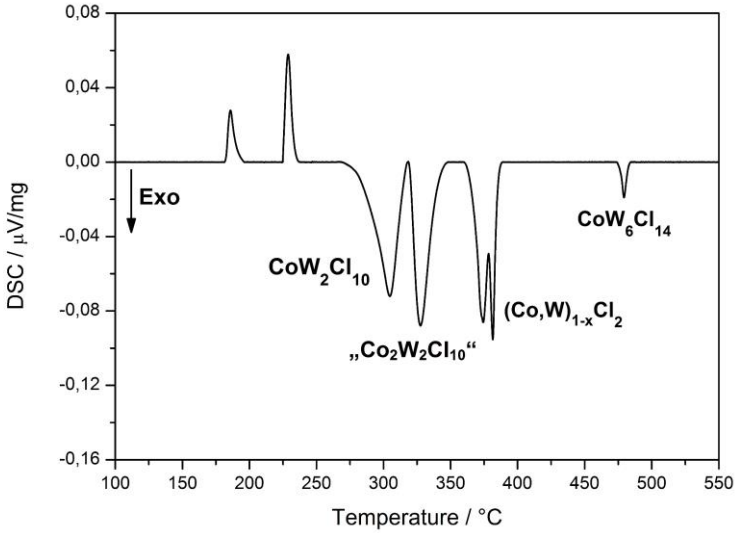

Figure 24. Thermal effects during the reduction of WCl_6 with cobalt powder with increasing temperature (corrected for background).

The third metal applied for the reduction of tungsten hexachloride is cobalt. A 1:2 molar mixture of β-WCl_6 and cobalt powder was mixed in an agate mortar and ca. 60 mg were enclosed into a gold plated container and heated with a heating rate of 2 °C/min between room temperature and 550 °C. These studies are designed to systematically detect and to investigate compounds which appear during the successive reduction of tungsten hexachloride. The differential scanning calorimetry (DSC) investigation is performed with a (WCl_6/Co) sample enclosed into an air-tight steel container with the recorded thermogram shown in Figure 24.

DSC experiments and separate preparations in silica tubes are performed under essentially similar conditions. Some explorative adjustments of preparation conditions in silica tubes were done. This involves the employment of lower reaction temperatures and prolonged reaction durations in attempt to improve the yield and crystallinity of products. Reaction products are characterized by X-ray powder diffraction (Figure 25).

The reduction of WCl_6 is performed with an appropriate amount of cobalt powder, allowing for the reduction of tungsten to the oxidation state +2, consistent with W_6Cl_{12}. As it turned out in the present reaction, the final product of the reaction (11) is CoW_6Cl_{14}.

$$6\ WCl_6 + 12\ Co \rightarrow CoW_6Cl_{14} + 11\ CoCl_2 \qquad (11)$$

The DSC measurement shows several thermal effects (Figure 24). The first endothermic effect corresponds to the sublimation temperature of β-WCl_6. The following endothermic effect represents the formation of a melt, as has been confirmed by visual inspection of a sample heated in a silica tube. The same pattern has been confirmed by a separate study in which only β-WCl_6 was employed. The similar behave was observed for iron and nickel system.

An inspection of the initial reaction of β-WCl_6 with cobalt powder revealed a transformation of β-WCl_6 into a rhombohedral α-WCl_6-type structure. This material can be, however, considered as a cobalt-intercalated tungsten hexachloride structure having the general composition Co_xWCl_6, as is discussed later. The missing DSC signal for Co_xWCl_6 can be explained with the really slow incorporation of cobalt powder into WCl_6, as has been shown during reactions in silica tubes.

Following this highly reactive stage a cascade of exothermic effects is followed. The next two exothermic effects displayed in the DSC are centered slightly above 300 and 325 °C can be explained with the formation of two compounds CoW_2Cl_{10} and "$Co_2W_2Cl_{10}$" crystalizing monoclinically.

Two following exothermic effects centered near 380 °C cannot be addressed separately. A compound resulting from these events is characterized as a $CdCl_2$-type structure, which can be described as $(Co,W)_{1-x}Cl_2$. The final occasion recorded in the DSC represents the exothermic formation of CoW_6Cl_{14} centered near 480 °C which crystallizes isotypic to MW_6Cl_{14} (M = Mn, Fe, Ni).

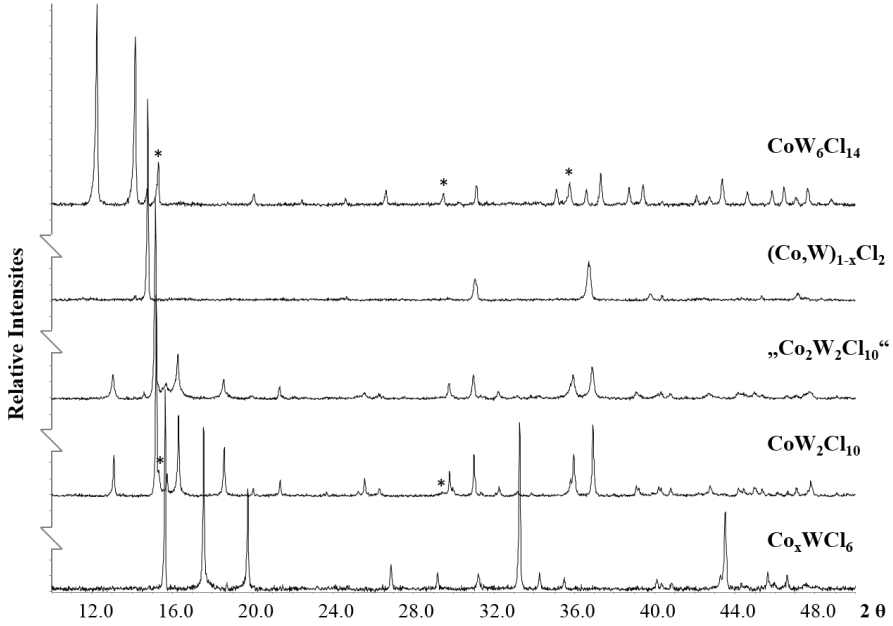

Figure 25. X-ray powder patterns of compounds obtained in the Co-W-Cl system with increasing preparation temperature (from bottom to top). $CoCl_2$ is marked (*) as a side-phase.

Synthesis

Compounds were initially prepared under conditions following the results of the DSC measurement. However the obtained products often showed low crystallinities. In such cases, reactions with prolonged heating durations were performed in silica tubes at lower temperatures. Total masses of 450 mg were employed for preparations of Co_xWCl_6 phases, and 150 mg for all other reactions:

Co_xWCl_6 was obtained as a black powder after heating β-WCl_6 with excess of cobalt powder (y = 0 – 10) at 145 °C for ten days, following reaction (12).

$$WCl_6 + y\ Co \rightarrow Co_xWCl_6 + z\ Co \qquad (12)$$

CoW_2Cl_{10} was obtained as a black powder after heating equimolar amounts of WCl_6 and cobalt powder at 220 °C for two days, following reaction (13).

$$2\ WCl_6 + 2\ Co \rightarrow CoW_2Cl_{10} + CoCl_2 \qquad (13)$$

"**$Co_2W_2Cl_{10}$**" was obtained as a black powder after heating WCl_6 and cobalt powder 2:3 molar ratio at 285 °C for two days, following reaction (14).

$$6\ WCl_6 + 9\ Co \rightarrow 3\ Co_2W_2Cl_{10} + 3\ CoCl_2 \quad (14)$$

$(Co,W)_{1-x}Cl_2$ was obtained as a brown powder after heating WCl_6 and cobalt powder 1:2 molar ratio at 400 °C for two days, following reaction (15).

$$6\ WCl_6 + 12\ Co \rightarrow 6\ (Co,W)_{1-x}Cl_2 + 6\ CoCl_2 \quad (15)$$

$(Co,W)_{1-x}Cl_2$ was obtained as single-phase material after the reaction product of reaction (4) was washed with ethanol to remove coproduced $CoCl_2$.

CoW_6Cl_{14} was obtained as a black powder after heating WCl_6 and cobalt powder in 1:2 molar ratio at 500 °C for two hours, following reaction (16).

$$6\ WCl_6 + 12\ Co \rightarrow CoW_6Cl_{14} + 11\ CoCl_2 \quad (16)$$

Characterization of Co_xWCl_6

Two modifications have been reported for WCl_6. Rhombohedral α-WCl_6 and trigonal β-WCl_6. Transformation from low temperature modification to high temperature modification was performed under argon atmosphere in a glass ampule at around 180 °C First after applying metal powder into the reaction with β-WCl_6, tungsten hexachloride undergoes a phase transition to yield the α-WCl_6-type structure.

The first product can be obtained after heating the mixture of WCl_6 with excess of Co powder at 145 °C for longer period of time (10 days). Series of separate experiments with different amount of cobalt powders were performed to investigate the reducing role of metal powder in more detail. Co_xWCl_6 revealed an increasing unit cell volume with increasing reaction time and increasing excess of metal powder.

These experiments revealed an expansion of the unit cell volume for series of Co_xWCl_6 compounds in the order of $\Delta V = 10$ Å^3, which is graphically displayed in Figure 26. An indication for the intercalation of WCl_6 with cobalt is given by the increase of (*c*-) lattice parameters from 16.800(1) Å to 17.101(4) Å. The largest obtained unit cell volume of Co_xWCl_6 ($V = 553.8(2)$ Å^3) is clearly larger than values reported for α-WCl_6 ($V = 543.3(1)$ Å^3[36] or $V = 534.9(1)$ Å^3[2]).The behavior of Co ions seem to be quite similar to another metal ions used for

the reduction in *M*-W-Cl (*M* = Mn, Fe) systems. The saturation of the metal uptake seems to emerge with a large excess of metal powder.

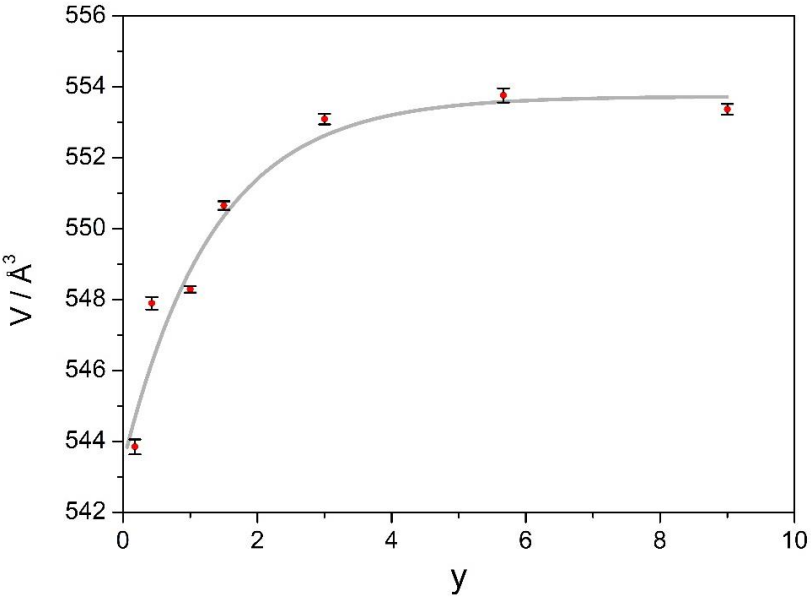

Figure 26. Unit cell volume of $W(Co_x)Cl_6$ phase as a function of excess (y) of cobalt powder.

Characterization of CoW_2Cl_{10}

Powders of CoW_2Cl_{10} behave stable in air. The crystal structure of CoW_2Cl_{10} was refined from X-ray powder data and is isotypic with the structure of MW_2Cl_{10} (*M* = Mn,[32] Fe[33,35]). The structure is composed of hexagonal closest packed layers of chloride ions stacked along the *c*-axis direction. Cations of both types occupy 3/5 of octahedral sites in every second interlayer in an ordered way. Adjacent tungsten atoms in bioctahedral centers are shifted towards each other to form dimers at a W–W distance of 2.737(8) Å. This distance is close to the distance that is considered as a double bond in WCl_4 (2.688(2) Å,[5] 2.713(3) Å[6]). The overall structure can be considered as a cation deficient derivative of a CdI_2-type structure.

Characterization of "$Co_2W_2Cl_{10}$"

Powders of "$Co_2W_2Cl_{10}$" were indexed isotypically to the crystal structure refined for $Fe_2W_2Cl_{10}$.[34,35] The structure of $Fe_2W_2Cl_{10}$ represents a stuffed derivative of $Fe_2W_2Cl_{10}$, where cations of both types occupy 4/5 of octahedral sites in every second interlayer, in an ordered way. However, intensity differences observed in the X-ray powder patterns indicate some deviations in the crystal structure of "$Co_2W_2Cl_{10}$". According to our initial X-ray powder structure refinement studies, cobalt atoms are distributed over several octahedral sites in every second interlayer of the structure. However, high quality structure refinements are hindered by the poor scattering power of cobalt for Cu-$K_{\alpha1}$ radiation.

Characterization of $(Co,W)_{1-x}Cl_2$

The phase which we describe here as $(Co,W)_{1-x}Cl_2$ appears as a dark-green almost black powder which behaves stable in air and against ethanol. Its formation is assigned to one of the closely adjacent exothermic DSC signals near 380 °C. Single-phase samples of $(Co,W)_{1-x}Cl_2$ were obtained by removing the coproduced $CoCl_2$ with ethanol. The X-ray powder pattern was indexed isotypically to the crystal structure of $CoCl_2$ ($CdCl_2$-type) which is represented by a cubic closest packing of chloride ions and cations occupying all octahedral sites in every second interlayer. Neutron diffraction studies on $CoCl_2$ (*R-3*, Z = 3) have revealed a unit cell volume V = 189.78 Å^3,[47] which is significantly larger than the corresponding volume of $(Co,W)_{1-x}Cl_2$ (176.17(4) Å^3).

The composition of a sample of $(Co,W)_{1-x}Cl_2$ was analyzed as $(Co_{0.24}W_{0.43})Cl_2$ by EDX analysis. A variation of *y* would explain small changes of the unit cell volume obtained for this phase.

Characterization of CoW_6Cl_{14}

CoW_6Cl_{14}, as a light gray crystalline powder, can be obtained at around 475 °C, presented in DSC diagram as a last endothermic signal. The crystal structure of CoW_6Cl_{14} is cubic with a = 12.525(1) Å, and build up from $[W_6Cl_{14}]^{2-}$ units and Co^{2+} cations filling octahedral voids between them. Cobalt atoms are octahedrally surrounded through chlorido ligands belonging to the $[W_6Cl_{14}]^{2-}$ cluster. The arrangement of cobalt cations and cluster anions in the crystal

structure of CoW_6Cl_{14} fallows the arrangement of sodium cations and chloride anions in NaCl. Isotypic compounds are presented for MW_6Cl_{14} (M = Mn, Fe, Ni).

Magnetic Measurement

Crystalline samples of compounds were loaded into gelatine capsules under argon atmosphere (glovebox) and their magnetic susceptibilities were recorded with a SQUID magnetometer with a magnetic field of 50000 Oe for CoW_2Cl_{10} and $(Co,W)_{1-x}Cl_2$, and 1000 Oe for CoW_6Cl_{14} in the temperature range 5 K ≤ T ≤ 300 K with progressive steps. The susceptibility of cobalt compounds was fitted following an extended Curie-Weiss law ($\chi = C / (T - \theta) + \chi_0$). Magnetic susceptibility measurements performed for CoW_2Cl_{10}, $(Co,W)_{1-x}Cl_2$, and CoW_6Cl_{14} are shown in Figure 27.

In CoW_2Cl_{10} and $(Co,W)_{1-x}Cl_2$ samples a small amount of not fully removed $CoCl_2$ is present, which has a big influence on the calculated value of μ_B, obtained through the fit with an extended Curie-Weiss law. The magnetic structure of $CoCl_2$ is composed of hexagonal closest packed layers of ferromagnetically aligned Co^{2+} spins with a strong anisotropy confining the spins parallel to the hexagonal axis. Alternating layers in this structure are coupled weakly antiferromagnetically to each other so that the overall magnetic structure is antiferromagnetic below T_N = 24.9 K.[47] This effect can be also observed in magnetic measurements performed with iron compounds, were $FeCl_2$ has a similar strong influence like $CoCl_2$.

For CoW_2Cl_{10} and $(Co,W)_{1-x}Cl_2$ samples effect coming from $CoCl_2$ can be observed at temperatures below 50 K as a deviation from linearity (Figure 27. a) and b)).

The corresponding values for CoW_2Cl_{10} and $(Co,W)_{1-x}Cl_2$ are too high, which can be addressed to the presence of the $CoCl_2$ side-phase. The fit for CoW_6Cl_{14} yields with 4.0 μ_B, what corresponds to the expected value for 3 unpaired electrons of Co^{2+}, which equals $\mu_{s.o.}$ = 3.87 μ_B (according to spin-only). $(Co,W)_{1-x}Cl_2$ and CoW_6Cl_{14} compounds shows linearity in a wide temperature range according to the paramagnetic behavior of both compounds.

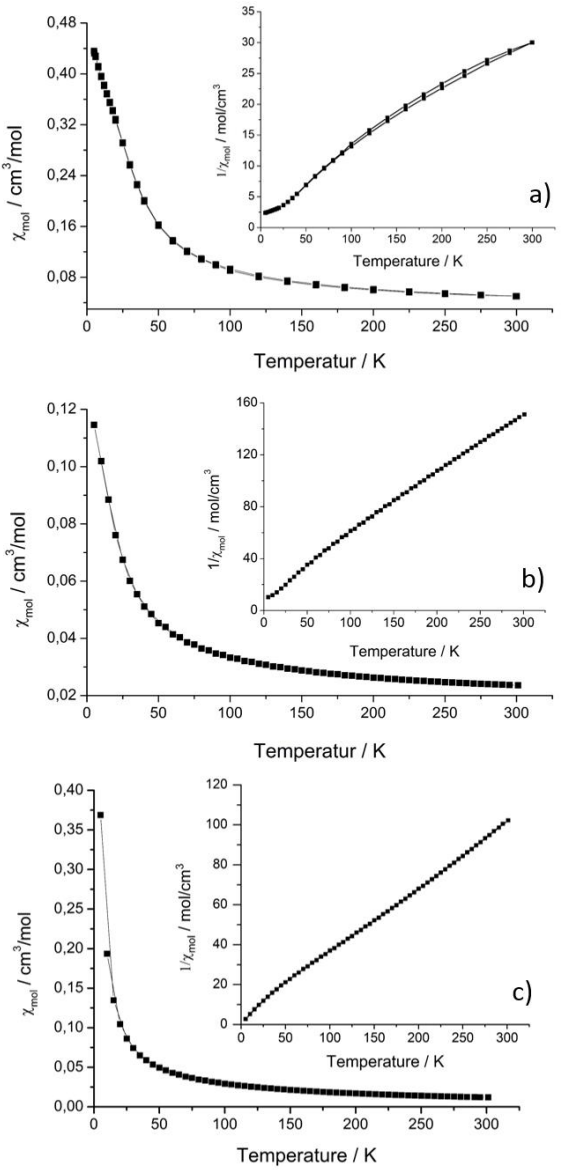

Figure 27. Temperature dependency of the magnetic susceptibilities of a) CoW_2Cl_{10}, b) $(Co,W)_{1-x}Cl_2$ and c) CoW_6Cl_{14}.

4.4. Ni-W-Cl System

Thermal Analysis of Ni-W-Cl System

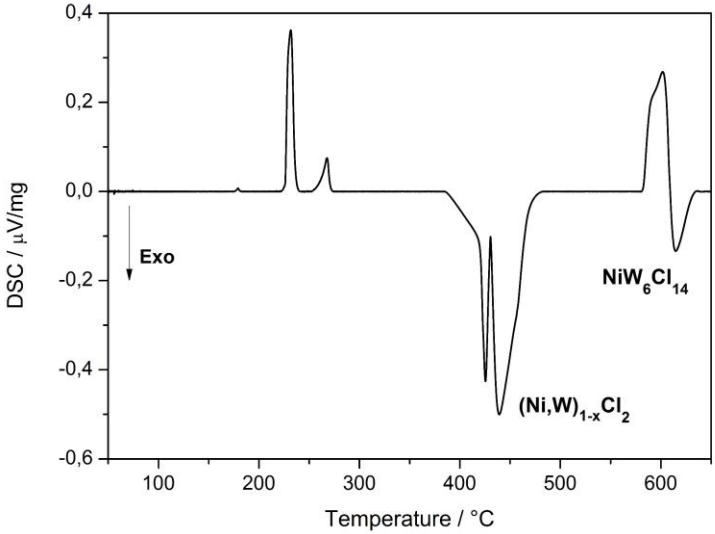

Figure 28. Thermal scanning (DSC) of a Ni-W-Cl system.

The next applied reducing metal is nickel. The reduction of WCl_6 is performed with an appropriate amount of nickel powder, allowing for the complete reduction of tungsten. As it turned out in the present reaction, the final product of the reaction (17) is NiW_6Cl_{14}.

$$6\ WCl_6 + 12\ Ni \rightarrow NiW_6Cl_{14} + 11\ NiCl_2 \qquad (17)$$

Around 40 mg 1:2 molar mixture of β-WCl_6 and nickel powder was mixed and enclosed into a gold plated steel container. This was heated in DSC mode of a thermal analyser with a heating rate of 2 °C/min between room temperature and 650 °C (Figure 28).

Detection of compounds in the Ni-W-Cl system was successfully performed thanks to the systematic investigation of the products through DSC measurement, with help of XRD.

The first endothermic effect can be interpreted as a sublimation of $WOCl_4$, which small amounts are always presented together with β-WCl_6. The following two endothermic effects can be addressed to the sublimation and melting of tungsten hexachloride, respectively. The same

pattern has been confirmed by a separate study in which only β-WCl_6 was employed, and is also presented in iron and cobalt systems.

The signal, which appears between 420 and 460 °C, is cut into two signals with an endothermic effect which belongs to the sublimation of WCl_4, also presented in Fe-W-Cl system at around 400 °C. This main exothermic effect is first reduction step of tungsten hexachloride and corresponds to $(Ni,W)_{1-x}Cl_2$. The last endothermic effect can be explained as a formation of a melt of $(Ni,W)_{1-x}Cl_2$. This signal smoothly transforms into an exothermic effect, last reduction step of WCl_6, which is NiW_6Cl_{14}.

In Ni-W-Cl system two products are characterized by X-ray powder diffraction (Figure 29).

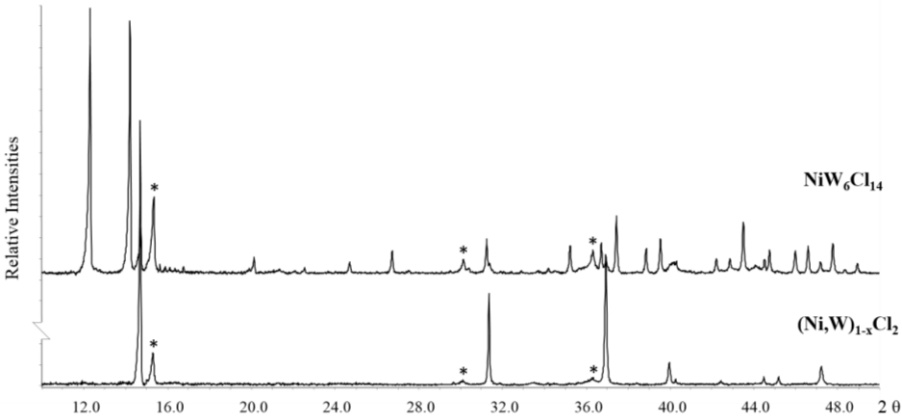

Figure 29. X-ray powder patterns of compounds obtained in the Ni-W-Cl system. Composition of products and preparation temperature are given. Side phases are marked for $NiCl_2$ (*).

Synthesis of the Products in Ni-W-Cl System

DSC experiments and separate preparations in silica tubes are performed under essentially similar conditions as in other systems. Later on, reaction conditions were individually modified in order to obtain well-crystallized high yield products or single crystals. Individually optimized reaction conditions are given as follows:

$(Ni,W)_{1-x}Cl_2$ was obtained as black block crystal after heating a mixture of β-WCl_6 with nickel powder in 1:2 molar ratio at 440 °C for 48 hours following reaction (18).

$$6\ WCl_6 + 12\ Ni \rightarrow 6\ (Ni,W)_{1-x}Cl_2 + 6\ NiCl_2 + Ni \qquad (18)$$

NiW_6Cl_{14} was obtained as black block crystal after heating a mixture of β-WCl_6 with copper powder in 1:2 molar ratio at 600 °C for 2 hours following reaction (19).

$$6\ WCl_6 + 12\ Ni \rightarrow NiW_6Cl_{14} + 11\ NiCl_2 \qquad (19)$$

Characterization of $(Ni,W)_{1-x}Cl_2$

The first product synthetized at 440 °C $(Ni,W)_{1-x}Cl_2$ appears as a dark almost black powder which behaves stable in air. Single-phase samples of $(Ni,W)_{1-x}Cl_2$ were obtained by removing the coproduced $NiCl_2$ with water and nickel powder excess with 15 % solution of HNO_3. The X-ray powder pattern was indexed isotypically to the crystal structure of $NiCl_2$ ($CdCl_2$-type) (Figure 30), which is represented by a cubic closest packing of chloride ions and cations occupying all octahedral sites in every second interlayer. The unit cell volume of published $NiCl_2$ compound equals V = 182.8(7) $Å^3$,[64] which is considerable larger than the corresponding volume of $(Ni,W)_{1-x}Cl_2$ (V = 173.74(1) $Å^3$).

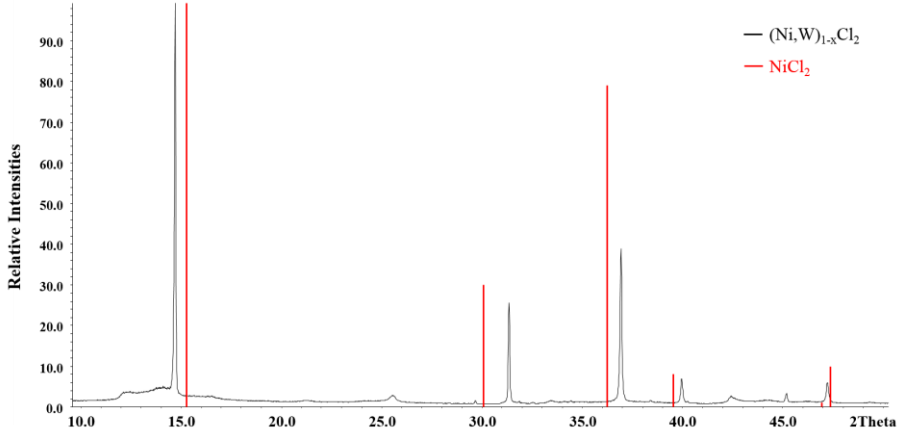

Figure 30. X-ray powder pattern of $(Ni,W)_{1-x}Cl_2$ and reflections of $NiCl_2$ (red).

EDX data were collected for $(Ni,W)_{1-x}Cl_2$. Additional picture were recorded with an EMS JEOL JSM-6500F is presented on the Figure 31. There presented crystals can achieve the size up to 1 mm and they are build up from layer, which seems to be minimally moved in the plane. This impedes the precise characterization of $(Ni,W)_{1-x}Cl_2$.

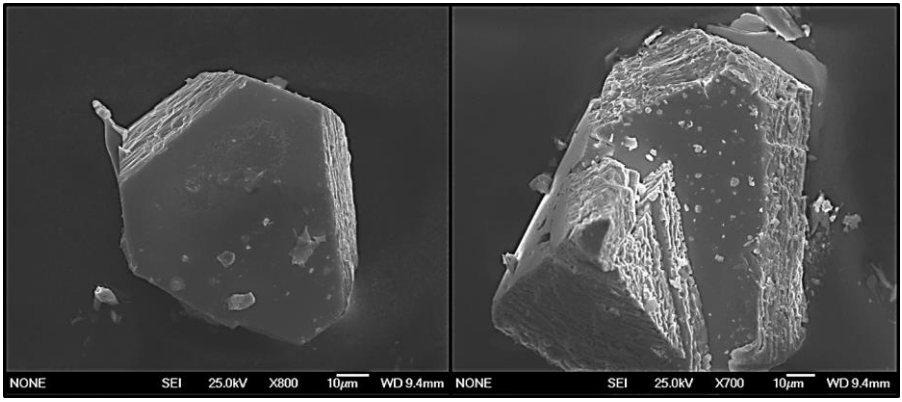

Figure 31. Picture of $(Ni,W)_{1-x}Cl_2$ made with an Electron Scanning Microscope JEOL JSM-6500F.

The composition of $(Ni,W)_{1-x}Cl_2$ sample was analyzed with EDX method as average composition $(Ni_{0.21}W_{0.54})Cl_2$. Series of crystals analyzed with use of EDX, EMS shows small differences in the composition, which closes in the range of 5 % measurement error. Taking an assumption, that nickel is in divalent and tungsten in trivalent oxidation state the corresponding charge balanced phase can be described as $(Ni_{1-y}W_{2/3y})Cl_2$. A variation of *y* would explain small changes of the unit cell volume obtained for this phase.

Characterization of NiW_6Cl_{14}

The second and the last nickel compound is characterized isotopically to series of MW_6Cl_{14} (*M* = Mn, Fe, Co) products. NiW_6Cl_{14} crystalized cubically in the space group *Pn-3* with $a = 12.476(1)$ Å. NiW_6Cl_{14} is build up from $[W_6Cl_{14}]^{2-}$ cluster anions and Ni^{2+} cations placed in octahedral voids between them. Terminal chlorido ligands form six $[W_6Cl_{14}]^{2-}$ are surrounding octahedrally nickel atoms.

4.5. Cu-W-Cl System

Thermal Analysis of Cu-W-Cl System

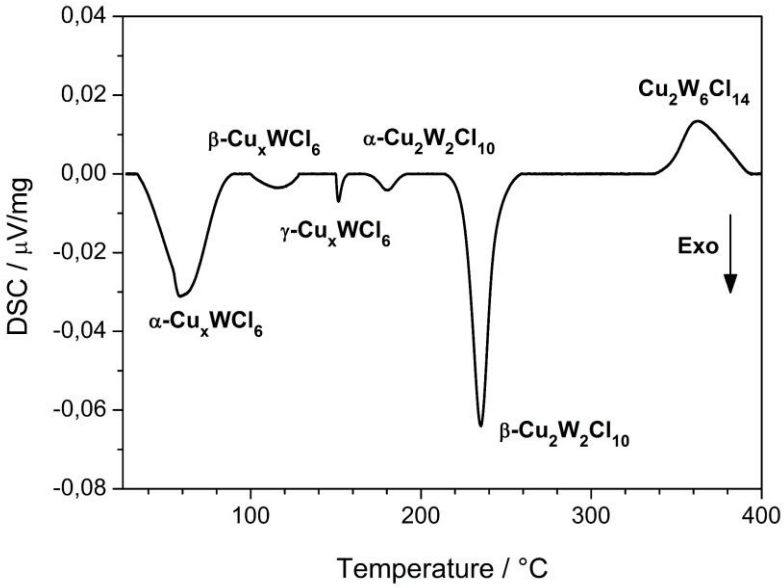

Figure 32. Thermal scanning calorimetry (DSC) of the reaction of β-WCl_6 with elemental copper powder (corrected for background). Compounds are assigned to their supposed formation effects. "Exo" denotes an exothermic thermal effect in the DSC.

The last studied in this work reduction element is copper. The reaction between β-WCl_6 and elemental copper powder (ca. 40 mg) was investigated in a DSC apparatus. A slow heating rate (2 °C/ min) up to 400 °C, allows the detection of a heat consumption or release caused during the formation of intermediate phases in the Cu-W-Cl system. The used molar ratio of 1:4, shown in reaction (20), was chosen to allow for a complete reduction of tungsten to the lowest oxidation state in $Cu_2W_6Cl_{14}$. The reduction of β-WCl_6 with elemental copper powder results in a series of six DSC signals, shown in Figure 32, which are addressed to the compounds α-Cu_xWCl_6, β-Cu_xWCl_6, γ-Cu_xWCl_6, α-$Cu_2W_2Cl_{10}$, β-$Cu_2W_2Cl_{10}$, and finally to the formation of $Cu_2W_6Cl_{14}$, according to the results of X-ray diffraction studies.

$6\ WCl_6 + 24\ Cu \rightarrow Cu_2W_6Cl_{14} + 22\ CuCl$ (20)

The first observed exothermic effect near 60 °C represents a reductive intercalation of copper ions into the structure of β-WCl_6 with the formation of monoclinic α-Cu_xWCl_6. The broad exothermic effect slightly above 100 °C corresponds to the formation of monoclinic β-Cu_xWCl_6, followed by the formation of orthorhombic γ-Cu_xWCl_6 near 150 °C. Separate reactions revealed, that α-Cu_xWCl_6 and β-Cu_xWCl_6 can be transformed into γ-Cu_xWCl_6 by prolonging the reaction time without changing the reaction temperature.

The following two exothermic effects near 180 °C and 230 °C correspond to the formation of $Cu_2W_2Cl_{10}$, which appears dimorphic. Both modifications are separately prepared and structurally characterized. The first phase is characterized as triclinic α-$Cu_2W_2Cl_{10}$, and the second as tetragonal β-$Cu_2W_2Cl_{10}$.

The transition from Cu_xWCl_6 phases to $Cu_2W_2Cl_{10}$ modifications requires a structural reorganization, because one type of structure contains isolated [WCl_6] octahedra and the other edge-sharing [W_2Cl_{10}] bioctahedra. This change could be accomplished by diffusion of tungsten ions from one octahedral site to another octahedral site within the hexagonal closest packing of chloride ions.

The final step of the successive reduction of WCl_6 with copper powder is the endothermic formation of $Cu_2W_6Cl_{14}$, which again requires a major reconstruction of the structure. $Cu_2W_6Cl_{14}$ crystallizes isotypic to $Cu_2W_6Br_{14}$[65] containing the well-known octahedral $[(M_6X_8)X_6]^{2-}$ cluster (M = metal, X = halide).

The transformation of isolated [WCl_6] octahedra into dimeric edge-bridging [W_2Cl_{10}] bioctahedra, and then into octahedral [W_6X_8] clusters is a structural consequence of the reduction of WCl_6 with copper powder, described in reaction (20).

Synthesis of Products in Cu-W-Cl System

The XRD powder patterns of five new compounds in the Cu-W-Cl system, as well as the known pattern of $Cu_2W_6Cl_{14}$, are displayed in Figure 33. All these compounds were prepared in separate reactions from β-WCl_6 and copper powder in accord to their formation conditions in the DSC measurement. CuCl is obtained as a side-phase. A contamination with small amounts of oxide seems often unavoidable in such reactions, indicated by the presence of small amounts of $WOCl_4$.

Mixtures of β-WCl_6 and copper powder, with total masses around 150 mg, were prepared under argon atmosphere (glovebox), placed into homemade quartz ampules (inner diameter: 0.7 cm, length: 3 cm), and sealed therein under vacuum while cooling the mixtures with liquid nitrogen. Later on, reaction conditions were individually revised in order to obtain well-crystallized high yield products or single crystals. All products, except for $Cu_2W_6Cl_{14}$, were handled under inert gas atmosphere (argon) because they easily decompose in air.

Individually optimized reaction conditions are performed as follows:

α-Cu_xWCl_6 was obtained as black crystalline powder after heating a mixture of β-WCl_6 with copper powder in 1:x (x = 0.58–1) molar ratio at 60 °C for 10 hours following reaction (21).

$$WCl_6 + x\ Cu \rightarrow Cu_xWCl_6 \quad (21)$$

The employment of copper powder quantities larger than x = 0.58 always resulted in a residue of copper under given conditions.
A reaction between β-WCl_6 and elemental copper powder is already obtained when grinding the mixture at room temperature for a few minutes, indicated by a colour change. The XRD powder pattern revealed the absence of the starting material β-WCl_6, but the crystallinity of the product is poor.

β-Cu_xWCl_6 (x = 0.72) was obtained as black crystalline powder after heating a mixture of β-WCl_6 with excess of copper powder (1:1 molar ratio) at 100 °C for 48 hours, following reaction (21).

γ-Cu_xWCl_6 (x = 0.78) was obtained as black block like crystals after heating a mixture of β-WCl_6 with copper powder in 1:0.78 molar at 150 °C for 10 hours following reaction (21).

α-$Cu_2W_2Cl_{10}$ was obtained as black crystalline powder after heating a mixture of β-WCl_6 with copper powder in 1:2 molar ratio at 200 °C for 2 hours following reaction (22).

$$2\ WCl_6 + 4\ Cu \rightarrow \alpha\text{-}Cu_2W_2Cl_{10} + 2\ CuCl \quad (22)$$

β-$Cu_2W_2Cl_{10}$ was obtained as black block crystal after heating a mixture of β-WCl_6 with copper powder in 1:2 molar ratio at 240 °C for 24 hours following reaction (23).

$$2\ WCl_6 + 4\ Cu \rightarrow \beta\text{-}Cu_2W_2Cl_{10} + 2\ CuCl \quad (23)$$

$Cu_2W_6Cl_{14}$ was obtained as black crystalline powder after heating a mixture of β-WCl_6 with copper powder in 1:4 molar ratio at 350 °C for 48 hours following reaction (24).

$$6\ WCl_6 + 24\ Cu \rightarrow Cu_2W_6Cl_{14} + 22\ CuCl \quad (24)$$

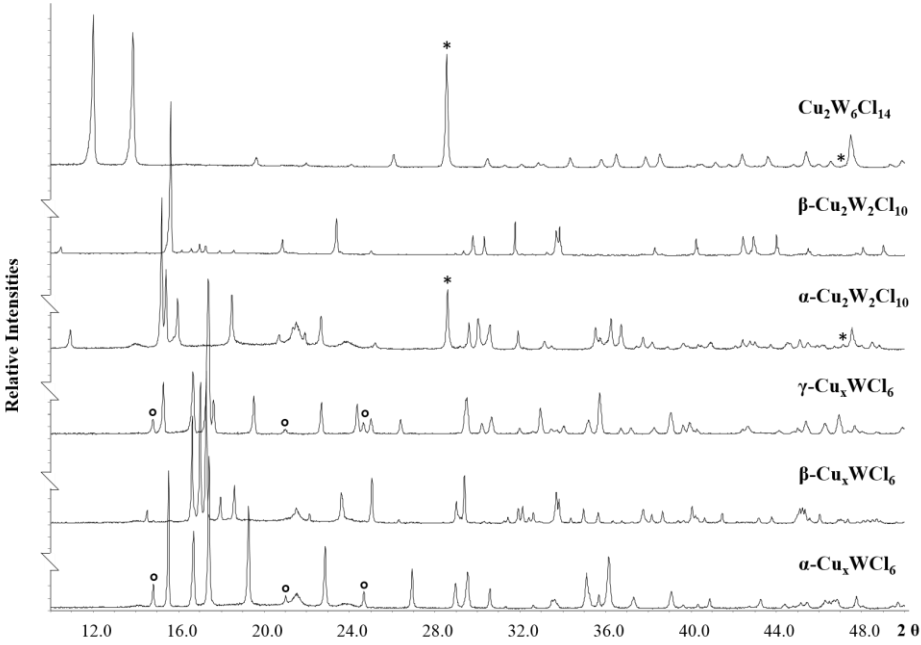

Figure 33. X-ray powder patterns of compounds obtained in the Cu-W-Cl system. Compositions of products and preparation temperature are given. Side phases are marked for CuCl (*) and $WOCl_4$ (°).

Characterization of Cu_xWCl_6

α-Cu_xWCl_6: The crystal structure of α-Cu_xWCl_6 was solved and refined on basis of XRD powder data with the monoclinic space group *C2/m* (Table 6). The amount of copper powder for the synthesis of α-Cu_xWCl_6 was varied in the range x = 0.58 – 1 to determine the phase-width. Below x = 0.58 only X-ray amorphous material was obtained. Refined lattice parameters of α-Cu_xWCl_6 revealed an increase of the unit cell volume from V = 376.50(7) $Å^3$ to V = 383.44(4) $Å^3$ with increasing amount of copper powder used in reactions, as can be seen in Figure 34.

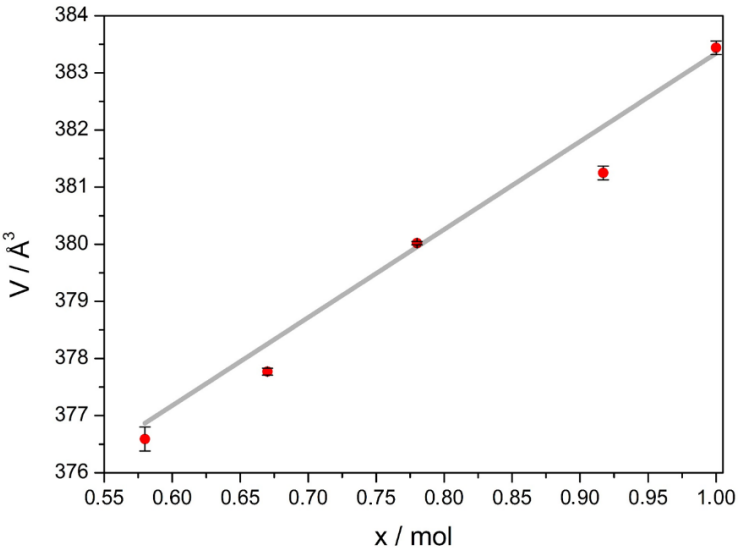

Figure 34. Unit cell volume of α-Cu_xWCl_6 as a function of the copper amount (x) used in the synthesis.

β-Cu_xWCl_6: The X-ray powder diffraction pattern was indexed monoclinically. The crystal structure of β-Cu_xWCl_6 was refined with the space group *C2/m* based on powder XRD data with results presented in Table 6. All equivalent isotropic displacement parameters of copper atoms where restraint to be equal.

γ-Cu_xWCl_6: The crystal structure was refined in the orthorhombic space group *Pnnm*, based on single-crystal XRD data (Table 6).

We note, that compositions and structures of Cu_xWCl_6 phases are refined closely related to each other (Table 6). On course of the reproduction of compounds reported herein, even more crystalline phases were detected in XRD studies, which could not be isolated as pure phases. Hence, assignments between compounds and thermal effects, given in Figure 32, may be affected by the existence of more compounds in the system.

Cu_xWCl_6 phases are obtained as dark green, almost black powders which behave highly hygroscopic in moist air. Their crystal structures are based on hexagonal closest packing (hdp) of chloride ions in which tungsten ions occupy 1/6 of the octahedral voids, thereby forming isolated [WCl_6] units. Copper ions in the Cu_xWCl_6 series are disordered over a few positions

with partial occupations. Figure 35 shows copper ions occupying tetrahedral and octahedral voids in the first phase that is detected in Cu-W-Cl system.

Table 6. Crystallographic data of α-Cu_xWCl_6, β-Cu_xWCl_6 and γ-Cu_xWCl_6.

	α-Cu_xWCl_6	**β-Cu_xWCl_6**	**γ-Cu_xWCl_6**
Empirical formula	$Cu_{0.78}WCl_6$	$Cu_{0.72}WCl_6$	$Cu_{0.77}WCl_6$
Formula weight / g·mol^{-1}	446.169	442.403	445.58
Crystal system	monoclinic	monoclinic	orthorhombic
Space group	*C2/m*	*C2/m*	*Pnnm*
Unit cell dimensions			
a / Å	6.2446(1)	17.6740(2)	17.533(3)
b / Å	10.6486(1)	10.6711(1)	6.1473(9)
c / Å	6.1412(1)	6.14962(7)	10.672(2)
β / °	111.474(1)	96.4309(7)	
Volume / Å^3	380.02(1)	1152.53(2)	1150.2(3)
Z	2	6	6
Density (calculated) / g·cm^{-3}	3.899	3.824	3.860
Absorption coefficient / mm^{-1}	48.954	47.364	19.126
Crystal size / mm^3	powder	powder	0.25 x 0.25 x 0.43
Temperature / K	293(2)	293(2)	293(2)
Theta range for date collection / °	6 – 60	2.5 – 55	2.234 – 25.026
Total number of reflections	331	801	9579
Refined parameters	17	39	86
Goodness-of-fit on F^2	-	-	1.341
Final R indices [I > 2σ(I)]	R_p = 0.0533 R_{wp} = 0.0693	R_p = 0.0464 R_{wp} = 0.0602	R_1 = 0.0379 wR_2 = 0.0802
R indices (all data)	R_{Bragg} = 3.2459	R_{Bragg} = 3.6513	R_1 = 0.0435, wR_2 = 0.0825
Largest diff. peak and hole / e·Å^{-3}	-	-	1.549 and -1.480
χ^2	1.8675	1.225	-

Cu_xWCl_6 phases (x<1) may be considered to involve some tungsten ions having an approximate oxidation state +5. This oxidation state is well-known for $A[WCl_6]$ (A = Li, [39] Cs[66]) compounds containing octahedral $[WCl_6]$ arrangements.

The structure refinement on **α-Cu_xWCl_6** reveals copper ions to occupy octahedral (Cu1, 8j, SOF (site occupation factor) = 0.143(2)) and tetrahedral (Cu2, 4g, SOF = 0.105(3)) voids in each interlayer of the hdp (Figure 35) forming an overall tetrahedra-octahedra-tetrahedra motif displayed in Figure 36 (left). Interatomic Cu(1)–Cu(2) distances between tetrahedral and octahedral positions of 1.731(9) Å indicate that only one type of position can be simultaneously occupied. Distances between adjacent tetrahedral positions of two equivalent Cu(2) ions are equal to 3.15(2) Å.

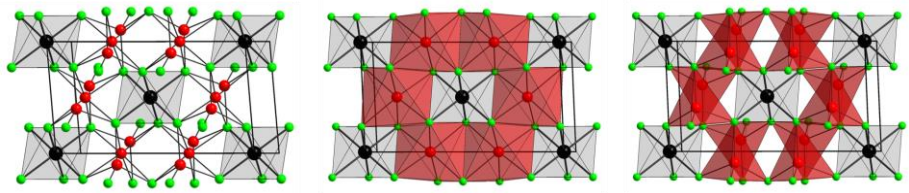

Figure 35. Crystal structure of α-Cu_xWCl_6, with two types of copper sites (left), separately indicated as red octahedral sites for Cu2 (4g, middle) and red tetrahedral sites for Cu1 (8j, right).

The structure refinement on **β-Cu_xWCl_6** revealed copper ions distributed over three crystallographic sites (Cu1-3, 8j, SOF = 0.213(5), 0.212(5), 0.116(5)), to occupy tetrahedral voids in each hdp interlayer forming $[CuCl_4]$ units, and tetrahedral voids in every third hdp interlayer forming edge-sharing $[Cu_2Cl_6]$ bitetrahedra displayed in Figure 36 (right). The interatomic Cu(1)–Cu(1) distance of 1.925(7) Å suggests the presence of up to one copper ion within this dimeric unit. Corresponding values for Cu(2)–Cu(2) and Cu(2)–Cu(3) amount to 2.983(8) Å and 2.85(1) Å.

Copper ions in **γ-Cu_xWCl_6** occupy tetrahedral voids distributed over three crystallographic sites (Cu1-3, 8h, SOF = 0.177(8), 0.158(7), 0.264(8)) in each interlayer, forming $[Cu_2Cl_6]$ bitetrahedra (Figure 36, right). Interatomic distances in $[Cu_2Cl_6]$ between Cu(1) and Cu(2) are 2.66(2) Å, between Cu(2) and Cu(3) 2.93(1) Å, and between two symmetry equivalent Cu(3) sites 2.96(1) Å.

A comparison of β-Cu_xWCl_6 and γ-Cu_xWCl_6 structures is presented in Figure 37.

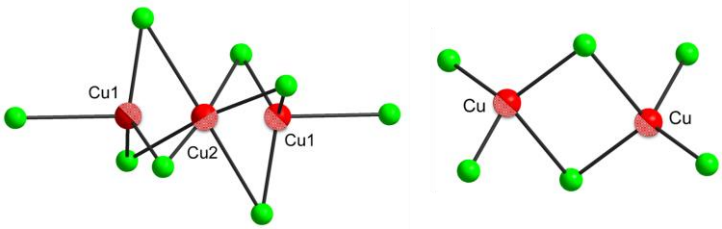

Figure 36. Coordination environment of Cu1 and Cu2 ions in α-Cu_xWCl_6 (left) and coordination of copper cations in edge-sharing $[Cu_2Cl_6]$ bitetrahedra (right) of β-Cu_xWCl_6 and γ-Cu_xWCl_6. Half-marked copper atoms symbolize partial occupations of sites.

A similar type of reduction, with metal incorporation into the structure of WCl_6, is presented for M_xWCl_6 compounds with M = Mn, Fe, and Co. Their crystal structures are also based on a hexagonal closest packing (hcp) arrangement of chloride ions and variable amounts of M ions occupying up to 1/3 octahedral voids in every second interlayer.

In contrast to these compounds it can be note the presence of copper ions in octahedral and tetrahedral (α-Cu_xWCl_6) or tetrahedral interstices in every interlayer (β-Cu_xWCl_6 and γ-Cu_xWCl_6).

The compositions of Cu_xWCl_6 phases appear closely related to each other. A significant phase-width is found for α-Cu_xWCl_6 (Figure 34) and may be also existent in other phases. The phase-with, the sensitivity of Cu_xWCl_6 compounds against hydrolysis, and the presence of CuCl and unreacted copper powder in reaction products make analytical studies difficult to perform.

A more important issue should be the oxidation states present for copper and tungsten in the structures. Cu–Cl distances in α-Cu_xWCl_6, β-Cu_xWCl_6, and γ-Cu_xWCl_6 are $\bar{d}_{Cu\text{-}Cl}$ = 2.28(1) Å, $\bar{d}_{Cu\text{-}Cl}$ = 2.275(8) Å and $\bar{d}_{Cu\text{-}Cl}$ = 2.274(1) Å. These values appear shorter than in other compounds with Cu^+ ions in tetrahedral surroundings such as in $Cu[W_6CCl_{18}]$ ($\bar{d}_{Cu\text{-}Cl}$ = 2.387(1) Å)[67], $CsCu_2Cl_3$ ($\bar{d}_{Cu\text{-}Cl}$ = 2.382(1) Å)[68] or $[N(CH_3)_4][Cu_2Cl_3]$ ($\bar{d}_{Cu\text{-}Cl}$ = 2.406(1) Å)[69]. At the same time these distances are longer than those reported for Cu^{2+} ions in compounds such as Cs_2CuCl_4 ($\bar{d}_{Cu\text{-}Cl}$ = 2.205(2) Å)[70], $[(CH_3)_4N]_2[CuCl_4]$ ($\bar{d}_{Cu\text{-}Cl}$ = 2.243.(1) Å)[71] and $(C_7N_3H_{14})_2[CuCl_4]$ ($\bar{d}_{Cu\text{-}Cl}$ = 2.251(2) Å)[72].

From this comparison it seems that distances between copper and chloride ions in Cu_xWCl_6 phases do not compare well with literature values of compounds containing Cu^+ and Cu^{2+} ions, which may be related to the low site occupancies of copper ions in Cu_xWCl_6 phases. This may

be understood when looking at the lattice expansion shown for α-Cu_xWCl_6 in Figure 34 and to the interplay with the oxidation state of tungsten in Cu_xWCl_6 phases.

The comparison of all Cu-W-Cl products with another compounds is shown in Table 7, together with coordination number (CN) of copper ions.

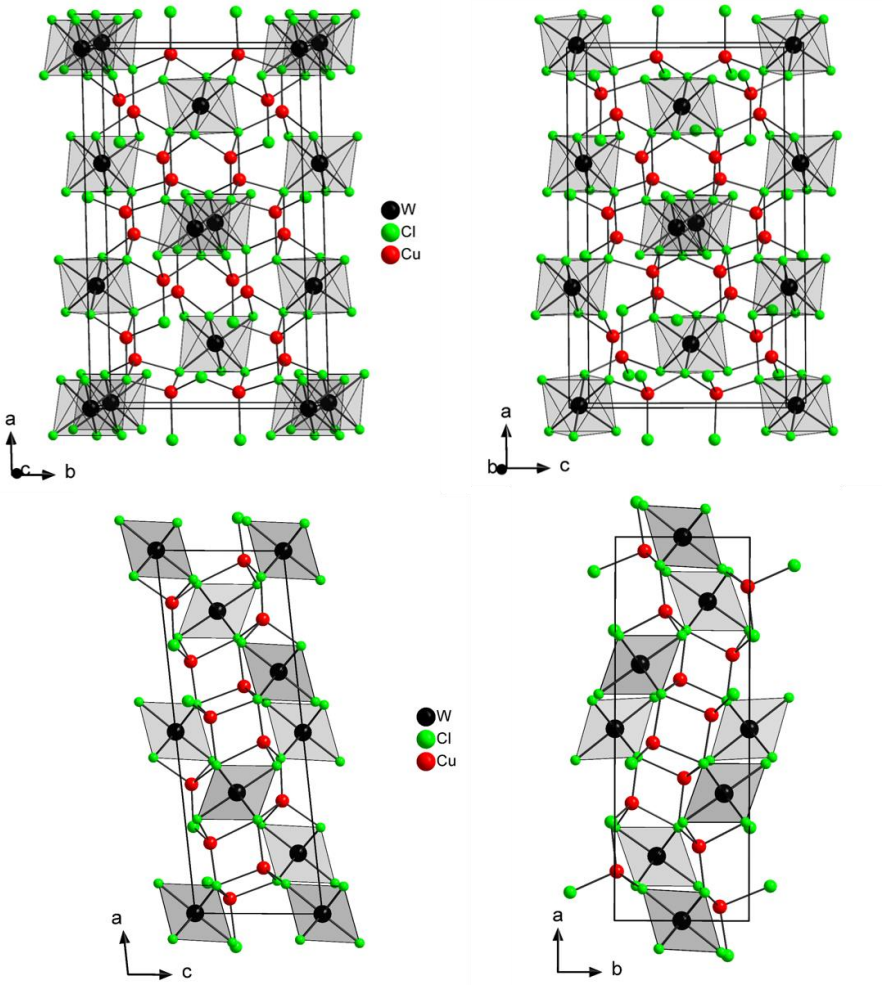

Figure 37. Crystal structures of β-Cu_xWCl_6 (left) and γ-Cu_xWCl_6 (right). The bottom view of both Cu_xWCl_6 structures is rotated by 90 ° around the *a*-axis.

Table 7. Distance ranges (Å), average values (Å) and coordination numbers (CN) in α-Cu_xWCl_6, β-Cu_xWCl_6, γ-Cu_xWCl_6, α-$Cu_2W_2Cl_{10}$, β-$Cu_2W_2Cl_{10}$ and $Cu_2W_6Cl_{14}$ products in comparison to some other compounds.

	d_{Cu-Cl} / Å $\bar{d}$ **, CN**	d_{Cu-Cu} / Å
α-Cu_xWCl_6	2.13(1) – 2.638(3) **2.285(1), 4** **2.55(1), 6**	1.731(9) – 3.15(2)
β-Cu_xWCl_6	2.13(1) – 2.48(1) **2.283(1), 4**	1.97(3) – 2.90(2)
γ-Cu_xWCl_6	2.127(9) – 2.492(9) **2.274(1), 4**	2.66(2) – 2.95(1)
α-$Cu_2W_2Cl_{10}$	2.221(6) – 2.320(6) **2.257(1), 3**	–
β-$Cu_2W_2Cl_{10}$	**2.411(2)** x 4**, 4**	–
$Cu_2W_6Cl_{14}$	**2.24(1)** x 3**, 3**	–
$Cu[W_6CCl_{18}]$[67]	2.345(6) – 2.503(7) **2.387(1), 4**	2.59(1) – 2.66(1)
$CsCu_2Cl_3$[68]	2.166(7) – 2.534(6) **2.382(1), 4**	2.797(1) – 3.119(3)
$[N(CH_3)_4][Cu_2Cl_3]$[69]	2.255(2) – 2.574(2) **2.406(1), 4**	2.869(2) – 3.197(2)
Cs_2CuCl_4[70]	2.18(1) – 2.26(2) **2.205(2), 4**	–
$[(CH_3)_4N]_2[CuCl_4]$[71]	2.218(5) – 2.268(6) **2.243.(1), 4**	–
$(C_7N_3H_{14})_2[CuCl_4]$[72]	2.243(1) – 2.248(1) **2.251(2), 4**	–

Characterization of α-$Cu_2W_2Cl_{10}$ and β-$Cu_2W_2Cl_{10}$

α-$Cu_2W_2Cl_{10}$: Black crystalline powders of α-$Cu_2W_2Cl_{10}$ were inspected by XRD and the crystal structure was refined with the space group $P\bar{1}$ (Table 8). The crystal structure shown in the Figure 38 (top) is composed of hcp layers of chloride ions stacked along the *b*-axis direction in which tungsten ions occupy (2/5) octahedral sites in every second interlayer. Adjacent tungsten atoms are arranged in bioctahedral [W_2Cl_{10}] units in which they are shifted towards each other to form short W–W contacts at 2.717(3) Å. Copper ions can be described to occupy (2/5) octahedral sites in every second interlayer. However, they are strongly displaced from the octahedral sites to occupy nearly trigonal coordinated sites with an angular deviation of the trigonal plane of about 8°. Each [$CuCl_3$] unit interconnects three independent [W_2Cl_{10}] units. Cu–Cl distances range between 2.221(6) and 2.320(6) Å ($\bar{d}_{Cu\text{-}Cl}$ = 2.258(6) Å). A similar coordination environment of copper has been reported for Cu^+ ions in $Cu_2W_6Cl_{14}$ with $d_{Cu\text{-}Cl}$ = 2.24(1) Å, as will be discussed later.

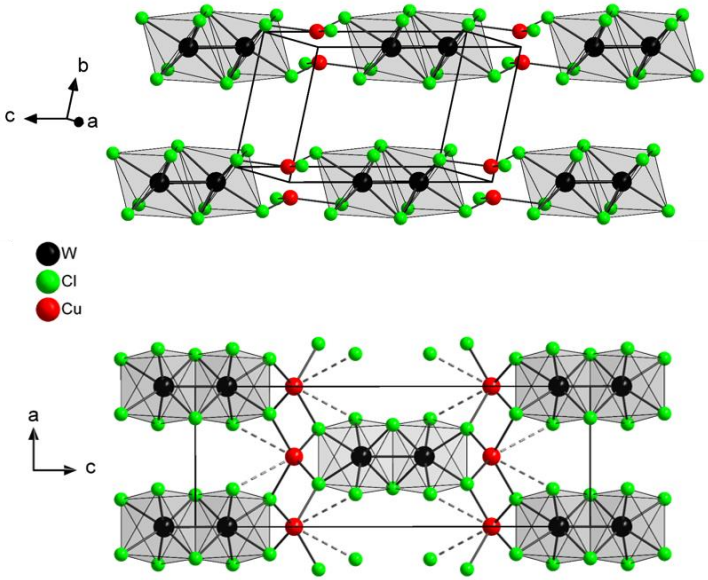

Figure 38. Crystal structures of α-$Cu_2W_2Cl_{10}$ (top) and β-$Cu_2W_2Cl_{10}$ (bottom). Tetrahedral environments of copper ions in β-$Cu_2W_2Cl_{10}$ are indicated with the deviation from octahedral environments (dashed lines).

β-$Cu_2W_2Cl_{10}$: α-$Cu_2W_2Cl_{10}$ can be transformed into black block like crystals of β-$Cu_2W_2Cl_{10}$ at 210 °C. The crystal structure of β-$Cu_2W_2Cl_{10}$ was refined with the tetragonal space group *$P4_2/mnm$* on basis of single-crystal XRD data (Table 8).

The crystal structure is composed from a hcp of chloride layers stacked along the *b*-axis direction. Copper and tungsten ions occupy (2/5) octahedral sites in every interlayer in an ordered fashion. Adjacent tungsten atoms in bioctahedral centers are shifted towards each other to form dimers at a W–W distance of 2.698(1) Å. This distance is close to the distance that is considered as a double bond in WCl_4 (2.688(2) Å,[5] 2.713(3) Å[6]).

Copper ions are displaced from octahedral centers to be situated in a tetrahedral environment of chloride ions (Figure 38, bottom). All interatomic distances between copper and chloride ions in β-$Cu_2W_2Cl_{10}$ are equal to 2.411(2) Å, which is a typical distance for Cu^+.

Further analytical studies were not possible to perform due to the strong air instability of α-$Cu_2W_2Cl_{10}$ and β-$Cu_2W_2Cl_{10}$.

Closely related crystal structures were reported for MW_2Cl_{10} (M = Mn, Fe, Co). Both types of structures, $Cu_2W_2Cl_{10}$ and MW_2Cl_{10}, contain edge-sharing bioctahedra, which are well-known from neutral [W_2Cl_{10}] in WCl_5, with a nonbonding W–W distance of 3.814(2) Å.[4]

A study on the electronic situation of the W–W bonding within edge-sharing bioctahedra was reported for FeW_2Cl_{10} and $Fe_2W_2Cl_{10}$.[35] The [W_2Cl_{10}] unit in FeW_2Cl_{10} is in the oxidation state 2-, while in $Fe_2W_2Cl_{10}$ the [W_2Cl_{10}] unit has the oxidation state 4-, as has been confirmed through the presence of Fe^{2+} by Mössbauer spectroscopy. Interatomic distances between tungsten atoms in $Fe_2W_2Cl_{10}$ are at 2.637(1) Å, and thereby only slightly shorter than those in FeW_2Cl_{10} with 2.707(5) Å. This is explained with a simultaneous occupation of weakly bonding δ and antibonding δ* orbitals. Interatomic W–W distances refined for α-$Cu_2W_2Cl_{10}$ (2.717(3) Å) and β-$Cu_2W_2Cl_{10}$ (2.698(1) Å) can be interpreted to indicate a $[W_2Cl_{10}]^{2-}$ ion.

Table 8. Crystallographic data of α-$Cu_2W_2Cl_{10}$ and β-$Cu_2W_2Cl_{10}$.

	α-$Cu_2W_2Cl_{10}$	**β-$Cu_2W_2Cl_{10}$**
Empirical formula	$Cu_2W_2Cl_{10}$	$Cu_2W_2Cl_{10}$
Formula weight / g·mol^{-1}	849.319	849.28
Crystal system	triclinic	tetragonal
Space group	$P\bar{1}$	$P4_2/mnm$
Unit cell dimensions		
a / Å	6.1738(1)	6.007(1)
b / Å	6.2626(1)	
c / Å	9.0390(2)	16.900(2)
α / °	102.600(1)	
β / °	109.274(1)	
γ / °	101.653(1)	
Volume / Å^3	307.38(1)	609.8(1)
Z	2	4
Density (calculated) / g·cm^{-3}	4.5879	4.625
Absorption coefficient / mm^{-1}	56.158	24.381
Crystal size / mm^3	powder	0.4 x 0.32 x 0.28
Temperature / K	293(2)	293(2)
Theta range for date collection / °	2.5 – 55	3.60 – 25.91
Total number of reflections	818	6145
Refined parameters	30	24
Goodness-of-fit on F^2	-	1.085
Final R indices [I > 2σ(I)]	R_p = 0.0476, R_{wp} = 0.0623	R_1 = 0.0316, wR_2 = 0.0812
R indices (all data)	R_{Bragg} = 4.3711	R_1 = 0.0331, wR_2 = 0.0825
Largest diff. peak and hole / e·Å^{-3}	-	1.847 and -1.817
χ^2	1.6894	-

Characterization of $Cu_2W_6Cl_{14}$

A greenish-yellow crystal powder of $Cu_2W_6Cl_{14}$ was indexed consistent with the cubic crystal space group $Pn\bar{3}$ with a = 12.8030(3) Å. The thermal scanning method demonstrates the formation of $Cu_2W_6Cl_{14}$ at a much lower temperature (below 400 °C) than previously reported (above 600 °C). $Cu_2W_6Cl_{14}$ was reported in 1998[73] and described isotypically to $Cu_2W_6Br_{14}$.[65] Copper ions are coordinated in a trigonal planar fashion by three Cl^a ions of $[(W_6Cl_8^i)Cl_6^a]^{2-}$ (Figure 39). All Cu-Cl distances and Cl-Cu-Cl angles are equal, at 2.24(1) Å and 119.9(4) °, respectively. Crystalline powders of $Cu_2W_6Cl_{14}$ behave stable in air and against air moisture.

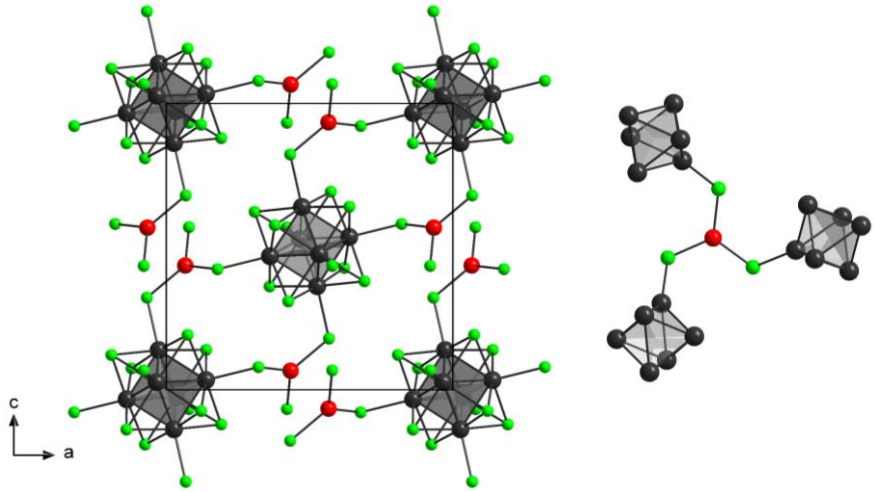

Figure 39. Unit cell of $Cu_2W_6Cl_{14}$ and coordination of Cu^+ cations in $Cu_2W_6Cl_{14}$.

4.6. Reduction of WCl_6 with Copper and Hexachlorobenzene

The reduction of β-WCl_6 with copper also yield some new compounds, among them the new $Cu[W_6CCl_{18}]$ containing an interstitial carbon atom.

In 2003 the first carbon centered trigonal prismatic tungsten clusters W_6CCl_{16} and W_6CCl_{18} were published by Schnering et al.[9] The first observation of this type of cluster was due to a carbon impurity, but the identity of this type of cluster was confirmed by reduction of WCl_4 with tungsten metal powder and graphite in a temperature gradient around 700 °C, and the presence of carbon was evidenced by ^{13}C-NMR. A few years later a new synthesis route was described for the cluster series of W_6Cl_{18}, W_6CCl_{15}, W_6CCl_{16}, W_6CCl_{18}, $W_{30}C_2(Cl,Br)_{68}$ in which more reactive carbon sources were employed.[10]

The structure of *triprismo*-W_6CCl_{18} cluster follows the motif of the sulfur-centered trigonal prismatic niobium cluster $[Nb_6SBr_{17}]^{3-}$, reported for $A_3[Nb_6SBr_{17}]$ with A = K, Rb, Cs, Tl.[74] The *triprismo*-W_6CCl_{18} cluster can appear as a neutral species having a molecular structure but also as $[W_6ZCl_{18}]^{n-}$ (n = 1, 2, 3) anion containing carbon or nitrogen as an interstitial atom (Z).[11,12] Among $A[W_6ZCl_{18}]$ compounds there exists examples with *A* = Li, Na, Ca, Ag with Z = C, N,[75] and ligand exchange reactions of terminal chlorides by means of solution chemistry were reported to yield $[(W_6ZCl_{12})L_6]^{2-}$ clusters[76].

Here is reported the preparation of $Cu[W_6CCl_{18}]$ with hexachlorobenzene as a carbon source and two derivatives of this cluster compound, $Cu(C_2H_6OS)_6[W_6CCl_{18}]$ and $Cu(C_2H_6OS)_4[W_6CCl_{18}]_2$, obtained after crystallization from (dimethyl sulfoxide, acetone) solution.

Jahn-Teller distorted octahedral copper(II) complexes are known to be good catalysts[77]. Here described Cu-cluster could be a promising starting material for new type of trigonal prismatic tungsten clusters containing copper(II) complexes for catalysis.

Synthesis

$Cu[W_6CCl_{18}]$ (I). $Cu[W_6CCl_{18}]$ was formed by reduction of β-WCl_6 with copper powder and C_6Cl_6 according to reaction (25). Hexachlorobenzene was used instead of graphite which appeared inefficient under conditions which were used. A mixture of 320 mg of β-WCl_6 (0.807 mmol), 171 mg of Cu (2.693 mmol), and 6.5 mg of C_6Cl_6 (0.023 mmol) with total mass of around 500 mg was mixed under argon atmosphere (glovebox), placed into a homemade quartz ampule and sealed under vacuum while cooling the mixture with liquid nitrogen. Afterwards,

the ampule was placed into a Simon-Müller furnace, heated to 700 °C with a heating and cooling rate of 2 °/min, and kept at this temperature for 2 hours. Black powder and block shaped crystals of the product were obtained from the reaction.

$$6\ WCl_6 + 20\ Cu + 1/6\ C_6Cl_6 \rightarrow Cu[W_6CCl_{18}] + 19\ CuCl \quad (25)$$

Compound **(I)** behaves stable in air. In attempt to remove the coproduced CuCl, the reaction product was washed with dimethyl sulfoxide (DMSO), and with ethanol afterwards to dry the product and get rid of DMSO residues. However, it turned out that some amounts of **(I)** were dissolved and finally crystallized from the solution as compound **(II)**.

$Cu(C_2H_6OS)_6[W_6CCl_{18}]$ (II): A sample of 200 mg of the product mixture from reaction (1) was dissolved in 60 ml dimethyl sulfoxide (DMSO) and ethanol. After evaporation of the solvents at room temperature, dark brown needles and light green, transparent plate-like crystals were obtained. Needle shaped crystals of $Cu(C_2H_6OS)_6[W_6CCl_{18}]$ and plate shaped green crystals of $CuCl_2(C_2H_6OS)_2$ [78] shown in Figure 40 were identified.

$Cu(C_2H_6OS)_4[W_6CCl_{18}]_2$ (III): A sample of around 50 mg of $Cu(C_2H_6OS)_6[W_6CCl_{18}]$ was dissolved in 20 ml acetone. After evaporation of the solvents at room temperature, dark violet needles of $Cu(C_2H_6OS)_4[W_6CCl_{18}]_2$ and green crystals of $CuCl_2(C_2H_6OS)_2$ were obtained.

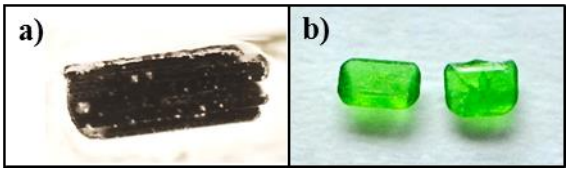

Figure 40. Crystals obtained during evaporation of dimethylsulfoxide: a) crystal of $Cu(C_2H_6OS)_6[W_6CCl_{18}]$, b) crystals of $CuCl_2(C_2H_6OS)_2$.

Characterization of $Cu[W_6CCl_{18}]$

Black block crystals of **1** crystallize triclinic in the space group *P-1* (Table 9) in comparison to the already known series of $A[W_6ZCl_{18}]$ compounds which were reported with the hexagonal in the space group $P6_3/m$[75]. The main motive in the crystal structure of **(I)** is the carbon-centered trigonal prismatic tungsten cluster anion $[W_6CCl_{18}]^-$. It is composed out of six tungsten atoms, which form a trigonal prism, centered with a carbon atom. Twelve chloride ligands have

μ_2-bridging functionality and six chlorides act as terminal Cl^a ligands, all together forming the $[(W_6CCl_{12})Cl_6]$ cluster presented in Figure 41.

Copper ions occupy two distinct positions in the structure with the statistical weight of ½ (refined occupancy 0.493(7) and 0.507(7)). Copper ions are tetrahedrally surrounded by chloride ligands of the $[W_6CCl_{18}]^-$ cluster. The tetrahedral environment of two adjacent copper ions yields edge-sharing bitetrahedra (Figure 41, right, top) might be compared with the arrangement of a $[Cu_2Cl_3]^-$fragment from the crystal structure of $[N(CH_3)_4][Cu_2Cl_3]$.[69] Interatomic distances of copper(I) ions in this compound are at 2.299(2) – 2.574(2) Å for Cu–Cl, and 2.869(2) – 3.197(2) Å for Cu–Cu distances. Corresponding distances in **(I)** range at 2.345(6) – 2.503(7) Å for Cu–Cl, and 2.59(1) – 2.66(1) Å Cu–Cu distances. Shorter Cu–Cu distance in **(I)** are due to the fact that copper positions in $Cu[W_6CCl_{18}]$ are only half occupied, and their alternative presence would avoid any Cu–Cu repulsion.

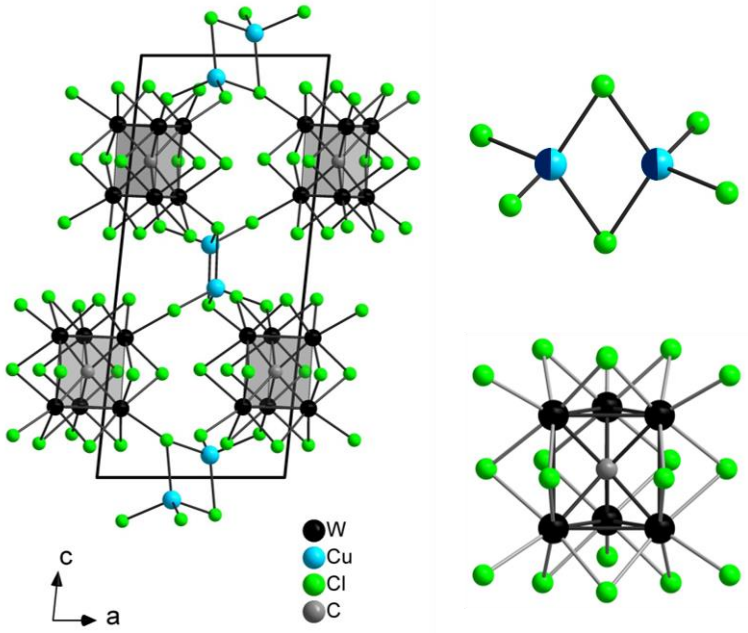

Figure 41. Crystal structure of $Cu[W_6CCl_{18}]$ (left) in which bridging chloride cluster ligands are removed for more clarity in the picture. A complete $[W_6CCl_{18}]$ cluster motive is shown at right, and the environment of copper (half occupied) is displayed in the central projection.

Table 9. Crystallographic data of $Cu[W_6CCl_{18}]$, $Cu(C_2H_6OS)_6[W_6CCl_{18}]$, and $[Cu(C_2H_6OS)_4][W_6CCl_{18}]_2$.

	I	**II**	**III**
Empirical formula	$Cu[W_6CCl_{18}]$	$Cu(C_2H_6OS)_6[W_6CCl_{18}]$	$Cu(C_2H_6OS)_4[W_6CCl_{18}]_2$
Formula weight / $g \cdot mol^{-1}$	1816.75	2285.52	3884.49
Crystal system	Triclinic	Monoclinic	Triclinic
Space group	P -1	C 2/c	P -1
Unit cell dimensions			
a / Å	8.89(1)	17.333(1)	9.471(1)
b / Å	8.929(1)	16.011(1)	12.630(2)
c / Å	17.669(2)	18.082(1)	13.634(2)
α / °	81.85(1)		104.69(1)
β / °	80.78(1)	94.61(1)	90.16(1)
γ / °	60.39(1)		92.99(1)
Volume / $Å^3$	1200.7(3)	5001.7(6)	1575.2(3)
Z	2	4	1
Density (calculated) / $g \cdot cm^{-3}$	5.025	3.035	4.095
Absorption coefficient / mm^{-1}	31.481	15.398	23.818
F(000)	1570	4148	1711
Crystal size / mm^3	0.26 x 0.14 x 0.14	0.05 x 0.15 x 0.41	0.10 x 0.16 x 0.34
Temperature / K	293(2)	293(2)	293(2)
Theta range for date collection / °	2.342 – 25.024	2.358 – 25.026	2.630 – 25.027
Total number of reflections	9524	19122	10225
Refined parameters	245	228	314
Goodness-of-fit on F^2	1.237	1.168	1.241
Final R indices [$I > 2\sigma(I)$]	$R_1 = 0.0369$, $wR_2 = 0.0845$	$R_1 = 0.0358$, $wR_2 = 0.0504$	$R_1 = 0.0347$, $wR_2 = 0.0644$
R indices (all data)	$R_1 = 0.0395$, $wR_2 = 0.0857$	$R_1 = 0.0529$, $wR_2 = 0.0544$	$R_1 = 0.0472$, $wR_2 = 0.0678$
Largest diff. peak and hole / $e \cdot Å^{-3}$	3.740 and -1.486	0.661 and -0.815	1.168 and -0.999

If copper was present as Cu^+ ions in **(I)** a corresponding $[W_6CCl_{18}]^-$ cluster anion should be present. The oxidation states of $[W_6CCl_{18}]^{n-}$ (n = 0, 1, 2) clusters are not always well expressed by bond distances, but they give a clear hint in this case. A comparison of W–W distances is shown in Table 11. Distances within the trigonal prismatic clusters can be subdivided into those running along trigonal edges and those connecting two triangles with each other. W–W distances within triangles of **(I)** range at 2.7150(8)–2.7450(1) Å and distances between two triangles are at 2.9117(9)–2.9350(9) Å. Average values of these distances are in good agreement

with distances obtained for $Li[W_6CCl_{18}]$, supporting the presence of a $[W_6CCl_{18}]^-$ cluster. For compounds containing a $[W_6CCl_{18}]^{2-}$ cluster smaller distances are expected along triangular edges.

Table 10. Average distances (Å) between tungsten atoms in $[W_6CCl_{18}]^{n-}$ anions of (I-III) in comparison to some other compounds.

	W-W $^{\Delta}$ / Å [a)]	W-W $^{\mid}$ / Å [b)]
$Cu[W_6CCl_{18}]$ **(I)**	2.7298(8)	2.9241(9)
$Cu(C_2H_6OS)_6[W_6CCl_{18}]$ **(II)**	2.6701(5)	3.0208(6)
$Cu(C_2H_6OS)_4[W_6CCl_{18}]_2$ **(III)**	2.7371(3)	2.9293(3)
W_6CCl_{18}[9]	2.743(1)	2.930(1)
$Li[W_6CCl_{18}]$[75]	2.7312(5)	2.9142(6)
$Ca[W_6NCl_{18}]$[75]	2.665(2)	3.013(2)
$(Bu_4N)_2[W_6CCl_{18}]$[11]	2.667(1)	3.028(1)
$(Bu_4N)_2[W_6CCl_{12}(CF_3SO_3)_6]$[76]	2.632(2)	3.037(5)

a) Δ – edges of triangles in trigonal prismatic cluster

b) $\mid$ – edges between triangles in trigonal prismatic cluster

Characterization of $Cu(C_2H_6OS)_6[W_6CCl_{18}]$

Dark brown, needles of $Cu(C_2H_6OS)_6[W_6CCl_{18}]$ crystallize monoclinic in the space group *C2/c* (Figure 40). The crystal structure contains carbon-centered trigonal prismatic tungsten cluster anions $[W_6CCl_{18}]^{2-}$ and copper complexes $[Cu(C_2H_6OS)_6]^{2+}$, where Cu ions are surrounded by a six dimethyl sulfoxide groups (Figure 42, bottom). The arrangement of $[W_6CCl_{18}]^{2-}$ clusters and $[Cu(C_2H_6OS)_6]^{2+}$ ions in the structure build up an arrangement similar to that in the CsCl structure, where complex copper ions are surrounded by eight clusters, and vice versa. Copper ions are surrounded by six dimethyl sulfoxide groups in a Jahn-Teller distorted octahedral fashion shown in Figure 42.[79,80] Bond lengths between copper and oxygen atoms presented in Table 12 reveal four shorter contacts with O1, O2 (1.939(6)-2.010(7) Å) and two longer ones with O3 (2.399(7) Å). All interatomic Cu-O distances are very similar to those found in $[Cu(C_2H_6OS)_6](HSO_4)_2$, where Cu^{2+} ions have a similar environment with six DMSO molecules.[81]

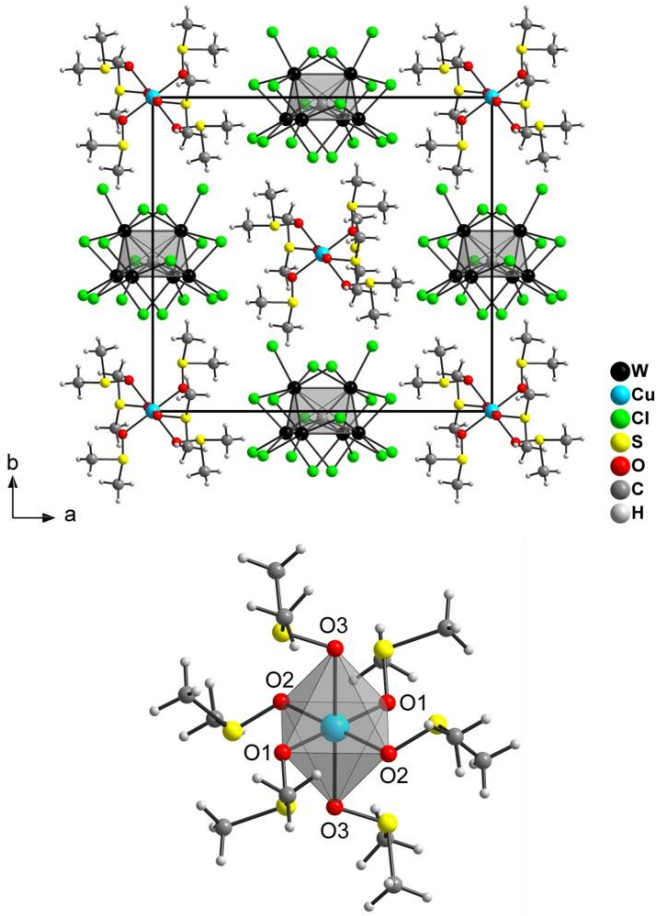

Figure 42. Cristal structures of $Cu(C_2H_6OS)_6[W_6CCl_{18}]$ (top), an octahedral copper(II) complex (bottom) and one of prototypical Jahn-Teller distortion of an octahedral copper(II) complex.

^{13}C-NMR measurement presented in Figure 43 proofs the presence of a carbon atom in the interstitial site of the trigonal prismatic cluster. The obtained chemical shift of 280.7 ppm for carbon a carbon atom is very similar for the corresponding signal found at 279.9 ppm for W_6CCl_{18}.[9,75] Carbon centered trigonal prismatic tungsten clusters of **(I)** and **(II)** appear similar although they show slightly different dimensions. W–W distances in **(II)** appear significantly shorter, and can be well related with other compounds listed in Table 10, containing divalent clusters ($[W_6CCl_{18}]^{2-}$).

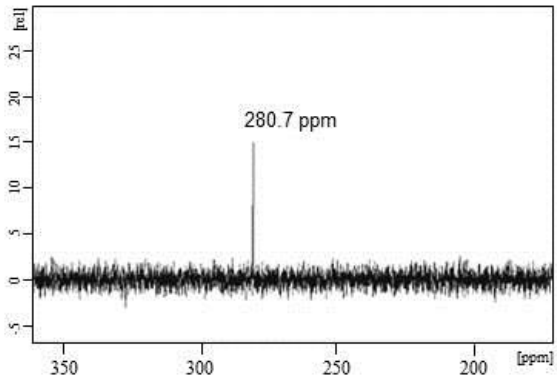

Figure 43. ^{13}C-NMR spectrum of $Cu(C_2H_6OS)_6[W_6CCl_{18}]$ cluster performed in DMSO.

Table 11. Selcted bond lengths (Å) of copper ions (multiplicities) for compounds (II, III) in comparison to bond lengths (Å) in other Cu^{2+} compounds.

	II	$[Cu(C_2H_6OS)_6](HSO_4)_2$ [81]	**III**	$[CuCl_6]^{4-}$ [82]
Cu – O1	1.939(6) (2x)	1.976(1) (2x)	1.94(1) (2x)	----
Cu – O2	2.010(7) (2x)	2.022(1) (2x)	1.918(9) (2x)	----
Cu – O3	2.399(7) (2x)	2.344(1) (2x)	----	----
Cu – Cl	----	----	3.011(4) (2x)	3.105(1) (2x)
Cu – Cl	----	----	----	2.251(1) (2x)
Cu – Cl	----	----	----	2.361(1) (2x)

II – $Cu(C_2H_6OS)_6[W_6CCl_{18}]$

III – $Cu(C_2H_6OS)_4[W_6CCl_{18}]_2$

Characterization of $Cu(C_2H_6OS)_4[W_6CCl_{18}]_2$

Dark violet, plate-shaped crystals of $Cu(C_2H_6OS)_4[W_6CCl_{18}]_2$ were crystallized after dissolving $Cu(C_2H_6OS)_6[W_6CCl_{18}]$ in acetone. The triclinic unit cell of **(III)** contains two carbon-centered trigonal prismatic tungsten cluster anions $[W_6CCl_{18}]^-$ and one Cu^{2+} ion. Copper is surrounded by four dimethyl sulfoxide groups ($[Cu(C_2H_6OS)_4]^{2+}$) in a nearly square planar arrangement and two axial chloride ligands of two clusters (Figure 44, bottom). The bridging connectivity

via chloride ions combines both structure elements into one and introduces a completely different structural arrangement.

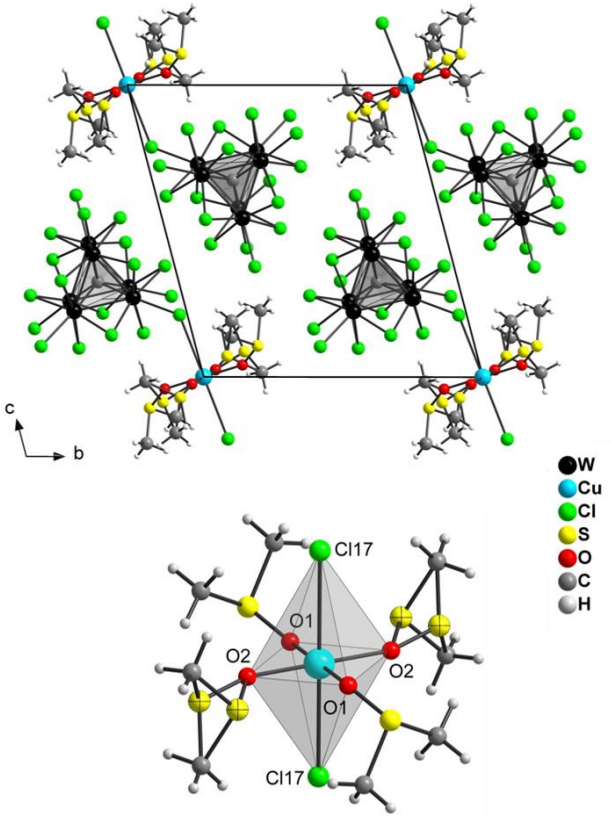

Figure 44. Cristal structures of $Cu(C_2H_6OS)_4[W_6CCl_{18}]$ (top) and an octahedral Jahn-Teller distortions of copper(II) complex (bottom). On the right side copper core, from $Cu(C_2H_6OS)_4\,[W_6CCl_{18}]$ compound, coordinated six fold with four oxygen atoms and two chloric atoms.

W–W bond lengths within the carbon-centered trigonal prismatic tungsten cluster of **(III)** are in good agreement with the assumption of a $[W_6CCl_{18}]^-$ cluster in **(I)** (Table 10). Distances between copper and surrounding atoms are presented in Table 11.

Summary

With the DSC monitoring approach for reactions between tungsten hexachloride and elemental manganese, iron, cobalt, nickel or copper binary W-Cl and ternary M-W-Cl systems were successfully explored. A whole series of compounds can be harvested by separate preparation at temperatures corresponding to those of thermal effect observed in the DSC diagram.

Thermal scanning of the Mn-W-Cl system with excess of manganese powder has shown the formation conditions of four new compounds Mn_xWCl_6, MnW_2Cl_{10}, $(Mn,W)_{1-x}Cl_2$, and MnW_6Cl_{14}.

The reaction begins with an intercalation of manganese ions into the structure of α-WCl_6, represented by close packed layers of chloride ions in which tungsten ions occupy (1/3) octahedral sites in every other interlayer. Only a small fraction (< 1/10) of vacant octahedral voids in these layers is considered to be occupied by manganese ions. After the first reduction step more manganese is incorporated into the structure of MnW_2Cl_{10}. In this structure cations occupy 1/5 (Mn) + 2/5 (W) octahedral sites in every second interlayer. Two tungsten ions are forming edge-sharing bioctahedral $[W_2Cl_{10}]^{2-}$ units. The next compound in the reaction sequence is $(Mn,W)_{1-x}Cl_2$, having a crystal structure related to that of $MnCl_2$ ($CdCl_2$-type), however with a 10 % smaller unit cell volume. The last reduction step in Mn-W-Cl system formation leads to MnW_6Cl_{14} compound. Tungsten atoms are building octahedral cluster cores which requires a major rearrangement of atoms, losing the layered arrangement of the structure. Manganese cations are octahedrally connected with six terminal chloride ions belonging to $[W_6Cl_{14}]$ cluster.

MnW_2Cl_{10} and MnW_6Cl_{14} show paramagnetic behavior.

The next metal from d-group elements used in the reduction of WCl_6 is iron. The reduction of β-WCl_6 with a sufficient amount of iron powder involves the cascade of five new compounds Fe_xWCl_6, FeW_2Cl_{10}, $Fe_2W_2Cl_{10}$, $(Fe,W)_{1-x}Cl_2$, and FeW_6Cl_{14}.

According to X-ray structure determination performed on a single crystal of Fe_xWCl_6, the iron ions are occupying octahedral voids in the same layers that are occupied with tungsten ions in α-WCl_6. The iron content in the crystal structure of Fe_xWCl_6 was refined in the order of x = 0.08. The crystal structures of FeW_2Cl_{10}, and $Fe_2W_2Cl_{10}$ reflect successive steps of reductive intercalations of Fe ions into a W_2Cl_{10} (WCl_5) structure.

This reductive intercalation can be considered to require a minimum of energy in transformation from FeW_2Cl_{10} to $Fe_2W_2Cl_{10}$, because no fundamental structural reorganization is necessary. Both structures are layered structures, where iron cation occupy 1/5 and 2/5 of octahedral voids in every second interlayer.

Mössbauer studies clearly show that iron ions are present as Fe^{2+} in all compounds in the Fe-W-Cl series. Following these results, tungsten appears as $W^{5+/6+}$ in Fe_xWCl_6, W^{4+} in FeW_2Cl_{10}, W^{3+} in $Fe_2W_2Cl_{10}$ and in $(Fe,W)_{1-x}Cl_2$, and W^{2+} in FeW_6Cl_{14}.

FeW_2Cl_{10}, $(Fe,W)_{1-x}Cl_2$ and FeW_6Cl_{14} compounds show paramagnetic behavior.

The electronic structure calculations lead to the assumption, that the bonding between tungsten ions in edge-sharing $[W_2Cl_{10}]^{n-}$ bioctahedra can be characterized as a W^{4+}–W^{4+} interaction with a formal ($\sigma^2\pi^2$) double bond for FeW_2Cl_{10}. The situation of the W^{3+}–W^{3+} interaction in $Fe_2W_2Cl_{10}$ can be also assigned close to a double bond because the δ^2 situation appears nearly nonbonding, due to the equal occupation of δ and δ* levels with electrons.

The third metal chosen for the reduction of tungsten hexachloride is cobalt. The reaction of β-WCl_6 with a sufficient amount of cobalt powder results with a series of five new compounds: Co_xWCl_6, CoW_2Cl_{10}, "$Co_2W_2Cl_{10}$", $(Co,W)_{1-x}Cl_2$, and CoW_6Cl_{14}.

The first reduction step of β-WCl_6 with cobalt powder begins similar as in the other two systems, with the intercalation of cobalt cations to yield Co_xWCl_6. The structure has a layered arrangement consistent with a stuffed α-WCl_6-type structure. The crystal structure of Co_xWCl_6 can be refined isotypic with these for the iron and manganese compounds. It can be observed, that with the decreasing ionic radius of metals Mn, Fe, and Co (oxidation state 2+, IR_{Mn} = pm, IR_{Fe} = 92 pm and IR_{Co} = 88.5 pm), the unit cell volume decreases from V = 573.3(2) Å^3 for Mn_xWCl_6, to V = 557.5(3) Å^3 for Fe_xWCl_6 and to V = 553.4(2) Å^3 for Co_xWCl_6.

The next two reductive intercalations of cobalt result with the formation of two compounds characterized as CoW_2Cl_{10} and ''$Co_2W_2Cl_{10}$''. Both structures are based on a hcp of chloride ions, where every second interlayer is successively occupied with cobalt ions. The corresponding reduction of tungsten is buffered by the uptake of electrons into the bonds between two tungsten atoms in $[W_2Cl_{10}]^{n-}$ bioctahedra. W–W dimers are capable to form double-bonds in CoW_2Cl_{10} and triple-bonds in ''$Co_2W_2Cl_{10}$''. The precise Co content in ''$Co_2W_2Cl_{10}$'' remains in question.

The structure of $(Co,W)_{1-x}Cl_2$ was indexed isotypically to the crystal structure of $CoCl_2$ ($CdCl_2$-type), with a significantly smaller unit cell of 13.6 Å^3 (≈ 7 %).
The last identified product is CoW_6Cl_{14}, the octahedral tungsten cluster with the structure isotypic to MW_6Cl_{14} in manganese and iron system.
For CoW_2Cl_{10}, $(Co,W)_{1-x}Cl_2$ and CoW_6Cl_{14} compounds paramagnetic behavior was found.

Reaction of β-WCl_6 with nickel, the fourth reducing metal of this series, results with only two compounds described as $(Ni,W)_{1-x}Cl_2$, and NiW_6Cl_{14}. The NiW_6Cl_{14} cluster is isotypic to other MW_6Cl_{14} (M = Mn, Fe, Co) compounds.
Nickel metal shows low reducing properties against tungsten hexachloride. $(Ni,W)_{1-x}Cl_2$ can be synthesized at temperature above 400 °C. The crystal structure according to the X-ray powder diffraction data seems to be isotypic to other $(M,W)_{1-x}Cl_2$ (M = Mn, Fe, Co) compounds. As expected also in the series of $(M,W)_{1-x}Cl_2$ products, the unit cell volume decreases with decreasing ionic radius of M^{2+} (IR_{Mn} = 97 pm, IR_{Fe} = 92 pm, IR_{Co} = 88.5 pm, IR_{Ni} = 83 pm) following the sequence V = 183.12(5) Å^3 > 180.23(4) Å^3 > 176.1(7) Å^3 > 173.74(1) Å^3. The stability of the products against moist air decreases in the opposite way, from few minutes for the manganese compound, to a minimum of a few months for the nickel compound. The defect $CdCl_2$-type structure of $(Ni,W)_{1-x}Cl_2$ compound could not be refined, due to the possible presence of a super-structure.

The last element used in this reduction studies is copper. The successive reduction of WCl_6 with copper powder shows up the reductive intercalation of copper ions to yield six new products: α-Cu_xWCl_6, β-Cu_xWCl_6, γ-Cu_xWCl_6, α-$Cu_2W_2Cl_{10}$, β-$Cu_2W_2Cl_{10}$, and $Cu_2W_6Cl_{14}$.
The reaction of β-WCl_6 with elemental copper begins at temperatures below 60 °C to form α-Cu_xWCl_6. Continuing reaction stages include the compounds β-Cu_xWCl_6, γ-Cu_xWCl_6. Crystal structures of Cu_xWCl_6 phases are based on hcp of chloride ions in which tungsten ions occupy 1/6 of the octahedral voids. Copper ions are disordered over a few position with partial occupations.
Further reduction step requires rearrangement of tungsten ions within octahedral layers and yields with $[W_2Cl_{10}]^{2-}$ bioctahedra with a metal–metal bonding between tungsten atoms, occurring as α- and β-modification of $Cu_2W_2Cl_{10}$. Both structures are based on an hcp of chloride ions. In α-$Cu_2W_2Cl_{10}$ copper ions are situated in distorted trigonal planar surrounding

of chloride ions, while in β-$Cu_2W_2Cl_{10}$ copper ions are tetrahedrally surrounded with four chloride ions.

A final reconstructive step leads to the formation of $Cu_2W_6Cl_{14}$ containing an octahedral tungsten cluster. All products in Cu-W-Cl system behave sensitive to moist air except for $Cu_2W_6Cl_{14}$.

More metastable phases may be expected to exist in this system.

A solid state reaction between β-WCl_6, copper powder, and C_6Cl_6 leads to the new carbon-centered trigonal prismatic tungsten cluster $Cu[W_6CCl_{18}]$ containing Cu^+ and $[W_6CCl_{18}]^-$. The tetrahedral environment of two neighboring copper ions forms the motive of edge-sharing bitetrahedra $[Cu_2Cl_6]$.

Dissolution of $Cu[W_6CCl_{18}]$ in DMSO yields $[Cu(C_2H_6OS)_6][W_6CCl_{18}]$ in which Cu^{2+} is situated in a Jahn-Teller distorted octahedron in surrounded by six dimethyl sulfoxide groups, and the $[W_6CCl_{18}]^{2-}$. The oxidation state of $[W_6CCl_{18}]^{n-}$ may be estimated by marginal changes in trigonal prismatic cluster dimensions, i.e. by a contraction of trigonal faces and an extension of prismatic edges when going from n = 1 to 2, and vice versa. $[Cu(C_2H_6OS)_6][W_6CCl_{18}]$ can be transformed into $[Cu(C_2H_6OS)_4][W_6CCl_{18}]_2$ cluster.

Reduction of WCl_6 with non-classical reduction agents such as Mn, Fe, Co, Ni und Cu have a big potential. The thermal detection method is showing promising results for systematically explorations in the field of metal halides with respect to structural reorganizations. As a result of studies in the M-W-Cl systems it could be shown that a significant number of thermally metastable compounds is existing. It turned out, that performed reduction studies involve a cascade of intermediate compounds until a thermodynamically stable product is formed. It can be noted, that several of these compounds exist only in a small temperature window. Therefore it is very difficult to find such compounds in explorative solid state reactions, without results from DSC measurements. In addition, this procedure may be expanded to other metal halide systems[83] and other reducing agents adapted from the entire periodic system. This type of investigation opens a new window for the detection and controlled synthesis of new cluster compounds.

Zusammenfassung

Durch die Untersuchung der Reduktion zwischen Wolframhexachlorid und elementarem Mangan, Eisen, Cobalt, Nickel oder Kupfer konnten binäre W-Cl und ternäre M-W-Cl Systeme erfolgreich untersucht werden. Es konnte eine ganze Serie von neuen Verbindungen durch die Kombination von DSC und einzeln durchgeführten Reaktionen erhalten werden.

Die thermische Analyse des Mn-W-Cl-Systems mit einem Überschuss an Manganpulver zeigt die Bildungsbedingungen von vier neuen Verbindungen: Mn_xWCl_6, MnW_2Cl_{10}, $(Mn,W)_{1-x}Cl_2$ und MnW_6Cl_{14}.
Die Reaktion beginnt mit einer Interkalation von Mangan-Ionen in die Struktur von α-WCl_6, die aus einer hdp von Chlorid-Ionen besteht, in der Wolfram-Ionen 1/3 der oktaedrischen Plätze in jeder zweiten Schicht besetzen. Es wird angenommen, dass nur ein kleiner Bruchteil (< 1/10) der freien Oktaederlücken in diesen Schichten durch Mangan-Ionen besetzt wird. Nach dem ersten Reduktionsschritt wird mehr Mangan in die Struktur von MnW_2Cl_{10} aufgenommen. In dieser Struktur besetzen Kationen 1/5 (Mn) + 2/5 (W) der oktaedrischen Lücken in jeder zweiten Zwischenschicht. Wolfram-Ionen bilden hierbei kantenverknüpfte, bioktaedrische $[W_2Cl_{10}]^{2-}$-Einheiten. Die nächste Verbindung in der Reaktionssequenz ist $(Mn,W)_{1-x}Cl_2$ mit einer Kristallstruktur verwandt zu der von $MnCl_2$ ($CdCl_2$-Typ), jedoch mit einer 10 % kleineren Elementarzelle. Der letzte Reduktionsschritt im System von Mn-W-Cl führt zu der Verbindung MnW_6Cl_{14}. Die Bildung dieser Verbindung ist mit einer drastischen Restrukturierung der Atome verbunden, wobei sowohl die dichteste Kugelpackung als auch die schichtartige Struktur verloren gehen. Mangan-Ionen sind oktaedrisch mit sechs terminalen Chlorid-Ionen verbunden, die jeweils zu einem $[W_6Cl_{14}]^{2-}$-Cluster gehören.
Für MnW_2Cl_{10} und MnW_6Cl_{14} wurde paramagnetisches Verhalten gefunden.

Das nächste Metall der d-Gruppen-Elemente, das für die Reduktion von WCl_6 verwendet wurde, ist Eisen. Die Reduktion von β-WCl_6 mit einer ausreichenden Menge Eisenpulver führt zu einer Kaskade von fünf neuen Verbindungen Fe_xWCl_6, FeW_2Cl_{10}, $Fe_2W_2Cl_{10}$, $(Fe,W)_{1-x}Cl_2$ und FeW_6Cl_{14}.
Gemäß der Röntgenstrukturbestimmung an einem Fe_xWCl_6-Einkristall besetzen die Eisen-Ionen oktaedrische Lücken in denselben Schichten wie die Wolfram-Ionen. Der Eisengehalt in der Kristallstruktur von Fe_xWCl_6 wurde in der Größenordnung von x = 0,08 verfeinert. Die Kristallstrukturen von FeW_2Cl_{10} und $Fe_2W_2Cl_{10}$ zeigen aufeinanderfolgende Schritte einer

Interkalation von Eisen-Ionen in eine W_2Cl_{10} (WCl_5) Struktur. Es kann in Betracht gezogen werden, dass diese reduktive Interkalation ein Minimum an Energie für die Umwandlung von FeW_2Cl_{10} zu $Fe_2W_2Cl_{10}$ braucht, da keine fundamentale Reorganisation der Struktur vonnöten ist. Beide Strukturen sind Schichtstrukturen, wobei Eisen-Ionen 1/5 beziehungsweise 2/5 der oktaedrischen Lücken in jeder zweiten Schicht besetzen.

Mössbauer-Messungen zeigen deutlich, dass Eisen-Ionen als Fe^{2+} in allen Verbindungen der Fe-W-Cl Serie vorhanden sind. Fasst man all diese Ergebnisse zusammen, so zeigt sich Wolfram als $W^{5+/6+}$ in Fe_xWCl_6, als W^{4+} in FeW_2Cl_{10}, als W^{3+} in $Fe_2W_2Cl_{10}$ und $(Fe,W)_{1-x}Cl_2$, und als W^{2+} in FeW_6Cl_{14}.

Für FeW_2Cl_{10}, $(Fe,W)_{1-x}Cl_2$ und FeW_6Cl_{14} wurde paramagnetisches Verhalten gefunden.

Die Berechnungen der elektronischen Struktur führen zu der Annahme, dass die Bindungen zwischen den Wolfram-Ionen in den kantenverknüpften $[W_2Cl_{10}]^{n-}$ Bioktaedern als W^{4+}-W^{4+} Wechselwirkungen mit einer formalen ($\sigma^2\pi^2$) Doppelbindung für FeW_2Cl_{10} beschrieben werden können. Die Situation der W^{3+}-W^{3+}-Wechselwirkung in $Fe_2W_2Cl_{10}$ kann ebenfalls beinahe als Doppelbindung aufgefasst werden, da die δ^2 Situation nahezu, durch die gleiche Besetzung von δ und δ^* mit Elektronen, nichtbindend erscheint.

Das dritte Metall, das für die Reduktion von Wolframhexachlorid ausgewählt wurde, ist Cobalt. Die Reaktion von β-WCl_6 mit einer ausreichenden Menge an Cobaltpulver führt zu einer Serie von fünf neuen Verbindungen: Co_xWCl_6, CoW_2Cl_{10}, "$Co_2W_2Cl_{10}$", $(Co,W)_{1-x}Cl_2$ und CoW_6Cl_{14}.

Der erste Reduktionsschritt von β-WCl_6 mit Cobaltpulver beginnt mit der Bildung von Co_xWCl_6. Die Struktur hat eine Schichtanordnung ähnlich zur aufgefüllten α-WCl_6 Struktur. Die Kristallstruktur von Co_xWCl_6 kann isotyp zu der Eisen- und Manganverbindung verfeinert werden. Es kann beobachtet werden, dass mit dem abnehmenden Ionenradius (IR) der Metalle Mn, Fe, und Co (Oxidationsstufe 2+, IR_{Mn} = pm, IR_{Fe} = 92 pm und IR_{Co} = 88.5 pm) das Zellvolumen abnimmt und V = 573.3(2) $Å^3$ für Mn_xWCl_6, V = 557.5(3) $Å^3$ für Fe_xWCl_6 und V = 553.4(2) $Å^3$ für Co_xWCl_6 beträgt.

Die nächsten zwei reduktiven Interkalationen von Cobalt resultieren in der Bildung zweier Verbindungen, welche als CoW_2Cl_{10} und "$Co_2W_2Cl_{10}$" charakterisiert werden konnten. Beide Strukturen basieren auf einer hexagonal dichtesten Kugelpackung von Chlorid-Ionen, wobei jede zweite Oktaederlückenschicht zu 1/5 beziehungsweise 2/5 mit Cobalt-Ionen besetzt ist. Die entsprechende Reduktion mit Cobalt geht mit der Aufnahme von Elektronen in die Bindung

zwischen zwei Wolframatomen in den $[W_2Cl_{10}]^{n-}$ Bioktaeder einher. Die $[W_2Cl_{10}]^{n-}$ Bioktaedern sind in der Lage Doppelbindungen in CoW_2Cl_{10} und Dreifachbindungen in "$Co_2W_2Cl_{10}$" auszubilden. Der genaue Cobaltgehalt von "$Co_2W_2Cl_{10}$" konnte nicht abschließend geklärt werden.

Die Struktur von $(Co,W)_{1-x}Cl_2$ wurde isotyp zu der Kristallstruktur von $CoCl_2$ ($CdCl_2$-Typ) indiziert, jedoch mit einer signifikant kleineren Elementarzelle von 13,6 $Å^3$ (≈ 7 %). Das letzte identifizierte Produkt ist CoW_6Cl_{14}, ein oktaedrischer Wolframcluster mit einer Struktur isotyp zu MW_6Cl_{14} im Mangan- und Eisensystem.

CoW_2Cl_{10}, $(Co,W)_{1-x}Cl_2$ und CoW_6Cl_{14} zeigen ein paramagnetisches Verhalten.

Reaktionen von β-WCl_6 mit Nickel, dem vierten reduzierenden Metall der Serie, resultieren in nur zwei Verbindungen, die beschrieben werden können als $(Ni,W)_{1-x}Cl_2$ und NiW_6Cl_{14}. Der Cluster NiW_6Cl_{14} ist isotyp zu anderen MW_6Cl_{14} (M = Mn, Fe, Co) Verbindungen.

Nickel zeigt geringe reduzierende Eigenschaften mit Wolframhexachlorid. $(Ni,W)_{1-x}Cl_2$ kann bei Temperaturen über 400 °C synthetisiert werden. Die Kristallstruktur scheint, gemäß der Röntgenstrukturbestimmung, isotyp zu anderen $(M,W)_{1-x}Cl_2$ (M = Mn, Fe, Co) Verbindungen zu sein. Wie es auch in der Serie der $(M,W)_{1-x}Cl_2$ Verbindungen zu erwarten ist, nimmt die Größe der Elementarzelle mit abnehmendem Ionenradius der M^{2+}-Ionen (IR_{Mn} = 97 pm, IR_{Fe} = 92 pm, IR_{Co} = 88.5 pm, IR_{Ni} = 83 pm) ab und beträgt V = 183.12(5) $Å^3$ > 180.23(4) $Å^3$ > 176.1(7) $Å^3$ > 173.74(1) $Å^3$. Die Stabilität der Produkte gegenüber Luftfeuchtigkeit nimmt in umgekehrter Reihenfolge ab, von ein paar Minuten für die Manganverbindung bis zu ein paar Monaten für die Nickelverbindung. Es war nicht möglich den $CdCl_2$-Defektstrukturtyp von $(Ni,W)_{1-x}Cl_2$ zu verfeinern, möglicherweise liegt eine Überstruktur vor.

Das letzte Element, das in dieser Reduktionsstudie verwendet wird, ist Kupfer. Die sukzessive Reduktion von WCl_6 mit Kupferpulver zeigt eine reduktive Interkalation von Kupfer-Ionen und es werden sechs neue Produkte erhalten: α-Cu_xWCl_6, β-Cu_xWCl_6, γ-Cu_xWCl_6, α-$Cu_2W_2Cl_{10}$, β-$Cu_2W_2Cl_{10}$, und $Cu_2W_6Cl_{14}$.

Die Reaktion von β-WCl_6 mit elementarem Kupfer beginnt schon bei Temperaturen unter 60 °C und es wird α-Cu_xWCl_6 gebildet. Weiterführende Reaktionsstufen beinhalten die Verbindungen β-Cu_xWCl_6 und γ-Cu_xWCl_6. Kristallstrukturen der Cu_xWCl_6 Phasen basieren auf einer hexagonal dichtesten Packung von Chlorid-Ionen in welchen Wolfram-Ionen 1/6 der oktaedrischen Lücken besetzen. Kupfer-Ionen sind über wenige oktaedrischen Lücken mit partieller Besetzung verteilt.

Der nächste beobachtete Reduktionsschritt erfordert eine Neuorientierung der Wolfram-Ionen innerhalb der oktaedrischen Schichten und führt zu $[W_2Cl_{10}]^{2-}$ Bioktaedern mit einer Metall-Metall-Bindung zwischen den Wolfram-Atomen, was in den α- und β-Modifikationen von $Cu_2W_2Cl_{10}$ endet. Beide Strukturen basieren auf einer hexagonal dichtesten Packung von Chlorid-Ionen. In α-$Cu_2W_2Cl_{10}$ ist Kupfer verzerrt trigonal planar von Chlorid-Ionen umgeben, während in β-$Cu_2W_2Cl_{10}$ die Kupfer-Ionen tetraedrisch von vier Chlorid-Ionen umgeben sind. Ein letzter rekonstruktiver Schritt führt zu der Bildung von $Cu_2W_6Cl_{14}$, das einen oktaedrischen Wolfram-Cluster enthält. Alle Produkte im Cu-W-Cl-System verhalten sich empfindlich gegenüber Luftfeuchtigkeit mit Ausnahme von $Cu_2W_6Cl_{14}$.
Es kann davon ausgegangen werden, dass noch mehrere metastabile Phasen in diesem System existieren.

Die Festkörperreaktion zwischen β-WCl_6, Kupferpulver und C_6Cl_6 führt zum neuen kohlenstoffzentrierten trigonal-prismatischen Cluster $Cu[W_6CCl_{18}]$ welcher Cu^+ und $[W_6CCl_{18}]^-$ enthält. Die tetraedrische Umgebung zweier benachbarter Kupfer-Ionen formt das Motiv von kantenverknüpften $[Cu_2Cl_6]$ Bitetraedern. Das Auflösen von $Cu[W_6CCl_{18}]$ in DMSO führt zur Bildung von $[Cu(C_2H_6OS)_6][W_6CCl_{18}]$ wobei Jahn-Teller verzerrte Cu^{2+}-Ionen von sechs Dimethylsulfoxid Gruppen und $[W_6CCl_{18}]^{2-}$-Clustern umgeben sind. Die Oxidationsstufe von $[W_6CCl_{18}]^{n-}$ kann durch eine marginale Verschiebung in den trigonal-prismatischen Cluster-Dimensionen abgeschätzt werden, d. h. eine Kontraktion der trigonalen Flächen und eine Erweiterung der prismatischen Kanten, ausgehend von n = 1 zu 2 und umgekehrt.
$[Cu(C_2H_6OS)_6][W_6CCl_{18}]$ kann in den Cluster $[Cu(C_2H_6OS)_4][W_6CCl_{18}]_2$ überführt werden.

Die Untersuchung der Reduktion von WCl_6 mit nicht klassischen Reduktionsmittel wie Mn, Fe, Co, Ni und Cu zeigt großes Potential. Die thermische Analyse zeigt vielversprechende Resultate zur systematischen Untersuchungen auf dem Gebiet der Metallhalogenide hinsichtlich der strukturellen Reorganisation. Zusammenfassend konnte in den Studien der M-W-Cl Systeme gezeigt werden, dass eine signifikante Anzahl von thermisch metastabilen Verbindungen existiert. Diese Studien zeigen, dass bei der Reduktion eine Kaskade von Zwischenverbindungen entsteht bis ein thermodynamisch stabiles Produkt gebildet wird. Metastabile Verbindungen werden in explorativen Festkörper-Reaktionen ohne Hilfe von DSC-Messungen oftmals übersehen. Dieses Verfahren kann möglicherweise auf andere Metallhalogen-Systeme[83] und andere Reduktionsmittel des ganzen Periodensystems übertragen werden.

List of Publications

1. Cluster Harvesting by Successive Reduction of a Metal Halide with a Nonconventional Reduction Agent - a Benefit for the Exploration of Metal-Rich Halide Systems.
   M. Ströbele, A. Mos, H.-J. Meyer, *Inorg. Chem.* **2013**, *52*, 6951–6956.

2. Thermal Detection, Synthesis, and Structural Characterization of Compounds in the Co-W-Cl System.
   A. Mos, M. Ströbele, H.-J. Meyer, *J. Cluster Sci.* **2015**, *26*, 187-198.

3. Detection and Characterization of Compounds in the Mn-W-Cl System through a Combined Thermal Scanning-XRD Approach.
   A. Mos, M. Ströbele, H.-J. Meyer, *Z. Anorg. Allg. Chem.* **2015**, 641, 1722-1727.

4. Carbon Centered Trigonal Prismatic Tungsten Clusters $[W_6CCl_{18}]^{n-}$ (n = 1, 2) containing Copper(I) and Copper(II).
   A. Mos, M. Ströbele, H.-J. Meyer, *Z. Anorg. Allg. Chem.* **2015**, *641*, 2245-2249.

5. From WCl_6 to WCl_2. Properties of Intermediate Fe-W-Cl Phases.
   A. Mos, C. Castro, S. Indris, M. Ströbele, R. F. Fink, H.-J. Meyer, *Inorg. Chem*. **2015**, *54*, 9826-9832.

6. Snap-shots of a Reduction Pathway: The Reaction of WCl_6 with Copper Powder.
   A. Mos-Hummel, M. Ströbele, H.-J. Meyer, *Eur. J. Inorg. Chem*. **2016**,
   DOI: 10.1002/ejic.201600640.

Acknowledgment

I would like to take the opportunity to thank all those who contributed in accomplishing this research.

Dr. Markus Ströbele for support in the field of crystallography.

Dr. Jochen Glaser for preforming and evaluating of magnetic measurements.

Dr. Sylvio Indris from Karlsruhe Institute of Technology for performing of Mössbauer spectroscopy measurements and their evaluation.

Prof. Dr. R. F. Fink and Cristina Castro for performing of quantum chemical calculations.

Elke Nadler for the help with performing of EDX measurements.

Dr. Ronny Löffler for crystal pictures done with a Scanning Electron Microscope.

At last, I would like to thank Dr. Farzia Hossain for performing of a NMR measurement.

References

[1] J. A. A. Ketelaar, G. W. van Oosterhout, *Recl. Trav. Chim. Pays-Bas*, **1943**, *62*, 197–200.

[2] F. Tamadon, K. Seppelt, *Angew. Chem. Int. Ed.* **2013**, *52*, 767–769.

[3] J. C. Taylor, P. W. Wilson, *Acta Cryst. Sect. B,* **1974**, *30*, 1216–1220.

[4] F. A. Cotton, C. E. Rice, *Acta Cryst. Sect. B,* **1978**, *34*, 2833–2834.

[5] A. Nägele, Dissertation, Univ. Tübingen, Germany, **2001**.

[6] V. Kolesnichenko, D. C. Swenson, L. Messerle, *Inorg. Chem.* **1998**, *37*, 3257–3262.

[7] R. E. McCarley, T. M. Brown, *Inorg. Chem.* **1964**, *3*, 1232–1236; R. D. Hogue, R. E. McCarley, *Inorg. Chem.* **1970**, *9*, 1354–1360; T. C. Zietlow, M. D. Hopkins, H. B. Gray, *J. Solid State Chem.* **1985**, *59*, 112–119; V. Kolesnichenko, L. Messerle, *Inorg. Chem.* **1998**, *37*, 3660–3663; M. Ströbele, T. Jüstel, H. Bettentrup, H.-J. Meyer, *Z. Anorg. Allg. Chem.* **2009**, *635*, 822–827.

[8] R . Siepmann, H.-G. v. Schnering, H. Schäfer, *Angew. Chem.* **1967**, *79*, 650–651; A. Nägele, J. Glaser, H.-J. Meyer, *Z. Anorg. Allg. Chem.* **2001**, *627*, 244–249; S. Dill, J. Glaser, M. Ströbele, S. Tragl, H.-J. Meyer, *Z. Anorg. Allg. Chem.* **2004**, *630*, 987–992.

[9] Y.-Q. Zheng, H. G. von Schnering, J.-H. Chang, Y. Grin, G. Engelhardt, G. Heckmann, *Z. Anorg. Allg. Chem.* **2003**, *629*, 1256–1264.

[10] M. Ströbele, H.-J. Meyer, *Inorg. Chem.* **2010**, *49*, 5986–5991.

[11] E. J. Welch, N. R. M. Crawford, R. G. Bergman, J. R. Long, *J. Am. Chem. Soc.* **2003**, *125*, 11464–11465.

[12] E. J. Welch, C. L. Yu, N. R. M. Crawford, J. R. Long, *Angew. Chem.* **2005**, *117*, 2605–2609; *Int. Ed.* **2005**, 44, 2549–2553.

[13] K. Jödden, H. Schäfer, *Z. Anorg. Allg. Chem.* **1977**, *430*, 5-22.

[14] E. Ahmed, M. Groh, M. Ruck, *Eur. J. Inorg. Chem.* **2010**, *33*, 5294-5297.

[15] SMART, SAINT, SADABS, and XPREP: Area Detector Control and Data Integration and Reduction Software, Bruker Analytical X-ray Instruments Inc., Madison.

[16] T. Roisnel, J. Rodriguez-Carvajal, WinPLOTR: A Windows tool for powder diffraction patterns analysis. Proceedings of the Seventh European Powder Diffraction Conference (EPDIC7), R. Delhez, E. J. Mittenmeijer, Eds.; Barcelona, Spain, May 20−23, **2000**, *Vol. 118*.

[17] A. Altomare, M. Camalli, C. Cuocci, C. Giacovazzo, A. Moliterni, R. Rizzi, *J. Appl. Crystallogr.* **2009**, *42*, 1197–1202.

[18] G. M. Sheldrick, *SHELXL-97: Program Package for Crystal Structure Determination*, University of Göttingen, Göttingen, 1997.

[19] TURBOMOLE V6.6 2014, a development of the University of Karlsruhe and Forschungszentrum Karlsruhe GmbH, 1989-2007, TURBOMOLE GmbH, since **2007**; available from http://www.turbomole.com/.

[20] R. Ahlrichs, M. Bär, M. Häser, H. Horn, C. Kölmel, *Chem. Phys. Lett.* **1989**, *162*, 165–169.

[21] A. D. Becke, *Phys. Rev. A*, **1988**, *38*, 3098–3100.

[22] O. Vahtras, J. Almlöf, M.W. Feyereisen, *Chem. Phys. Lett.* **1993,** *213*, 514–518.

[23] K. Eichkorn, F. Weigend, O. Treutler, R. Ahlrichs, *Theor. Chem. Acc.* **1997**, *97*, 119–124.

[24] M. von Arnim, R. Ahlrichs, *J. Comp. Chem.* **1998**, *19*, 1746–1757.

[25] M. Sierka, A. Hogekamp, R. Ahlrichs, *J. Chem. Phys.* **2003**, *118*, 9136–9148.

[26] F. Weigend, R. Ahlrichs, *Phys. Chem. Chem. Phys.* **2005**, *7*, 3297–3305.

[27] D. Andrae, U. Häußermann, M. Dolg, H. Stoll, H. Preuß, *Theor. Chim. Acta* **1990,** *77*, 123–141.

[28] A. Klamt, G. Schürmann, *J. Chem. Soc. Perkin Trans.* **1993**, *2*, 799–805.

[29] A. Klamt, *J. Phys. Chem.* **1996**, *100*, 3349–3353.

[30] A. Klamt, V. Jonas, *J. Chem. Phys.* **1996**, *105*, 9972–9981.

[31] P. Deglmann, F. Furche, R. Ahlrichs, *Chem. Phys. Lett.* **2002**, *362*, 511–518.

[32] A. Mos, M. Ströbele, H.-J. Meyer, *Z. Anorg. Allg. Chem.* **2015**, 641, 1722–1727.

[33] M. Ströbele, H.-J. Meyer, *Z. Anorg. Allg. Chem.* **2011**, *637*, 1024–1029.

[34] M. Ströbele, A. Mos, H.-J. Meyer, *Inorg. Chem.* **2013**, *52*, 6951–6956.

[35] A. Mos, C. Castro, S. Indris, M. Ströbele, R. F. Fink, H.-J. Meyer, *Inorg. Chem.* **2015**, *54*, 9826–9832.

[36] A. Mos, M. Ströbele, H.-J. Meyer, *J. Cluster Sci*. **2015**, *26*, 187–198.

[37] A. Mos-Hummel, M. Ströbele, H.-J. Meyer, *Eur. J. Inorg. Chem*. **2016**, published online.

[38] S. Böschen, H. L. Keller, *Z. Kristallogr*. **1992**, *200*, 305–315.

[39] M. Weisser, S. Tragl, H.-J. Meyer, *Z. Kristallogr. NCS*, **2007**, *223*, 5–6.

[40] J. D. Tornero, J. Fayos, *Z. Kristallogr*. **1990**, *192*, 147–148.

[41] J. Beck, Ch. Kusterer, R.-D. Hoffmann, R. Pöttgen, *J. Solid State Chem.* **2006**, *179*, 2298–2309.

[42] J. A. M. van Liempt, Dissertation, Univ. Delft, Netherlands, **1931**.

[43] G. M. Sheldrick, *Acta Crystallogr. Sect. A.* **2008**, *64*, 112–122.

[44] V. Kolesnichenko, D. C. Swenson, L. Messerle, *Chem. Commun.* **1998**, 2137–2138.

[45] L. B. Anderson, F. A. Cotton, D. DeMarco, A. Fang, W. H. Ilsley, B. W. S. Kolthammer, R. A. Walton, *J. Am. Chem. Soc.* **1981**, *103*, 5078–5086.

[46] F. A. Cotton, D. DeMarco, B. W. S. Kolthammer, R. A. Walton, *Inorg. Chem.* **1981**, *20*, 3048–3051.

[47] M. K. Wilkinson, J. W. Cable, E. O. Wollan, W. C. Koehler, *Phys. Rev.* **1959**, *113*, 497–507.

[48] S. Hashimoto, K. Forster, S. C. Moss, *J. Appl. Crystallogr.* **1989**, *22*, 173-180.

[49] R. J. Birgeneau, W. B. Yelon, E. Cohen, J. Makovsky, *Phys. Rev. B*, **1972**, *5*, 2607–2615.

[50] C. Vetter, *J. Phys. Chem. Solids*, **1975**, *36*, 401–405.

[51] F. Menil, *J. Phys. Chem. Solids*, **1985**, *46*, 763–769.

[52] R. Poly, R. C. Torriba, *Inorg. Chim. Acta*, **1993**, *212*, 123–134.

[53] F. A. Cotton, K. R. Dunbar, C. T. Eagle, L. R. Falvello, A. C. Price, *Inorg. Chem.* **1989**, *28*, 1754–1757.

[54] R. Stranger, T. Lovell, J. E. McGrady, *Inorg. Chem.* **1999**, *38*, 5510-5518.

[55] S. Shaik, R. Hoffmann, C. R. Fisel, R. H. Summerville, *J. Am. Chem. Soc.* **1980**, *102*, 4555-4572.

[56] D. W. Brogden, Y. Turov, M. Nippe, G. Li Manni, E. A. Hillard, R. Clérac, L. Gagliardi, J. F. Berry, *Inorg. Chem.* **2014**, *53*, 4777-4790.

[57] J. E. McGrady, R. Stranger, T. Lovell, *Inorg. Chem.* **1998**, *37*, 3802-3808.

[58] G. Cavigliasso, C.-Y. Yu, R. Stranger, *Polyhedron*, **2007**, *26*, 2942-2948.

[59] G. M. Chiarelli, F. A. Cotton, C. A. Murillo, Q. Zhao, *Inorg. Chem.* **2014**, *53*, 2288-2295.

[60] J. A. M. Canich, F. A. Cotton, L. M. Daniels, D. B. Lewis, *Inorg. Chem.* **1987**, *26*, 4046-4050.

[61] E. F. Pettersen, T. D. Goddard, C. C. Huang, G. S. Couch, D. M. Greenblatt, E. C. Meng, T. E. Ferrin, *J Comput. Chem.* **2004**, *25*, 1605-1612.

[62] I. Mayer, *Chem. Phys. Lett.* **1983**, *97*, 270-274.

[63] A. E. Reed, R. B. Weinstock, F. Weinhold, *J. Chem. Phys.* **1985**, *83*, 735-746.

[64] A. Ferrari, A. Braibanti, G. Bigliardi, *Acta Crystallogr.* **1963**, *16*, 846–847.

[65] Y.-Q. Zheng, Y. Grin, K. Peters, H. G. von Schnering, *Z. Anorg. Allg. Chem.* **1998**, *624*, 959–964.

[66] W. Eichler, H. J. Seifert, *Z. Anorg. Allg. Chem.* **1977**, *431*, 123–133.

[67] A. Mos, M. Ströbele, H.-J. Meyer, *Z. Anorg. Allg. Chem.* **2015**, *641*, 2245–2249.

[68] C. Brink, N.F. Binnendijk, J. van de Linde, *Acta Crystallogr.* **1954**, *7*, 176–180; G. Meyer, *Z. Anorg. Allg. Chem.* **1984**, *515*, 127–132; S. Hull, P. Berastegui, *J. Solid State Chem.* **2004**, *177*, 3156–3173.

[69] S. Andersson, S. Jagner, *Acta Chem. Scand.* **1985**, *40A*, 177–181.

[70] Y. Xu, S. Carlson, K. Söderberg, R. Norrestam, *J. Solid State Chem.* **2000**, *153*, 212–217.

[71] R. Clay, J. Murray-Rust, P. Murray-Rust, *Acta Cryst.* **1975**, *B31*, 289–290.

[72] I. Díaz, V. Fernández, J. Luis Martínez, L. Beyer, A. Pilz, U. Müller, *Z. Naturforsch. B.* **1998**, *53*, 933–938.

[73] Y.-Q. Zheng, J. Nuss, H. G. von Schnering, *Z. Kristallogr. NCS*, **1998**, *213*, 680.

[74] H. Womelsdorf, H.-J. Meyer, *Angew. Chem.* **1994**, *106*, 2022–2023, *Int. Ed.* **1994**, *33*, 1943; H. Womelsdorf, H.-J. Meyer, *Z. Anorg. Allg. Chem.* **1996**, *622*, 2083–2088.

[75] M. Weisser, R. Burgert, H. Schnöckel, H.-J. Meyer, *Z. Anorg. Allg. Chem.* **2008**, *634*, 633–640.

[76] E. J. Welch, J. R. Long, *Angew. Chem. Int. Ed.* **2007**, *46*, 3494–3496.

[77] D. A. Evans, S. J. Miller, T. Lectka, P. von Matt, *J. Am. Chem. Soc.* **1999**, *121*, 7559-7573; S. E. Balaghi, E. Safaei, L. Chiang, E. W. Y. Wong, D. Savard, R. M. Clarke, T. Storr, *Dalton Trans.* **2013**, *42*, 6829–6839.

[78] R. D. Willett, K. Chang, *Inorg. Chim. Acta*, **1970**, *4*, 447–451.

[79] H. Jahn, E. Teller, *Proc. R. Soc. London, Ser. A*, **1937**, *161*, 220–235.

[80] M. A. Halcrow, *Chem. Soc. Rev.* **2013**, *42*, 1784–1795.

[81] S. Bieller, H.-W. Lerner, M. Bolte, *Acta Crystallogr. Sect. E*, **2005**, *61*, 928–929.

[82] M. Wei, R. D. Willett, K. W. Hipps, *Inorg. Chem.* **1996**, *35*, 5300–5303.

[83] D. N. Hay, D. C. Swenson, L. Messerle, *Inorg Chem*. **2002**, *41*, 4700-4707.